NACA

RESEARCH MEMORANDUM

SUMMARY AND ANALYSIS OF HORIZONTAL-TAIL CONTRIBUTION TO LONGITUDINAL STABILITY OF SWEPT-WING AIRPLANES AT LOW SPEEDS

By Robert H. Neely and Roland F. Griner

Langley Aeronautical Laboratory
Langley Field, Va.

NATIONAL ADVISORY COMMITTEE
FOR AERONAUTICS

WASHINGTON

August 23, 1955

CONTENTS

[redacted]

NATIONAL ADVISORY COMMITTEE FOR AERONAUTICS

RESEARCH MEMORANDUM

SUMMARY AND ANALYSIS OF HORIZONTAL-TAIL CONTRIBUTION TO LONGITUDINAL STABILITY OF SWEPT-WING AIRPLANES AT LOW SPEEDS

By Robert H. Neely and Roland F. Griner

SUMMARY

Available wind-tunnel data on the low-speed horizontal-tail contribution to the static longitudinal stability of high-speed airplane configurations incorporating unswept and sweptback wings are reviewed and analyzed. The characteristics of the flow behind wings and wing-body combinations are described and related to the downwash at specific tail locations for unseparated and separated flow conditions. The effects of variations of tail position, variations of wing plan form and airfoil section, trailing-edge flaps, stall-control devices, and ground interference on the air-flow characteristics and tail contribution are analyzed and demonstrated. The more favorable tail arrangements are emphasized and their application to specific configurations is illustrated. The analysis of the factors affecting the horizontal-tail contribution is, for the most part, descriptive; however, an attempt has been made to summarize certain data by empirical correlation or theoretical means in a form useful for design.

INTRODUCTION

The analysis of the downwash behind wings given in references 1 to 3 has provided a good basis from which the horizontal-tail contribution to the static longitudinal stability can be estimated for wing-body combinations having thick unswept wings of moderate to high aspect ratios. This analysis was concerned largely with the conditions of unseparated flow and little rolling-up of the trailing vortex sheet, which conditions are applicable to most of the useful flight range for the type of wings considered. The corresponding problem for current high-speed airplane configurations is considerably more complicated than the problem studied in references 1 to 3. The increased complexity of the wing-body-tail interference problem is due to (1) the presence of flow separation over

the wing for a considerable portion of the lift-coefficient range, which results from the use of sweep and airfoil sections having small nose radii, (2) the faster rolling-up of the vortex sheet resulting from the use of low-aspect-ratio wings (ref. 4), and (3) the greater importance of the fuselage because of its larger size. Early investigations of wing-tail interference for swept-wing configurations (refs. 5 and 6) showed that the tail had a powerful influence on the variation of stability through the lift-coefficient range and that this influence varied greatly with the vertical location of the tail. Numerous subsequent investigations have been conducted at both low and high speeds to study the wing-tail interference problem for various swept-wing configurations. In reference 7 a number of the important factors affecting the horizontal-tail contribution at low speeds were examined, and the problem of combining a tail with wing-fuselage combinations to provide good longitudinal stability characteristics was discussed.

The purpose of the present paper is to provide a more comprehensive review and analysis than was given in reference 7 of present knowledge concerning the low-speed horizontal-tail contribution for sweptback-wing airplanes. The characteristics of the flow behind sweptback wings and wing-body configurations are described and related to the downwash characteristics of specific tail locations for unstalled and stalled flow conditions. The effects of variations of tail position, variations of wing plan form and airfoil section, trailing-edge flaps, stall-control devices, and ground interference on the air-flow characteristics and tail contribution are analyzed and demonstrated. The more favorable tail arrangements are emphasized and their application to specific configurations are illustrated.

A brief analysis of the tail contribution to stability of thin unswept-wing configurations of small aspect ratio is included. Swept-forward or composite plan forms are not considered; however, data for such configurations are given in references 8 to 12. The analysis of the factors affecting the horizontal-tail characteristics is, to a large extent, descriptive. It was not possible to present quantitative design charts for estimating the tail contribution, but it was possible to correlate a number of significant parameters affecting the tail contribution and to suggest rough design procedures based on this empirical correlation. The experimental data on which the analysis in this paper is based were obtained mostly at Reynolds numbers greater than 4×10^6.

In addition to the analysis presented herein, an index to published data on the air-flow characteristics and stability contribution of the horizontal tail obtained from tests of models at Reynolds numbers greater than 4×10^6 has been prepared and is presented in tables I and II. For convenience, an index to figures is presented as table III.

SYMBOLS

C_L	lift coefficient
$C_{L_{max}}$	maximum lift coefficient
C_m	pitching-moment coefficient
c_l	section lift coefficient
ΔC_L	increment of wing lift coefficient due to deflecting trailing-edge flaps
L	lift
Γ	wing circulation
U	longitudinal velocity
q	free-stream dynamic pressure
R	Reynolds number based on mean aerodynamic chord of wing
M	Mach number
A	aspect ratio
b	span (wing span unless otherwise noted) measured perpendicular to plane of symmetry
c	local chord measured parallel to air stream
$\bar{c}$	mean chord measured parallel to air stream
c'	mean aerodynamic chord, $\frac{2}{S}\int_0^{b/2} c^2 dy$
d	maximum fuselage diameter
d_t	fuselage diameter at $c'/4$ of tail
h	horizontal-tail height normal to plane containing wing-root-chord line, positive when above plane through wing-root-chord line

[redacted]

l	horizontal-tail length parallel to wing-root-chord line measured from the airplane center of gravity to quarter-chord point of tail mean aerodynamic chord (center of gravity assumed at quarter-chord point of wing mean aerodynamic chord unless otherwise noted)
m	distance parallel to wing-root-chord line measured from three-quarter-chord point of wing mean aerodynamic chord to quarter-chord point of tail mean aerodynamic chord
S	area (wing area unless otherwise noted)
Λ	angle of sweepback (from quarter-chord line unless otherwise noted), deg
δ_f	deflection of trailing-edge flaps, deg
λ	taper ratio
i_w	angle of incidence of wing measured with respect to fuselage center line, positive when wing trailing edge is down, deg
i_t	angle of incidence of horizontal tail measured with respect to plane containing wing-root-chord line, positive when tail trailing edge is down, deg
x	longitudinal coordinate, positive rearward
y	spanwise coordinate
z	vertical coordinate, positive upward
x_0	longitudinal coordinate measured from $c'/4$
x_{TE}	longitudinal coordinate measured from wing trailing edge at a given spanwise station
z_{TE}	vertical coordinate measured from horizontal plane through wing trailing edge at a given spanwise station
v	downwash velocity at x,y
b'	vortex spacing
z'	vertical distance between tail and a line connecting vortex centers

[redacted]

w	wake-center location above extended wing-chord plane
α	angle of attack of wing-root-chord line with respect to horizontal plane, deg
α_1	wing angle of attack for increase in $d\epsilon_{max}/d\alpha$, deg
α_2	wing angle of attack for unstable C_m change of tail-off configuration, deg
ϵ	downwash angle, downflow positive, deg
$\epsilon_{\Lambda=0}$	downwash angle for wing having 0° sweepback of quarter-chord line, deg
ϵ_{max}	maximum downwash angle, deg
$\Delta\epsilon$	increment of downwash angle due to deflecting trailing-edge flaps, deg
ϵ_e	effective downwash angle, $\alpha + i_t - \alpha_t$, deg
ϵ_B	downwash due to body alone, deg
e_w	downwash induced by wing and image vortices, deg
σ	sidewash angle, deg
$\frac{q_t}{q}$	ratio of local dynamic pressure (at horizontal tail) to free-stream dynamic pressure

$$\eta\left(\frac{q_t}{q}\right)_e = -\frac{C_{m_{i_t}}}{C_{L_{\alpha_t}} V}$$

$C_{L_{\alpha_t}}$	lift-curve slope of isolated horizontal tail, $\frac{dC_L}{d\alpha_t}$, deg
C_{m_t}	pitching-moment coefficient contributed by horizontal tail

$C_{m_{i_t}}$ rate of change of pitching moment with horizontal-tail incidence, $\partial C_m / \partial i_t$

α_t angle of attack of horizontal-tail root chord, $C_{m_t} / C_{m_{i_t}}$, deg

V horizontal-tail-volume coefficient, $\frac{l}{c'} \frac{S_t}{S}$

τ tail stability parameter, $\frac{1}{VC_{L_{\alpha_t}}} \frac{\partial C_{m_t}}{\partial \alpha}$

Subscripts:

w wing

t horizontal tail

e effective

LE leading edge

TE trailing edge

max maximum

MODEL NOTATION AND TAIL PARAMETERS

Model Notation

For any given model, only the most pertinent details have been presented herein. For complete details refer to the original reference applicable to the given model.

A three-number notation is used to identify the plan-form characteristics of the wing where the notation gives, in order, the sweepback of the quarter-chord line, the aspect ratio, and the taper ratio. As an example, the model having the wing characteristics $\Lambda_{c/4} = 50.0^\circ$, $A = 2.88$, and $\lambda = 0.625$ is designated as a 50-2.9-.63 wing or 50-2.9-.63 wing-body combination.

The plan form of the horizontal tail is also designated by the three-number notation. Unless specifically noted as being a tail, the three-number notation on the figures refers to the wing.

[redacted]

The airfoil sections of a lifting surface having a round-nose leading edge are defined by the standard NACA airfoil designations. Airfoil sections having sharp leading edges are referred to as either circular-arc, wedge, or hexagonal airfoil sections. The designated airfoil sections refer to sections parallel to the free stream unless otherwise noted. For particular details of wings having twist and camber, reference to the original paper should be made.

The leading-edge devices (flap, slat, etc.) are referred to by spans in fractions of wing semispan and the deflection angles are omitted. The outboard end of the leading-edge device is located between 97 percent and 100 percent of the semispan.

The designated span of the trailing-edge flaps is the location of the outboard end of the flap. Most of the wing-body configurations with trailing-edge flaps have the flap inboard ends located at or close to the intersection of the wing trailing edge with the body. The wing configurations without bodies have the inboard end of the trailing-edge device located at the plane of symmetry.

Deflections of some of these devices are measured in a plane parallel to the air stream, whereas others are measured in a plane perpendicular to a constant percent-chord line on the swept wing panel. When such details are needed, reference to the original papers should be made.

It should be noted that the extended split flap is a split flap with the hinge located at the wing trailing edge.

Tail Air Flow and Stability Parameters

Effective values of downwash angle and dynamic pressure.- The effective downwash angle ϵ_e and the dynamic-pressure ratio are calculated from the experimental pitching-moment data. For configurations where only two horizontal-tail incidences and a tail-off configuration were investigated, the lift curve of the tail was assumed to be linear and the effective-flow parameters were calculated as follows:

$$\epsilon_e = \alpha + i_t - \alpha_t \tag{1}$$

where

$$\alpha_t = \frac{C_{m_t}}{C_{m_{i_t}}}$$

[redacted]

and

$$\eta\left(\frac{q_t}{q}\right)_e = \frac{C_{m_{i_t}}}{\left(C_{m_{i_t}}\right)_0} = -\frac{C_{m_{i_t}}}{C_{L_{\alpha_t}} V} \tag{2}$$

where

$$C_{m_{i_t}} = \frac{\partial C_m}{\partial i_t}$$

for a given configuration with or without flaps, and

$$\left(C_{m_{i_t}}\right)_0 = \frac{\partial C_m}{\partial i_t}$$

for the condition when the tail is located out of the wake and away from the wing-chord plane of the flap-off configuration at $\alpha = 0^\circ$.

When data with enough tail incidences were available, the value of ϵ_e was determined by equation (1) by using the condition that $\alpha_t = 0^\circ$ at the intersections of the tail-on and tail-off pitching-moment curves.

Tail stability parameter.- The combined effects of downwash angle and dynamic pressure on the stabilizing contribution of the horizontal tail is defined by the tail stability parameter τ (see ref. 13):

$$\tau = \frac{\partial C_{m_t}}{\partial \alpha} \frac{1}{C_{L_{\alpha_t}} \frac{S_t}{S} \frac{l}{c'}} \tag{3}$$

which, for a linear lift-curve slope, is

$$\tau = -\left[\eta\left(\frac{q_t}{q}\right)_e \left(1 - \frac{d\epsilon_e}{d\alpha}\right) + \alpha_t \frac{d\eta\left(\frac{q_t}{q}\right)_e}{d\alpha}\right] \tag{4}$$

A negative value of τ indicates that the tail is contributing stability. The values of τ presented were computed by equation (3) by assuming a linear tail lift-curve slope.

OUTLINE AND SCOPE OF ANALYSIS

The general objectives of the analysis contained in this report are to provide an understanding of the factors affecting the tail contribution to stability, to evaluate existing methods and provide new information for predicting the tail contribution, to demonstrate the effects of various configuration parameters on the tail contribution, and to indicate how the tail may be combined with wing-body combinations to provide desirable overall stability characteristics. These points are discussed under three subject headings which are the basic air-flow characteristics behind wings, the analysis of the stability contribution of specific horizontal tails, and the tail design providing desirable overall stability of the wing-body-tail configuration.

In order to provide a basis from which the analysis of the tail contribution can proceed, the air-flow characteristics behind wings and wing-body combinations are discussed in some detail. The vorticity distributions on the wing and in the wake are first described, and the effects of these distributions on the magnitude of the downwash angle and the position of the downwash field with respect to the wing, which are of prime importance in determining the tail contribution, are shown. The accuracy of certain idealized representations of the vortex system in depicting the flow field is determined by comparisons of calculated and experimental downwash angles. The flow behind both wings and wing-body combinations are reviewed and analyzed. The flows in the wake of wings are discussed as to whether the flow over the wing is unseparated or separated because of the large differences in the flow obtained for these two conditions. The flow characteristics for plain swept- and unswept-wing configurations are discussed at some length; in addition, the effects of various arrangements of stall-control devices and trailing-edge flaps on the flow are considered briefly.

The analysis of the longitudinal-stability contribution of the tail is begun with some general considerations of the lift produced by a tail surface when placed in a given flow field. Next, the fundamental aspects of tail location and geometry affecting the variation of the stability contribution with angle of attack are brought out by analyzing the non-uniform changes of downwash angle at the tail as it moves down with angle of attack through the flow field of sweptback-wing—body combinations. The points concerning the tail contribution which are emphasized are the direction of the changes of the tail contribution, the angles of attack where these changes occur, and the magnitude of the tail contribution, the primary emphasis being on the stalled-flow regime. Experimental data on the aerodynamic factors entering into the tail contribution at both low and high angles of attack are collected and correlated for a large number of plain-wing configurations. A procedure for estimating the tail contribution which is based, in part, on the experimental summaries is

outlined. The remainder of the analysis of the tail contribution is devoted to a demonstration of the quantitative effects of various configuration and test variables on the tail contribution of selected configurations. These effects are explained briefly in terms of the basic flow characteristics.

When the design of a horizontal tail to provide desirable overall configuration stability is considered, the general classes of tail-off pitching-moment curves and the differences in the required tail contribution are discussed by using the analysis of reference 7. The tail locations and volumes which tend to give desirable stability characteristics are then demonstrated for configurations with various types of tail-off pitching-moment curves.

AIR-FLOW CHARACTERISTICS

Plain-Wing Configurations Without Flow Separation

The downwash behind a wing depends on the magnitude and distribution of vorticity on the wing and in the trailing vortex sheet. The distribution of vorticity in the trailing vortex sheet changes with distance from the wing because of the rolling-up and distortion of the sheet. These changes in the configuration of the vortex sheet generally decrease the magnitude of the downwash over the tail region and cause the downwash variation in the vertical direction to become unsymmetrical about the vortex-sheet center line. As shown in reference 4, the same degree of rolling-up of the vortex sheet is defined by equal values of the parameter $\frac{x_{TE}}{b}\frac{C_L}{A}$ for wings with similar circulation distributions.

In the application of the Biot-Savart law to the calculation of the downwash behind wings (refs. 1, 2, 4, and 14 to 18), the vortex sheet is generally assumed to be flat with no rolling-up although the distortion is accounted for by displacing the sheet by a constant amount. Inasmuch as rolling-up may be of some consequence for the configurations under consideration, it is desirable to know how much rolling-up has occurred and its possible effect on the downwash calculation. For convenience in generalizing results on downwash and rolling-up of the trailing vortex sheet behind unstalled surfaces suitable for high-speed flight, wings are classified as wings having unswept trailing edges and nearly elliptical loadings (low aspect ratio) and those having sweptback trailing edges and loadings which are nearly uniform or reduced at the center of the wing.

Wings with unswept trailing edges and low aspect ratio.- For wings with unswept trailing edges and low aspect ratio, it is assumed that the load distribution does not depart very far from an elliptical load distribution. The shape of the vortex sheet as it moves downstream of the trailing edge is represented schematically in figure 1(a). The rolling-up phenomena have been discussed considerably by previous investigators (see, for example, ref. 4). In reference 4 approximate formulas for calculating the coordinates of the partially rolled-up vortex cores are suggested. These formulas are a modification of Kaden's results for the rolling-up of a vortex sheet of semi-infinite width. A few checks with experimental data indicate that the formulas of reference 4 predict the paths of the tip-vortex cores reasonably well for elliptical wings. Although these checks are not conclusive, the inward movement of the tip vortices, which is an indication of the degree of rolling-up of the trailing vortex sheet, is considered to be represented adequately by the results of reference 4 for wings with unswept trailing edges and nearly elliptical loadings.

For low lift coefficients the representation of the vortex system as a flat sheet without any rolling up is considered a good approximation for calculating downwash angles at usual tail locations. The excellent agreement between experimental and calculated downwash for several unstalled low-aspect-ratio sweptback wings from reference 18 is shown in figure 2. The downwash was calculated by distributing an elliptical spanwise loading at four chordwise stations. The distribution of load in a chordwise direction does not appear to have an important effect on downwash, however, except for positions near the wing. Falkner in reference 19 indicates that concentration of the load at the 0.25 chord line on a 60° delta wing will result in an underestimation of ϵ/C_L equal to 7 percent at 0.43c behind the trailing edge and 3 percent at 1.30c.

The limits of applicability of the concept of the nonrolled-up sheet for calculating the magnitude and position of the downwash behind unstalled wings are not well defined. Results of calculations given in reference 2 and of additional calculations based on the positions of the partially rolled-up vortex of reference 20 indicate that the influence of the distortion and rolling-up of the vortex sheet on the downwash angle near the plane of symmetry may be neglected for values of $\frac{x_{TE}}{b}\frac{C_L}{A} < 0.13$ for wings with approximately elliptical loadings. In these calculations the entire sheet was displaced downward an amount equal to the displacement at the plane of symmetry. If the value of $\frac{x_{TE}}{b}\frac{C_L}{A}$ of 0.13 is near the upper limit for neglecting the effects of distortion and rolling-up, then errors will arise in the practical range of lift coefficients when the flat-sheet representation with no rolling-up

is used for calculating the downwash. Separation may occur, however, before the limiting lift coefficient is reached, in which case the rolling-up phenomena and downwash characteristics are considerably changed as will be discussed later.

Sweptback wings with sweptback trailing edges.- For the sweptback wing with a sweptback trailing edge, the load distribution over the center part of the wing may be nearly uniform or, in most cases, shows a reduction in loading at the plane of symmetry. As a consequence the downwash decreases as the plane of symmetry is approached. This decreased downwash and the initial disposition of the vortex sheet gives rise to a trailing vortex sheet as illustrated in figure 1(b). The maximum displacement of the vortex sheet from the horizontal is obtained outboard of the plane of symmetry for locations near the wing but is obtained near the plane of symmetry far downstream of the wing (see ref. 21). Some insight into the rolling-up process may be gained by studying the lateral movement of the tip vortex. The tip-vortex positions behind three wings with sweptback trailing edges (refs. 22, 14, and 21) are presented in figure 3. The lateral movement of the tip vortices with increasing downstream distance is negligible, and the minimum vortex spacings measured are much greater than the spacings calculated for a fully rolled-up vortex sheet (approximately 0.85b/2). These results indicate that there is little rolling-up of the vortex sheet for the conditions in figure 3 which cover a range of $\frac{x_{TE}}{b}\frac{C_L}{A}$ likely to be of interest for the unseparated-flow case. It appears, then, that the assumption of a flat sheet with no rolling-up is justified for the calculation of downwash for a range of conditions at least as large as that for wings with unswept trailing edges and nearly elliptical loadings. The rolling-up process for the types of wings in figure 3 appears to be different than that for wings described in the previous section. This fact is shown by the smaller inward movement of the tip vortices of the present wings compared with the movement obtained on straight wings (fig. 3(a)) and the movement calculated by the method of reference 21 (which is essentially the method of ref. 4) (fig. 3(c)).

The downwash behind an unstalled 40-4.0-.63 wing as calculated in reference 14 is compared with experimental results in figure 4. The calculated values of downwash in the vortex sheet are low by about 20 percent at the plane of symmetry, but the discrepancy is less at positions away from the plane of symmetry and the vortex sheet. The downwash in the vortex sheet is very sensitive to the shape of the loading curve. Neglecting the effects of negative vorticity at the plane of symmetry which is indicated by the load distribution reduces the discrepancy between experimental and calculated downwash (see fig. 4(b)). Differences between experimental and calculated downwash similar to that just described have been observed for a 30-4.5-1.0 wing in reference 15 and a 45-3.5-.50 wing

(with nose flap deflected) in reference 23. In the latter reference experimental load distributions were used.

Because air in the boundary layer collects near the wing tips and because of the closer proximity of the outboard wing sections to the survey plane, the maximum loss of dynamic pressure in the wake is obtained behind the outboard sections. (See fig. 5.) In figure 5 and a number of subsequent figures the outline of the wing is projected in the stream direction onto the survey plane which is perpendicular to the main air stream. As shown in figure 5, the wake-center location can be predicted accurately by using the calculated downwash angles; however, an empirical relation for estimating the wake-center location which is accurate enough for most cases has been derived from available survey data. The relation for a spanwise station of approximately $0.25b/2$ is

$$\frac{d\frac{z_{TE}}{x_{TE}}}{d\alpha} = -\left(0.0175 - \frac{d\frac{w}{x_{TE}}}{d\alpha}\right) = \frac{-1.5}{\pi A}\frac{dC_L}{d\alpha} \qquad (5)$$

for wings with $\lambda = 0.4$ to 1.0 and $\Lambda = 30^\circ$ to 60°. For more highly tapered wings a value of 2.0 instead of 1.5 in equation (5) gives better results. Equation (5) applies best for tail lengths from $2l/b = 0.9$ to 1.5.

For a given angle of attack the downwash behind the inboard part of a wing decreases with increasing sweepback because of the accompanying decrease and outward shift of the lift. Because of the changes in downwash angle, the wake displacement relative to a horizontal line through the trailing edge also decreases with increasing sweepback. Some experimental data demonstrating this effect are shown in figure 6. In this figure the ordinate is the angle through which the wake is displaced from a horizontal line per unit change of wing angle of attack. The change in wake displacement is considerable for $\lambda = 1.0$, but it appears that the change decreases with a decrease in λ.

Wing-body combinations.- When a fuselage is added to a wing, the flow field behind the wing is altered because the circulation distribution over the wing is changed and an additional flow component is introduced because of the flow about the fuselage.

In order to demonstrate the phenomena involved in wing-body downwash, the components of the downwash angle of a combination consisting of a 50-2.9-.63 wing mounted on an infinite circular cylinder are shown in figure 7 for a vertical location of $z = 0$ and a longitudinal location of $x = \infty$. The total downwash is considered to be made up of the downwash due to the wing in the presence of the body, the downwash due to the isolated body, and the downwash due to mutual interference between

the flow fields of the wing and the body. In calculating the downwash the method used in reference 24 for representing the vortex system was followed. The vortex sheet was assumed to be flat and in line with the body. The downwash due to the wing was obtained by using the summation of the theoretical wing-alone loading and a body-induced loading calculated in reference 25 for a wing-body combination similar to the present one. This calculated loading is shown in figure 8. The downwash due to the isolated body was obtained from the increments of velocity resulting from the crossflow around an infinite circular cylinder at a velocity of $U\alpha$. The interference flow which represents the reduction of the body crossflow due to the wing downwash was obtained by determining the downwash induced by vortices which are situated within the fuselage boundary and are images of the vortices shed from the wing.

As shown in figure 7, the downwash due to the exposed wing vortices is approximately equal to the downwash of the wing alone for the example given, but this equality is not necessarily true. The interference downwash at the side of the body is given exactly by the product of the wing downwash and the nondimensional velocity increment due to the crossflow around the body $\left(\frac{d/2}{y}\right)^2$, and for stations away from the side of the body the downwash is given approximately by this product. The importance of small changes in wing loading close to the body on the flow is obvious and these changes are of greater importance than those for the wing alone. In the region close to the body, however, the greatest difficulty is encountered in predicting the body-induced loading (ref. 26). Calculations made for a plane at the top of the body show that the downwash is not very sensitive to the exact shape of the spanwise load distribution and that the predominant change between wing-alone and wing-body downwash is the large downwash angle above the body resulting from the tendency of the flow to follow the body.

Values of downwash calculated by the method described in the preceding paragraph are compared in figure 9 with the experimental values of downwash for a 50-2.9-.63 wing-body combination obtained from the original data of reference 27. A crude correction for the effect of afterbody contraction (fig. 8) on the flow field was made by displacing the flow field calculated for the combination with the infinite circular cylinder an amount equal to the displacement of the axial-flow streamlines about the body. The displacement of the axial-flow streamlines resulting from afterbody contraction is given approximately by the relation from reference 28:

$$y_2^2 - y_1^2 = \left(\frac{d_2}{2}\right)^2 - \left(\frac{d_1}{2}\right)^2 \qquad (6)$$

Although the downwash variation with spanwise distance are predicted qualitatively by the theory, the agreement between theoretical and experimental values of downwash is generally poor and is not so good as was obtained for the wing-alone configuration of figure 4. The calculated downwash is too low, particularly at spanwise stations near the body. Inaccuracies result when using the present method for calculating the downwash of wing-body combinations inasmuch as this method neglects the effects of the bound vortex and the movement between the vortex sheet and body and does not offer a rational solution for the flow near the end of the fuselage. Another source of error may be in the assumed span loading. Besides the factors relating to the method of calculation, there are other factors affecting the comparison in figure 9 which are related to the conditions of the experimental configurations. The value of the downwash gradient is changing rapidly in the region of the body center line so that the experimental accuracy is not so good as in other regions of the flow field. Viscous flow phenomena which are not considered in the calculation affect the flow field. Measurements reported in reference 29 indicate that the large upwash angles as obtained near infinite cylinders are not obtained in the regions of high rates of contraction of a finite-length body. The comparison shown in figure 9 is not considered conclusive in evaluating the method of calculation for bodies with nearly constant cross sections where the theory is most applicable. Experimental data for such configurations are needed. In addition, an evaluation of the effects of the bound vortex on downwash, possibly by the method suggested in reference 30, is desirable.

Plain-Wing Configurations With Flow Separation

The flow behind wings with separated flow differs significantly from the flow behind wings with unseparated flow. Although some characteristics of the flow are the same behind various stalled wings, differences in the flows do exist and are demonstrated by discussing the flow characteristics for several wings which differ considerably in plan form. In this discussion considerable emphasis is placed on the variation of the maximum downwash angle with angle of attack behind the inboard wing sections and the vertical position of the maximum downwash angle. These parameters are useful and convenient in describing the state of the flow and are of great importance in determining the downwash variation obtained at the tail.

Sweptback-wing configurations.- Wing flow characteristics for several stalled sweptback-wing configurations are indicated by span loading and tail-off pitching-moment curves in figure 10. The variations of the maximum downwash angle with angle of attack for a station within the span of a tail are also shown. The maximum downwash angle is used here as a convenient method of indicating changes in the flow field. Detailed flow

characteristics behind the wings are shown by vector plots and dynamic-pressure contours in figures 11 to 13. The variations of downwash with vertical distance from the wing trailing edge are given in figure 14.

As a result of the inward progression of separation which begins at the wing tips, the spanwise locations of the large changes in loading (fig. 10) and, consequently, the locations of the regions of large vorticity in the wake move inward with increasing angle of attack. In addition, the circulation about the wing increases with angle of attack at a greater rate after separation occurs, as indicated by the increased lift-curve slope of sections near the center of the wing in references 31 to 33 for low-aspect-ratio wings and in references 34 and 35 for high-aspect-ratio wings. Because of these two effects, the maximum downwash angle increases with angle of attack at a greater rate after separation occurs. The value of $d\epsilon_{max}/d\alpha$ does not increase significantly, however, until the regions of large vorticity have moved some distance inboard of the tips, as indicated by the load distribution in figure 10(a) and by the pitching-moment curves in figures 10(b) and 10(c).

The detailed flow characteristics behind a 60° delta (52.4-2.3-0) wing obtained from reference 36 are shown in figure 11. The flow behind other wings of the same plan form is described in references 37 and 38. A separation-vortex characteristic of sweptback wings with small nose radii forms along the leading edge and trails off the wing inboard of the wing tip. This vortex is identified by a region of large flow angles, rapid changes in flow angles, and reduced dynamic pressure. The vortex leaves the wing above the trailing edge and is inclined slightly downward with respect to a horizontal plane. With increasing angle of attack (see figs. 11(a) and 11(b)), the vortex moves inward and enlarges, and the center appears to move slightly upward relative to the wing trailing edge. Most of the vorticity shed from the wing appears to be concentrated in this separation vortex even during the early stages of development. Note data for $\alpha = 11.0°$ in figure 11(a) where a distinct viscous wake exists behind the inboard stations but no abrupt change in sidewash occurs while going through the wake. The span loading for this configuration (fig. 10(a)) also indicates that little vorticity would be shed behind the inboard sections. There is probably a small range of angle of attack where vorticity is contained in both the separation vortices and a continuous vortex sheet. This result was obtained for wings with nose radii larger than that of the present wing in reference 36. The positions of the separation vortices appear to be slightly outboard of the positions of a fully rolled-up pair of vortices as calculated from experimental load distributions of reference 32. The maximum downwash at a spanwise station of $0.27b/2$ is obtained along a line connecting the vortex centers as shown in figure 14(a).

The existence of regions of reduced dynamic pressure and the diffusion of these regions with increasing downstream distance (see figs. 11(b),

11(c), and 11(d)) indicate the existence of an inflow similar to that described in reference 2 for two-dimensional wakes. For the conditions in figure 11, however, the inflow phenomenon is essentially three dimensional. The distribution of downwash due to inflow in an xz plane passing through the region of low dynamic pressure will be similar to that obtained for two-dimensional wakes; moreover, a contribution to the downwash is obtained in xz planes outside the regions of low dynamic pressure because of the downwash components of the inflow. The contribution of the inflow to the downwash has not been evaluated; however, it can be said that its magnitude will diminish with increasing downstream distance.

By using the experimental load distribution of reference 32 the downwash behind the 60° delta (52.4-2.3-0) wing was calculated on the assumption that the vorticity was concentrated in a single swept horseshoe vortex. The calculated variations of ϵ_{max} with angle of attack and variations of downwash with vertical distance are compared with the experimental variations in figure 15. As shown in figure 15(a) the calculated values of ϵ_{max} and $d\epsilon_{max}/d\alpha$ at high angles of attack are lower than the experimental values. The agreement between experimental and calculated results is fairly good if the displacement of the experimental downwash curve as indicated by the extrapolated value of ϵ_{max} at $\alpha = 0$ is taken into account. The experimental and calculated variations of downwash with vertical distance differ by a constant amount at $2y/b = 0$ but by varying amounts at $2y/b = 0.3$ (see fig. 15(b)).

The vortex system behind the 45-3.5-.50 wing of figure 10(b) appears to be less concentrated than that for the 60° delta (52.4-2.3-0) wing just described even though the flows over the wings are basically similar. As shown in reference 23, the flow behind the 45-3.5-.50 wing appears as a vortex sheet in the early stages of separation but a large part of the vorticity is located within the outer one-third of the semispan. With increasing angle of attack, the vorticity becomes more concentrated. The flow angles at the higher angles of attack are more irregular than those obtained behind the 60° delta wing (compare figs. 11 and 12), and there are two distinct regions of low dynamic pressure behind the 45-3.5-.50 wing. For this wing a tip vortex and a separation vortex are both present. A plot of the integral of the circulation in the wake as a function of spanwise distance in figure 16 indicates that the tip vortex is relative weak. The calculated position of a completely rolled-up vortex is outboard of the position of the separation vortex as shown in figure 12. The flow behind the 45-3.5-.50 wing and the 50-2.9-.63 wing of reference 27 demonstrates very well the general effect of tip stalling on the position of the maximum downwash angle. As shown in figures 14(b) and 14(c), the position of the maximum downwash angle tends to move downward with angle of attack in accord with the wake-center movement until the wing stalls ($\alpha = 16.3°$ for the 50-2.9-.63 wing). As the wing stalls, the position of ϵ_{max} moves upward but this change occurs before $d\epsilon_{max}/d\alpha$

increases. The maximum downwash angle is generally obtained along a line connecting the separation-vortex centers at the higher angles of attack as in the case of the 60° delta wing.

Values of ϵ_{max} calculated for the 45-3.5-.50 wing by assuming a single swept horseshoe vortex whose strength and span were determined from the experimental span loading are considerably lower than the experimental values. Note that the calculated spans of the vortex were larger than the measured spans of the separation vortex in which most of the vorticity is concentrated. Downwash which was calculated in reference 23 by use of the vorticity distribution indicated by the experimental load distribution also indicates rather poor agreement with experimental results in regard to both ϵ_{max} (fig. 17) and the downwash angles outside the region of ϵ_{max}. For the type of flow observed on the 45-3.5-.50 wing, the disagreement between results of experiment and calculations based on the two extreme methods of vortex representation is not surprising.

For wings without the separation vortex on the surface, the change in load distribution due to tip stalling will still cause strong vortices behind the wing inboard of the tip as shown by data for a 45° delta wing in figure 8 of reference 39. These vortices appear to be less distinct and the flow is less steady than for a wing with separation vortices. The origin of these vortices appears to be above the trailing edge just as for the separation vortices.

The flow behind a sweptback-wing—body combination of high aspect ratio without the separation-vortex flow is illustrated in figure 13 for a condition of high angle of attack. These data were obtained from reference 40. A well-defined vortex sheet is indicated behind the inboard part of the wing even though the flow over the outboard part of the wing is separated as shown in figure 10(c). This result is in contrast to the results for the two wings discussed previously where vorticity behind the inboard wing sections was not discernible, and it is attributed to the large aspect ratio of the wing of figure 13. The position of ϵ_{max} as shown in figure 14(d) moves downward with angle of attack approximately in accordance with the wake movement even after the wing stalls; however, the position of ϵ_{max} moves only a small amount below the trailing edge.

The effects of a body on the flow behind a wing at high angles of attack are not well understood. Some of the effects for low angles of attack discussed previously would be expected to apply, at least qualitatively, to the high-angle-of-attack case. However, the displacement of the vortex sheet, or vortices, from the fuselage may be large and the effects of the body on the motion of the vortex system may be of importance. Viscous effects would also be expected to be more important at high angles of attack. No experimental studies have been made to determine

directly the effects of a body on the flow at low speeds, but results of tests at supersonic speeds reported in reference 24 of wings with separation vortices may be indicative of the body effects at low speeds. These results showed that the effect of the body on the motion of the wing vortices was dependent on body size and indicated the presence of two pairs of vortices originating near the nose and near the rear of the body. A simplified theoretical analysis of the effects of a body on the motions of wing vortices is presented in reference 41, and calculations of the downwash behind wing-body combinations at high angles of attack are presented in reference 42.

Unswept-wing configurations of low aspect ratio.- For unswept wings the initial stall may occur anywhere along the span, depending on the taper ratio. Consequently, the flow in the vicinity of the tail may vary considerably for wings of various taper ratios. For highly tapered wings, stalling will begin at the tip and the general flow phenomena would be similar to that described for sweptback wings. For wings with small taper, separation begins near the root and the flow would be expected to be much different from that behind sweptback wings. The general characteristics of the flow behind a wing of small taper will be described in this section.

The flow behind a 3.4-4.0-.63 wing is similar to that described in reference 2 for a stalled unswept wing. As demonstrated in figure 18, the predominant feature of the flow is a wide wake having considerable losses in dynamic pressure. The inflow into this wake determines to a great extent the vertical-downwash variation for positions close to the wing. The large reduction of the wake-induced downwash resulting from increased longitudinal distance as shown in figure 18 is in accord with the calculated trends of reference 3. The downwash at the center of the wake behind the wing-root section is lower than if the wing had not stalled. The maximum values of downwash shown in figure 19 for a station about 2 chord lengths behind the trailing edge show the same trend.

Body effects on the downwash are significant. The downwash above the body is increased considerably (see fig. 20), and the variation of maximum downwash with angle of attack is greater than for the wing alone as shown in figure 19. The angle of attack for increased values of $d\epsilon/d\alpha$ above the body appears to be associated with the onset of a deep boundary layer on the fuselage.

Sweptback-Wing Configurations With Stall Control

Stall-control devices have very little effect on the wing span loading due to changes in angle of attack before the wing stalls and, consequently, can be expected to have little effect on the variation of downwash with angle of attack in this range.

Stall-control devices can have a considerable effect on the span-load distribution when the wing is stalled but the effect on the wing loading and flow characteristics behind the wing will depend on the type and arrangement of the flow-control measure employed. There is very little information from which the influence of stall devices on the over-all flow characteristics behind a wing can be determined directly; therefore, the following discussion of the effects of various means of stall control on the flow characteristics is based to a large extent on the influence of stall-control devices on the separation and loading characteristics of the wing.

The effect of leading-edge flaps, or slats, on the stalling behavior and span loading of the wing depends primarily on the location of the inboard end of the device and on the wing plan form. For small to intermediate spans ($< 0.6b/2$), leading-edge flaps maintain the loading over the outer part of the wing and, for a given angle of attack, cause separation and the large dropoff of span loading to occur closer to the plane of symmetry than would occur for the plain wing. These results are illustrated in figure 21 for the 45-8.0-.45 wing of reference 43. The effects of leading-edge flaps on the flow characteristics behind a 45-5.1-.38 wing-body combination (ref. 44) are shown in figures 22 and 23. The region of high vorticity in the wake (for this wing, the separation vortices) are located farther inboard for the wing with leading-edge flaps than that for the plain wing because of the more inboard location of the large change in spanwise loading. Note the more inward location of the regions of large spanwise downwash gradients and low dynamic pressure in figure 22. In this figure it may also be seen that the increase in maximum downwash as the region of high vorticity is approached is much less with the leading-edge flap on the wing. The data of figure 23 show that the variation of maximum downwash with angle of attack behind the inboard survey station $0.16b/2$ is practically unaffected by leading-edge flaps, whereas ϵ_{max} is reduced at an earlier angle of attack behind the outboard station $0.32b/2$. The effects of leading-edge flaps on downwash diminish with increasing vertical distance from the point of maximum downwash. This result could have been anticipated because irregularities in span loading have a smaller effect on downwash as the distance from the position of maximum downwash is increased.

If the span of the flap or slat is long enough, the discontinuity at the end of the flap may cause the separation to spread mostly inboard. In this case the flow phenomena should be similar in many respects to those described in the previous section for an unswept wing having separated flow near the root. The flow angles would be smaller but the losses in dynamic pressure would be greater for the configuration with the stall-control device than for the plain sweptback-wing configuration. If full-span devices are employed, a delay in the changes in flow at the tail is experienced but the flow changes due to separation are basically similar to those for wings without flaps.

The description of the air flow over wings with partial-span leading-edge chord-extensions in reference 7 indicates that the loading over such configurations is similar to that for wings with leading-edge flaps, except that the loading over the outboard sections may not be maintained to as high an angle of attack. Therefore, the effects of chord-extensions on the flow at the tail are similar to those of leading-edge flaps.

Although the aerodynamic action of fences is somewhat different, effects on the load distribution are similar to those of leading-edge flaps in that fences delay the loss of lift outboard of the fence and cause earlier separation or loss of lift inboard of the fence (see ref. 43). All three of the stall-control devices discussed so far have much the same effect on the wing loading and, probably, on the flow behind the wing.

As shown in reference 35, combined camber and twist delayed appreciably the load changes on a 45-8.0-.45 wing but had no appreciable effect on the spanwise location of the initial separation. With regard to the flow at the tail, incorporation of camber and twist causes a delay in the flow changes and possibly a change in the severity of the flow changes.

Sweptback-Wing Configurations With Trailing-Edge Flaps

Flow behind wings and wing-body combinations with partial-span flaps at a low angle of attack.- The downwash and dynamic-pressure characteristics behind a 40-4.0-.63 wing (ref. 14) and wing-body combination (ref. 45) with partial-span split flaps, respectively, are presented in figures 24 and 25 for a low angle of attack. Since the angle of attack is small, the absolute values of downwash presented in figure 24 may be considered as closely representing the effect of deflecting the flaps. The maximum downwash behind the wing is obtained above the wake center line because of the wake-induced downwash (ref. 2) and the effects of the distortion of the vortex sheet. The influence of the body on the detailed air-flow characteristics is particularly significant near the wing-body juncture. The body reduces the downwash at spanwise stations near the wing-body juncture, increases the downwash at outboard stations, and displaces the wake near the body upward (fig. 24). These results may be explained by the presence of a strong vortex which originates near the wing-body juncture and has a direction of rotation opposite to that of the tip vortex. (See ref. 46.)

No attempt has been made to calculate the downwash due to deflecting flaps because of the large body effects present for the practical wing-body case. Calculations were made, however, to determine the dynamic pressure and wake dimensions behind the wing on the assumption of a two-dimensional wake as in reference 1 in order to demonstrate the three-dimensional character of the flow. As shown in figure 26, agreement

between dynamic-pressure characteristics determined from experiment and by calculation is poor. The wake intensity was lower and the width was much less at the inboard station than that calculated. The differences in the results are to some extent attributed to the rolling-up of the trailing vortex sheet but are primarily attributed to the outward flow in the wake which occurs on and near the wing because of the large spanwise pressure gradient behind the flap.

Surveys of the flow behind sweptback wings and wing-body combinations at various angles of attack with trailing-edge flaps are presented in references 13, 14, 23, 27, 36, 40, 44, 45, and 47.

Effect of angle of attack on flow behind wing-body combinations with trailing-edge flaps.- The changes in the detailed flow characteristics behind wing-body combinations with trailing-edge flaps as the angle of attack is increased through the stall are complex, and the changes are dependent to some extent on the trailing-edge flap and stall-control arrangement employed. For the present discussion, the flow behind wing-body combinations employing partial-span leading-edge and trailing-edge flaps will be described inasmuch as this combination is the most important case.

Flow separation and the loss in lift on various sections of a flapped wing occur at an earlier angle of attack than on an unflapped wing, and at some high angles of attack the loading on the two wing configurations is similar as shown in reference 43. The downwash of the flapped wing will then tend to approach that of the unflapped wing at a high angle of attack. The effects of trailing-edge flaps on downwash and wake characteristics below this angle of attack are illustrated in figure 27 for the 45-5.1-.38 wing-body combination of reference 44. The region of large downwash which is obtained behind the wing flaps at the lowest angle of attack in figure 27(a) is masked by flow changes due to separation as the angle of attack of the wing is increased, so that at $\alpha \approx 19^\circ$ the downwash distributions behind the flapped and unflapped wings are similar. The upward movement of the region of maximum downwash is, of course, much greater for the flapped wing than for the unflapped wing since the position of maximum downwash is lower with flaps on at low angles of attack but approaches the position for the unflapped wing at the higher angles of attack. It may be seen in figure 27(a) that the vertical downwash gradients are larger behind the configuration with trailing-edge flaps at the lower angles of attack. Although the variations of the maximum downwash with angle of attack for individual spanwise stations are irregular, the variations of maximum downwash obtained by spanwise integration across a typical tail span indicate an increase in the value of $d\epsilon_{max}/d\alpha$ when the wing stalls.

ANALYSIS OF STABILITY CONTRIBUTION OF HORIZONTAL TAIL

In this analysis of the stability contribution of the tail, certain aspects of the lift developed by a tail surface when placed in the flow field behind a wing-body combination will be discussed first. Next, the effective downwash obtained at the tail as it moves down with angle of attack through the downwash field will be analyzed in terms of the tail location relative to the chord plane and in terms of the tail geometry. Then, the effects of wing plan form, airfoil section, stall-control devices, trailing-edge flaps, proximity of ground, Reynolds number, and Mach number on the effective downwash characteristics and tail contribution τ are demonstrated. For the plain sweptback-wing configurations, a number of important factors affecting the tail contribution are correlated and consideration is given to methods for estimating the tail contribution.

Tail Lift Characteristics

The stability contribution of the horizontal tail is determined by the lift on the tail surface and the fuselage which results from placing the tail in the flow field of the wing-body combination. For tails mounted away from the fuselage, accurate values of the lift may be obtained by using average values of local tail angle of attack and dynamic pressure, which have been weighted according to the additional lift distribution of the tail. Satisfactory agreement with force-test results have been obtained in some cases by weighting according to the chord distribution (see regs. 13, 27, and 44). A proven method for calculating the lift of tail surfaces mounted on the body has not been developed. An approximate method for calculating the lift of a lifting surface and body combination has been suggested in reference 48. This method is extended to account for the main wing downwash inasmuch as it may prove useful in estimating the lift of a tail in the presence of a body and a wing and in developing more adequate estimation procedures. The lift of a surface and an infinite body at the same angle of attack α is given in reference 48 as

$$L = FL_{exp}\left(1 - \frac{d\bar{\epsilon}_B}{d\alpha}\right) \tag{7}$$

where

$$F = \frac{L_{surface} + L_{body}}{L_{surface}} = 1 + \frac{\int_{Surface} \left(-\frac{\epsilon_B}{\alpha}\right) c_l c \, dy}{\int_{Surface} c_l c \, dy}$$

where L_{exp} is the lift at an angle of attack α obtained by joining exposed wing panels, $L_{surface}$, the lift at an angle of attack α obtained on surface in presence of body, L_{body}, the lift at an angle of attack α obtained on body in presence of surface, and $\bar{\epsilon}_B$, the average body downwash across the exposed tail span. It may be noted that the parameter F is not sensitive to the shape of the load distribution and may be calculated by using any reasonable load distribution. According to reference 48, the ratio L/L_{exp} is relatively insensitive to the aspect ratio of the lifting surface. To the same degree of approximation, it would appear that equation (7) can be generalized to include the effect of the wing downwash as follows:

$$L = FL_{exp}\left(1 - \frac{d\bar{\epsilon}}{d\alpha}\right) = FL_{exp}\left(1 - \frac{d\bar{\epsilon}_B}{d\alpha} - \frac{d\bar{\epsilon}_w}{d\alpha}\right) \tag{8}$$

where $\bar{\epsilon}_w$ is the average downwash across exposed tail span due to wing and image vortices.

In the analysis of force-test data the isolated tail has been considered the basic lifting surface, and, for constant fuselage angle of attack, the ratio of the lift-curve slope of the tail and fuselage to that of the isolated tail is defined as η. In practice the isolation of the parameter η is uncertain so that it is best to use the parameter $\eta\left(\frac{q_t}{q}\right)_e$ as an indication of the lift characteristics of the tail. Experimental data on $\eta\left(\frac{q_t}{q}\right)_e$ are presented in figure 28 for tail surfaces mounted on the body. The isolated tail lift-curve slopes used in forming the ratios plotted in figure 28 were obtained by calculation in some cases and from experimental data in others. The available results indicate a fairly regular reduction of $\eta\left(\frac{q_t}{q}\right)_e$ with increase in body size. The variation is due mainly to the variation of η. Although $\eta\left(\frac{q_t}{q}\right)_e$ depends to some extent on the tail height and body shape, sufficient data are not available to ascertain the effects of these parameters. For tail surfaces mounted immediately adjacent to the body, values of $\eta\left(\frac{q_t}{q}\right)_e \approx 0.94$ have been measured in investigations reported in references 13, 27, and 49.

In the preceding discussions the lift curve of the tail was assumed to be linear; however, particular attention should be paid to nonlinearities

in the tail lift curve when using surfaces incorporating high sweep angles, low aspect ratios, and thin airfoils. Another factor of concern is the variation of the flow angle across the span of the tail as shown in figures 11 to 13 and 27(a). This variation may be sufficient to alter the stalling characteristics of the tail so that average values of tail angle of attack may not be indicative of the lift produced by the tail.

Basic Results for Sweptback-Wing Configurations

The horizontal-tail contribution to stability is not constant over the angle-of-attack range principally because the downwash angle at the tail varies nonuniformly with angle of attack. The latter result is due to the relative movement between the tail and the position of maximum downwash and to a nonuniform change in the general level of downwash with angle of attack.

A demonstration of how these factors affect the downwash variations at the tail is presented in figure 29 for a condition where the movement of the tail relative to the position of maximum downwash is large. The curves were calculated for a wing-tail system where the vortex system was represented by a pair of infinite vortices whose spacing and position relative to the tail were approximated from the results of reference 36. Calculations were made for the case where the vortex spacing was constant (fig. 29(a)) and for the case where the vortices moved inward with increasing angle of attack (fig. 29(b)). It can be seen that the movement of the tail through the downwash field introduces significant nonlinearities in the variation of the downwash at the tail even though the maximum downwash varies linearly with angle of attack. The inward movement of the vortices with increasing angle of attack accentuates the nonlinearities in downwash obtained at the tail but does not alter the trends shown for a constant vortex spacing. The downwash velocity for a constant value of x and y is

$$v = f(\Gamma, b', z') \tag{9}$$

where b' is the vortex spacing and z' is the vertical distance between the tail and a line connecting the vortex centers. Then,

$$\frac{dv}{d\alpha} = \frac{\partial f}{\partial \Gamma}\frac{d\Gamma}{d\alpha} + \frac{\partial f}{\partial b'}\frac{db'}{d\alpha} + \frac{\partial f}{\partial z'}\frac{dz'}{d\alpha} \tag{10}$$

The first two terms on the right-hand side are positive and increase in magnitude as z' approaches zero. The third term reaches a maximum positive value when the tail is above the line connecting the vortex centers (position of maximum downwash). This means that, as the tail moves downward with angle of attack, $d\epsilon/d\alpha$ increases with angle of

attack until the tail reaches a finite position above the point of maximum downwash ($z' = 0$) and that $d\epsilon/d\alpha$ decreases with angle of attack when the tail is below this position.

Examples of effective downwash variations obtained behind real wing-body combinations reported in references 27, 40, and 50 are presented in figure 30. Corresponding data on $d\epsilon_e/d\alpha$ and $\eta\left(\frac{q_t}{q}\right)_e$ are presented in figure 31. The basic flow characteristics for configurations similar to these have been described previously. The data in figures 30 and 31 show that the downwash does not vary continuously in a nonlinear manner from an angle of attack of 0° as for the configuration in figure 29 but rather, it varies linearly for part of the angle-of-attack range and then varies nonlinearly in a manner similar to that of the configuration in figure 29. For the configurations in figure 30 and for most other configurations discussed in this report, any nonlinear effects on downwash due to the movement of the tail with respect to the vortex sheet or due to the rolling up of the vortex sheet before separation occurs are small so that the value of $d\epsilon_e/d\alpha$ obtained at $\alpha = 0^\circ$ is essentially unchanged until separation occurs. The nonlinear variations of downwash at the tail with angle of attack shown in figure 30 are obtained because, after separation occurs, the maximum value of downwash increases at a substantially greater rate as shown in figure 10 and the relative movement between the tail and the point of maximum downwash is large as indicated by the movement of the wing chord line in figure 14. The relative importance of these factors in contributing to the nonlinear downwash variations may change, however, for different configurations. The dynamic pressure at the tail for the configurations of figure 31 does not vary significantly with angle of attack except at high angles of attack, so that $\frac{d\frac{q_t}{q}}{d\alpha}$ will not have any appreciable effect on the tail contribution as expressed by τ in equation (4) over most of the angle-of-attack range.

In the following discussion which deals with experimental results on tail location and tail geometry, the primary emphasis will be on the downwash in the range of lift coefficients where the flow over the wing is separated. The points concerning the downwash variations which are discussed are the direction of the changes of $d\epsilon_e/d\alpha$, the angles of attack where these changes occur, and the magnitude of $d\epsilon_e/d\alpha$.

Tail location.- As can be readily seen in figures 29 to 31, the downwash variations for angles of attack beyond the linear part of the downwash curves are affected considerably by the vertical location of the tail. The initial changes in the downwash variations are destabilizing for the high tail positions and stabilizing for the low tail

positions. As shown in figure 31, the initial changes in $d\epsilon_e/d\alpha$ tend to occur for the various tail positions at about the same angle of attack. This angle of attack corresponds closely to the initial wing stall angle which, for the low-aspect-ratio wings, is the angle of attack where the position of maximum downwash begins to move away from the wake center line but is lower than the angle of attack where $d\epsilon_{e_{max}}/d\alpha$ begins to increase. For all tail positions the magnitude of $d\epsilon_e/d\alpha$ decreases at some angle of attack. The angle of attack for decreasing $d\epsilon_e/d\alpha$ increases with increasing tail height h. Factors contributing to the decrease in $d\epsilon_e/d\alpha$ other than the movement of the tail through the downwash field as described for the simple vortex system in figure 29 are a decrease in $d\Gamma/d\alpha$ and a decrease of the average downwash over the tail span when the vortex cores or wakes encompass the tail.

From the data in figures 30 and 31 it may be inferred that there is a tail position near the chord plane which defines a boundary below which there are no destabilizing changes of $d\epsilon_e/d\alpha$. Data on six configurations which relate this boundary to the wake location are given in table IV. These data show that the maximum tail height for which there are no significant destabilizing changes in $d\epsilon/d\alpha$ is defined very well by the distance of the wake center from the wing chord plane at the angle of attack α_1 where $d\epsilon_{max}/d\alpha$ increases. This angle of attack is somewhat greater than the initial stalling angle of the wing. In terms of a significant wing characteristic, the maximum tail height for no destabilizing change in $d\epsilon_e/d\alpha$ is defined approximately by the wake-center location at the angle of attack α_2 where unstable changes in the tail-off pitching-moment curve are obtained. It should be noted that the aforementioned results were obtained for configurations where the movement between the tail and the wake center had no significant effect on $d\epsilon_e/d\alpha$ until stalling on the wing had occurred. The maximum tail heights for no destabilizing change of $d\epsilon/d\alpha$ are plotted against the distance from the trailing edge in figure 32 and compared with a mean boundary proposed in reference 51. Because of the nearly linear relation between the wake displacement and longitudinal distance from the trailing edge, straight lines that are drawn through the origin and any individual point will define a boundary applicable to a range of tail lengths.

The maximum value of $d\epsilon_e/d\alpha$ at the tail is important inasmuch as it is indicative of the least contribution to stability that the tail will provide. An illustration of the effect of tail height on the maximum value of $d\epsilon_e/d\alpha$ is shown in figure 33. The low angle-of-attack values of $d\epsilon_e/d\alpha$ are also shown. Above the boundary for no destabilizing change in $d\epsilon_e/d\alpha$ the maximum value of $d\epsilon_e/d\alpha$ increases with increasing tail

height to a peak value and then decreases. As shown in figures 29 to 31 maximum values of $d\epsilon_e/d\alpha$ are obtained at progressively higher angles of attack with increasing tail height and that the angle-of-attack range where $d\epsilon_e/d\alpha$ is larger than the low angle-of-attack value of $d\epsilon_e/d\alpha$ is greater as the tail height is increased. The decrease in maximum $d\epsilon_e/d\alpha$ noted in figure 33 may be explained as follows. In the discussion of the downwash results for a simple vortex system it was shown that the maximum value of $d\epsilon/d\alpha$ for the middle point on the tail is obtained when the tail is passing through a point located somewhat above the region of maximum downwash. Now, if the tail is above this point until $d\epsilon_{max}/d\alpha$ decreases, the resulting value of $d\epsilon/d\alpha$ at the tail would be lower than that obtained with the tail at a lower position. For complete tails located behind actual wings, the effective value of $d\epsilon_{max}/d\alpha$ is decreased at a high angle of attack by a reduction in $d\Gamma/d\alpha$ and a decrease of the average downwash over the tail span when the tail is immersed in the vortex cores or wake. Inasmuch as these factors are influenced by the inward progression of separation on the wing, the tail height at which the peak value of $d\epsilon_e/d\alpha$ is obtained appears to be related in some way to the angle of attack for $C_{L_{max}}$.

The effects of changes in tail length on the downwash characteristics behind a 52.4-2.3-0 wing-body combination reported in reference 50 are shown in figure 34. The magnitudes and variations of downwash are not affected much by change in tail length for $2h/b = 0.29$, 0.58, and 0.87 up to about $\alpha = 15^\circ$, but appreciable changes are obtained at higher angles of attack. The maximum value of $d\epsilon_e/d\alpha$ and the ensuing decrease in $d\epsilon_e/d\alpha$ are reached at a lower angle of attack as tail length is increased. This result can be visualized from a consideration of the movement of the tails through the downwash field behind the wing. The values of maximum $d\epsilon_e/d\alpha$ decrease with increase in tail length for a given tail height as shown in figure 35(a). For $2h/b = -0.07$, the variations of downwash (fig. 34) are similar although it may be seen that the downwash variation is more stabilizing for the most rearward tail position. For tail positions close to the boundary previously discussed, the type of downwash variation would be changed by a change in tail length.

It has been observed that the maximum values of $d\epsilon_e/d\alpha$ for the 52.4-2.3-0 wing-body combination may be correlated approximately if the tail location is given in terms of a tangent of an angle. The results of this correlation (where the angle is measured from the chord plane with the 3/4c' point as the origin) are shown in figure 35(b). The correlation obtained on the basis of equal tail-location angles has some theoretical justification. Results of calculations of $d\epsilon/d\alpha$ where the flow

was represented by a horseshoe vortex show the same trend as in figure 35(b) when the tail length was measured from the origin of the trailing vortices. The generality of the observed result is not known, but the degree of correlation obtained would depend on the choice of the origin. For the configuration in figure 35 satisfactory correlation is not obtained for tail lengths less than $1.44b/2$. The maximum values of $d\epsilon_e/d\alpha$ are obtained in the same angle-of-attack range for equal tail-location angles.

Tail-surface geometry.- When the possible effects of the span and plan form of the tail on $d\epsilon_e/d\alpha$ are considered, the spanwise variations of $d\epsilon/d\alpha$ must be studied. In general, the downwash in the region of the tail tip changes more over the angle-of-attack range than does the flow at the root. Within the α range where the wing flow is unseparated, an exception to this result occurs in that relatively large values of $d\epsilon/d\alpha$ are obtained in regions immediately above and below the fuselage as shown in figure 9. The detailed flow characteristics at various tail positions for separated flow on the wing are illustrated in figure 36 by contours of $d\epsilon/d\alpha$. The values of $d\epsilon/d\alpha$ tend to increase with increases in spanwise distance for high tail positions until the region of vorticity is reached; then the $d\epsilon/d\alpha$ value will decrease. As the angle of attack is increased from a low value, the flow at the tip of the tail is affected first, and for the higher tail positions $d\epsilon/d\alpha$ decreases first at the tip sections.

Tail plan forms can be altered to make important changes in the effective angle of attack of the tail in the direction indicated above; however, the magnitude of the possible changes has not been determined directly by experiment. Survey data of references 13, 27, 37, 40, and 44 may be used to obtain an estimate of this effect for wing-body combinations.

As suggested in reference 45, negative dihedral of the tail can be employed to move the tip away from the region of high $d\epsilon/d\alpha$ into region of low $d\epsilon/d\alpha$ and thus obtain some increase in the tail contribution. The change due to dihedral will obviously depend on the position of the tail relative to the downwash field. An example of the advantage of incorporating negative dihedral is shown in figure 37 for a 40-3.5-.58 wing-body combination with the root of the tail located at $2h/b = 0.28$.

Basic Results for Unswept-Wing Configurations

The variations of ϵ_e, $\eta\left(\frac{q_t}{q}\right)_e$, and τ with angle of attack for several unswept-wing—body combinations where separation begins near the root are shown in figure 38. The occurrence of nonlinearities in the downwash curves of figure 38(a) for a 5.3-2.5-.63 wing-body combination (ref. 49) appears to be associated primarily with flow separation on the wing as indicated by the fact that preventing separation by the use of

nose flaps results in approximately linear curves to nearly $C_{L_{max}}$ (see ref. 52). The downwash curves for the 5.3-2.5-.63 combination in figure 38 indicate an initial destabilizing trend for the two higher tail positions and a stabilizing trend for the low tail position. The factors contributing to the nonlinearities in the downwash curves are:

(1) Movement of tail through the wake. This effect may be stabilizing or destabilizing depending on the location of the tail relative to the wake center line. (See figs. 18 and 20.)

(2) Reduction in downwash behind the wing when the wing stalls (fig. 19).

(3) A large nonlinear increase in $d\epsilon/d\alpha$ above the fuselage resulting from the addition of the fuselage.

The increased values of $d\epsilon/d\alpha$ at the tail which result from the addition of a body are shown in figure 39 for a 3.4-4.0-.63 wing-body combination. The reduction in the destabilizing influence of the body with increasing spanwise distance emphasizes the importance of tail span in determining the tail contribution. This result was demonstrated in reference 53 for a model which had been shown in reference 54 to have large increases in $d\epsilon/d\alpha$ due to the body.

The magnitude of the loss of dynamic pressure at the tail and the variation of dynamic pressure with angle of attack shown in figure 38(b) are sufficiently large to be important in affecting the tail contribution τ.

The effect of increasing tail length on the downwash (fig. 38(a)) behind a 5.3-2.5-.63 wing-body combination appears to be moderate. Increasing the aspect ratio of the wing from 2.5 to 4.0 reduces downwash significantly. Part of this effect may be due to the increased ratio of tail span to body diameter b_t/d.

Additional data for unswept-wing—body combinations without flaps are presented in reference 55 and for configurations with the leading-edge and trailing-edge flaps in references 49 and 52.

Effect of Configuration and Test Variables on Tail Contribution

Wing plan form and airfoil section.- In order to demonstrate the effects of plan form changes on the downwash behind wings at low angles of attack, calculated values of the mean downwash over the tail span from

reference 56 are presented in figure 40. The effects of plan-form variables on the downwash for a given wing lift coefficient are shown in figure 40(a) in terms of the parameter $\frac{\pi A}{57.3}\frac{d\epsilon}{dC_L}$. The effects of sweepback on the downwash for a given angle of attack are shown in figure 40(b) in terms of the parameter $\frac{\epsilon}{\epsilon_{\Lambda=0}}$. For wings of moderate to high aspect ratio at a given lift coefficient (fig. 40), increasing the sweepback decreases the downwash as a result of the outward shift of load. This effect becomes smaller as the tail is moved away from the vortex sheet (increasing h). At a given angle of attack (fig. 40(b)), increasing the sweepback causes a greater reduction of downwash because of the accompanying decrease in C_L. The influence of sweepback on the average downwash varies with tail span because of the fact that the spanwise downwash gradient near the plane of symmetry (fig. 4(a)) increases with sweepback. Because of this result, trends shown by the downwash at the plane of symmetry should not be assumed to be indicative of the trends of the mean downwash. Results of calculations presented in figure 40(a) to determine effects of other wing-plan-form variables indicate that increasing the aspect ratio from 4 to 6 reduces the downwash parameter $\frac{\pi A}{57.3}\frac{d\epsilon}{dC_L}$ slightly, whereas reducing the taper ratio λ increases the value of $\frac{\pi A}{57.3}\frac{d\epsilon}{dC_L}$ considerably. The trends shown by the calculated data are verified by experimental data on a systematic series of wings in reference 57. Although data are not presented herein for wings of small aspect ratio with unswept trailing edges, sweepback should have a smaller effect on $d\epsilon/dC_L$ than shown in figure 40 because of the similarity of loadings on these wings. Changes in the wing plan form of wing-body combinations should have effects on the downwash at low angles of attack which are qualitatively similar to those obtained for wings alone. Systematic data showing such effects, however, are not available.

In order to demonstrate the effects of wing-plan-form variables on the downwash characteristics and tail contribution of wing-body combinations at both low and high angles of attack, data are presented in figures 41 to 44 for selected configurations which have geometric characteristics similar to each other except for the plan-form variable in question. A comparison of the tail characteristics of swept- and unswept-wing—body combinations from references 13 and 52 are presented in figure 41. Despite the dissimilarity in the stalling behavior and air-flow characteristics for the two configurations, the tail stability parameter τ (fig. 41(b)) of the swept- and unswept-wing—body combinations displays similar variations with angle of attack in that the stability parameter for the high and intermediate tails decreases initially and the stability parameter for the low tail increases initially with increase in the angle

of attack. These changes in the tail contribution, however, occur at a higher angle of attack and the degree of the unstable change of the high-tail stability contribution is greater for the sweptback wing. The latter result is due to the greater downwash of the sweptback wing which reaches higher lift coefficients than the unswept wing. Although data are not available to demonstrate conclusively the effect of wing sweep on the downwash for plan forms where tip stalling is present in all cases, a comparison of data for two configurations of aspect ratio 2 from references 58 and 59 in figure 42 indicates that increasing the sweepback angle from 37° to 56° had little effect on the downwash characteristics up to the maximum angle of attack tested.

The observed effects of aspect ratio (refs. 60 and 61) and taper ratio (refs. 62 and 63) on $d\epsilon_e/d\alpha$ in the stalled range as shown in figures 43 and 44 follow the trends obtained at low angles of attack.

The main effect of wing airfoil section on the tail contribution arises from a change in the angle of attack of flow separation and the attendant changes in the flow field. The characteristics of two 50° sweptback-wing configurations differing in nose radii (refs. 27 and 13) are compared in figure 45. The downwash changes at the tail were delayed until higher angles of attack were reached by increasing the nose radii but the maximum values of $d\epsilon_e/d\alpha$ for intermediate and high tail positions were increased. The reason for the latter effect is obvious since the total lift and, probably, distributions of lift at $\alpha = 28°$ are the same. As may be seen in table IV and figure 32, the delay in the angle of attack of stall by increasing the airfoil nose radius increases the maximum tail height for no destabilizing change of $d\epsilon_e/d\alpha$. Airfoil-section effects similar to those noted for the 50° swept wings have been obtained on 40° swept wings (refs. 60 and 63) where one of the wings did not exhibit separation vortices. The question of whether the type of flow separation on the wing will affect the tail contribution is difficult to answer because the change in separation angle of attack will be large enough to mask such effects.

Although few results are available at present, the effects on downwash of plan-form and airfoil-section modifications produced by leading-edge air inlets are of considerable interest. Tests of a 40-3.5-.58 wing-body combination indicated that large leading-edge air inlets located at the wing root reduced the value of $d\epsilon_e/d\alpha$ throughout the angle-of-attack range when the tail was located at $2h/b = 0.28$. Inlets of the type approaching a flush inlet gave results about the same as those of the basic wing. These results should not be generalized inasmuch as there is a possibility that some air inlets may produce a destabilizing downwash change.

The measured downwash characteristics for a large number of sweptback-wing—body combinations of various plan forms have been summarized in figures 46 and 47. The effective downwash characteristics at low angles of attack of 20 wing-body combinations are plotted as a function of the tail height $2h/b$ in figure 46 in four groups according to various combinations of the taper ratio, aspect ratio, and sweep angle. It has been determined that the magnitude of $d\epsilon_e/d\alpha$ in the stalled range of angles of attack may be correlated, in a rough sense, by relating this value of $d\epsilon_e/d\alpha$ to the low angle-of-attack value of $d\epsilon_e/d\alpha$ measured in the chord plane. The ratios of these two values of $d\epsilon_e/d\alpha$ are plotted against the tail-location parameter h/m in figure 47 for 18 sweptback-wing configurations. It should be noted that for any particular configuration the $d\epsilon_e/d\alpha$ ratios plotted in figure 47 were measured at different angles of attack for different tail heights. The value of $d\epsilon_e/d\alpha$ in the stalled range is about three or four times the low angle-of-attack value for the high tail positions and about 0.50 this value for the low tail positions. The $d\epsilon_e/d\alpha$ ratio appears to be dependent on the aspect ratio which may be a result of a difference in stalling behavior of the wing or the inexactness of tail-location parameter h/m in defining the maximum values of $d\epsilon_e/d\alpha$ for the smaller tail lengths.

Stall-control devices.- In the discussion on the basic air-flow characteristics behind sweptback wings with stall-control devices, the downwash before separation had occurred on the wing was shown to be unaffected by stall-control devices. Furthermore, it was indicated that, in general, some changes in the flow pattern in the region of maximum downwash angle are caused by the stall-control devices but the change decreases as the distance from the position of maximum downwash angle increases. The effects of various methods of stall control on the downwash and tail stability parameters are demonstrated in figures 48 to 51. In general, these results are consistent with the observations of the flow and show that the various means which have been used to improve the stability of the basic wing increase the tail contribution when the wing is stalled for tails located in a relatively high position. Only small effects are obtained when the tail is mounted in a low position.

The effects of $0.475b/2$ leading-edge flaps on the stability contribution of a tail mounted on the 45-5.1-.38 wing-body combination of reference 44 are shown in figure 48. For the high tail there is some reduction in the instability contributed by the tail at the higher angles of attack when the flaps are added. This change is caused by the change of flow near the tip of the tail. (See discussion of figure 23.) For the low tail no significant difference is noted. Data for 45-8.0-.45 and 50-2.9-.63 wing-body combinations in references 61 and 13 indicate some slight improvement due to partial-span leading-edge flaps for moderate to high tail locations.

Incorporation of long-span (0.725b/2) leading-edge flaps on a 40-4.0-.63 wing-body combination caused separation to occur first near the wing root. The change in location of separation from the midspan location obtained with shorter span flaps caused a reduction in the destabilizing change in the downwash variation with angle of attack for moderate to high tail positions. (Compare figures 7(i), 7(l), and 7(m) with figures 7(d), 7(g), and 7(h), respectively, of reference 60.)

The improvement due to leading-edge chord-extensions on the tail contribution of a 40-3.5-.50 wing-body combination is demonstrated in figure 49. Data on chord-extensions of 40-4.0-.50 and 35-3.6-.57 wing-body combinations with relatively high tails may be found in references 64 and 65.

The effect of wing fences on the tail contribution of a 40-3.5-.50 wing-body combination is smaller than the effect of chord-extension as shown by comparison of figures 49 and 50. Fences were shown to have a negligible effect on the tail contribution of a 45-8.0-.45 wing-body combination in references 61 and 66.

Combined twist and camber were highly beneficial to the tail contribution of a high-aspect-ratio wing configuration (see fig. 51). Camber and twist delayed and reduced the unstable changes in $d\epsilon/d\alpha$ for the high tail. Some benefit was gained for the intermediate tail but the benefit for the low tail was small. The methods of stall control used on a 45-8.0-.45 wing-body combination in order of increasing beneficial effects on the tail contribution were fences, leading-edge flaps, and combined camber and twist. Camber and twist had no beneficial effects on the downwash of a variable-sweep configuration ($\Lambda = 20^\circ$ to 60°) in reference 67, but this may be due to the fact that the tail was mounted in a relatively low position (average $h = 0.10b/2$).

Trailing-edge flaps.- The increments of downwash due to deflecting trailing-edge flaps on wing-body combinations are summarized in figure 52 in the form of a ratio of the measured effective downwash increment to the factor $\frac{\Delta C_L}{A\frac{b_f}{b}}$. This factor was found to give satisfactory correlation of the flap span effect for the calculated downwash angles of wings in reference 1 when the vertical location of the tail was measured from the vortex sheet. The degree of correlation indicated in figure 52 is satisfactory inasmuch as the maximum value of $\frac{\Delta\epsilon_e}{\Delta C_L \Big/ A\frac{b_f}{b}}$ corresponds to a value of $\Delta\epsilon_e$ not greater than 10°. The larger increments of downwash and the

values of $\frac{\Delta\epsilon}{\Delta C_L / A\frac{b_f}{b}}$ which do not correlate so well are obtained for low tail positions close to the wake. Some differences exist between the downwash factors for split flaps and for higher lift flaps which extend the wing chord.

The effects of trailing-edge flaps on the tail stability parameter and the downwash at the tail of several representative configurations having wings of 45° sweepback are shown in figures 53 and 54 for tails mounted in a high position and a low position, respectively. At low angles of attack where the downwash curves are linear and the tail contribution is constant, trailing-edge flaps have only minor effects on $d\epsilon_e/d\alpha$ (or τ) for tail positions above the wing chord plane. For tails below the wing chord plane, the flaps in some cases tend to increase the downwash parameter $d\epsilon_e/d\alpha$ at low angles of attack; however, no generally consistent behavior is evident from the available data. If the tail is located in the flap wake (see fig. 27(b)), some loss in the tail contribution would be obtained.

The initial nonlinearities in the downwash curves like those shown in figures 53 and 54 for flaps-deflected configurations are governed by the movement of the tail through the downwash field of the unstalled wing in addition to the changes in the downwash field arising from flow separation on the wing. The former effect which was generally unimportant for unstalled plain wings may be strong for tails passing through the region of large vertical downwash gradients obtained when trailing-edge flaps are deflected (fig. 27(a)); however, the effects of flow separation are the larger.

The magnitude of the stability contribution for tails located in low positions is increased (more negative τ or reduced $d\epsilon_e/d\alpha$) for moderate to high angles of attack by deflecting trailing-edge flaps (see fig. 54). For tails located in high positions such as in figure 53, the significant effect of trailing-edge flaps on the tail contribution at moderate to high angles of attack is that the maximum unstable value of τ is reduced. Although no data are presented for configurations having the tail mounted in an intermediate position, the downwash changes (reduced $d\epsilon_e/d\alpha$) due to flaps for such configurations are generally large after the tail passes through the region of maximum downwash (fig. 27(a)). The increased tail contribution due to flaps obtained after separation occurs is explained partly by the fact that the value of downwash of flapped configurations tends to approach the value for plain-wing configurations at a high angle of attack. (The angle of attack where this result occurs is approximately the angle where $\Delta C_L = 0$.) For low and intermediate tail heights, part of the increased tail contribution due to flaps results from the increased

tail movement relative to the position of maximum downwash and from the larger vertical downwash gradients below the region of maximum downwash (fig. 27(a)).

The maximum tail height for no destabilizing change in $d\epsilon_e/d\alpha$ which was discussed previously for plain wing configurations (fig. 32) is lowered by deflecting the trailing-edge flaps. The amount that this boundary is lowered is probably influenced by the type of flap. Some values of the maximum tail height for no destabilizing change in $d\epsilon/d\alpha$ which were determined from the survey data of references 44 and 27 are as follows:

Wing	Without flaps	With flaps
45-5.1-.38	2h/b = 0.13	2h/b = 0.05 (double slotted)
50-2.9-.63	2h/b = 0.15	2h/b = 0.10 (split)

The changes due to flaps shown in this table are to be expected since the region of maximum downwash is lowered. The magnitude of the change is influenced, however, by the flow behind the inboard end of the flap. This result may be shown by using the $d\epsilon/d\alpha$ contours of figure 55 for the 45-5.1-.38 wing-body combination with double-slotted flaps. In figure 55(a) for the boundary tail position $h = 0.05b/2$, the destabilizing effect of the outboard part of the assumed $0.37b/2$ tail is compensated for by a stabilizing effect of the inboard part of the assumed tail. The large changes of the local values of $d\epsilon/d\alpha$ with vertical and lateral position make it impossible to define the boundary tail height as simply as was done for cases without flaps.

Generalizations concerning the influence of tail span and taper ratio for low tails are difficult to make because of the large variations of ϵ and $d\epsilon/d\alpha$ in the spanwise direction and the large effect of angle of attack on these parameters. Force tests seem to be required to give reliable indications. The large changes of $d\epsilon/d\alpha$ for small changes of vertical distance shown in figure 55 indicate the use of dihedral in the tail will have a large effect on the tail contribution. For some tail heights it is probable that this effect will be larger for the case where flaps are deflected than for the case where flaps are neutral.

Proximity of ground.- Few data or analyses are available on ground effects on the flow at the tail of swept-wing airplanes. Flow measurements behind an unstalled 40-4.0-.63 wing in the presence of a ground board (ref. 14) indicate the same general effects of the ground as discussed in reference 3. These effects which are most pronounced at the center of the wing are a reduced downwash angle, a reduced wake displacement, and an unsymmetrical downwash profile with the maximum downwash generally occurring above the vortex sheet.

The influence of the ground on the downwash at the tail of a 40,4.0-.63 wing-body combination is shown in figure 56. These data taken from reference 60 show the reduced $d\epsilon_e/d\alpha$ associated with proximity of the ground. In addition, these data indicate that for the low tail positions large nonlinearities in the downwash curves occur before the angle of attack of flow separation, which is approximately 15° for the wing without flaps and 13° for the wing with flaps. The latter result is due to the large vertical downwash gradients below the wake center line and to the relatively large movement of the tail with respect to the wake center line.

It should be noted that for some airplane configurations the jet will be deflected by the ground. This flow change will affect the trim characteristics and possibly the stability of airplanes when the jet exhausts ahead of the tail and when the tail is located in the proximity of the jet.

Reynolds number and Mach number.- The effects of Reynolds number and Mach number (within the subsonic range) on the tail contribution of swept-wing configurations appear to be primarily dependent on the effects of these test variables on the total lift and load distribution on the wing. The tail contribution near an angle of attack of 0° will be very little affected by variation in Reynolds number except insofar as it may be affected by a change in the boundary-layer flow over the fuselage. This effect is of most concern for contracting bodies. The main effect of Reynolds number on the tail contribution is felt in its effect on the separation characteristics of the wing and the resulting flow changes at the tail. For wings with airfoil sections of small leading-edge radii, negligible Reynolds number effects are to be expected for Reynolds numbers from about 1×10^6 to 12×10^6 because of the small observed changes in the wing characteristics. Beyond this range the effects are unknown because of lack of comparable data on the wing characteristics. For wings with sections of moderate to large nose radii, increasing the Reynolds number delays the appearance of nonlinearities in the downwash curves (see refs. 68 and 69) and tends to alter the magnitude of $d\epsilon_e/d\alpha$ in a direction that the increasing nose radius has in figure 47.

Results of low-speed tests ($M < 0.25$) are applicable in a qualitative sense over a wide range of subsonic Mach number, but the extent to which the quantitative results are applicable is dependent on the wing section and plan form. As a consequence of the small change in the span-loading shape with Mach number, the low-speed values of $d\epsilon_e/dC_L$ for unstalled sweptback wings and wing-body combinations of references 56, 68, and 70 were not greatly changed up to a Mach number of at least 0.9 for most cases. Values of $d\epsilon_e/d\alpha$ generally increase with Mach number in the subcritical range because of the increase in the wing lift-curve slope.

Data for the stalled case indicate that Mach number changes the magnitude of $d\epsilon_e/d\alpha$, as in the unstalled case, and may change the angle of attack for nonlinear downwash variations. Some representative data showing the effects of Mach number on downwash behind stalled wings are presented in references 71 to 73. In general, reducing the wing thickness and increasing the wing slenderness (low aspect ratio and high sweep) reduce the effects of Mach number at both low and high angles of attack.

Estimation of Tail Contribution to Stability

The estimation of the horizontal-tail contribution to stability for wing-body combinations purely by theoretical means is limited in scope and of uncertain accuracy. The most reliable estimate of the tail contribution is one obtained from experimental data for a similar configuration. There are, however, certain general results and summaries obtained in the present study which are useful in the design of a horizontal tail. These results are reviewed in the following paragraphs from the viewpoint of estimating the contribution to stability of a horizontal tail on a sweptback-wing—body combination.

Low angles of attack.- For low angles of attack, a reasonable estimate of the downwash may be obtained from the experimental data summarized in figure 46. For tail heights greater than about two-thirds the body diameter away from the body center line, the calculated wing downwash should also be sufficiently accurate inasmuch as the body-interference effects are fairly small and the distance from the vortex sheet is large enough to avoid the difficulties encountered near the vortex sheet.

Estimation of the value of the parameter $\eta\left(\frac{q_t}{q}\right)_e$ appears to be more uncertain than that for downwash because of the small amount of data available. For tail surfaces mounted on the fuselage the value of $\eta\left(\frac{q_t}{q}\right)_e$ may be estimated from figure 28. For tails mounted immediately adjacent to the fuselage a value of $\eta\left(\frac{q_t}{q}\right)_e$ of 0.90 to 0.95 is recommended.

High angles of attack.- At high angles of attack the estimation of the tail contribution is less definite than at low angles of attack, but enough data are available to predict the direction of the initial change in the tail contribution with angle of attack, the angle of attack where this changes occurs, and the magnitude of $d\epsilon_e/d\alpha$ when the wing stalls.

The direction of the change in the stability contribution with angle of attack is given by the relation of the tail to the wake center line

at the angle of attack when the destabilizing change in the wing pitching moment or the decrease in lift-curve slope for the wing occurs. If the tail is above the wake at this angle of attack, the change in the tail contribution is destabilizing. The wake-center location may be determined from the theoretical downwash or from the simple approximate formula (eq. (5)) presented before. The maximum tail height for no destabilizing change in $d\epsilon/d\alpha$ is given in figure 32 for a number of configurations. It may be assumed that the initial significant departure of the tail contribution from that obtained at low angles of attack will occur when separation first appears on the wing. The magnitude of $d\epsilon_e/d\alpha$ for angles of attack where the flow over the wing is separated may be approximated from the experimental data of figure 47 for sweptback-wing—body combinations without flaps.

DESIGN CONSIDERATIONS OF A TAIL TO PROVIDE STATIC STABILITY

Tail Requirements

For the purpose of the present discussion the assumption is made that it is desirable to avoid unstable changes in $dC_m/d\alpha$ and to have a linear variation of pitching-moment coefficient with angle of attack if possible. The requirements of the horizontal tail to provide these characteristics are inherently dependent on the pitching-moment characteristics of the wing-body combination without the horizontal tail. The general classes of tail-off C_m curves encountered and the differences in the required tail characteristics have been discussed in reference 7. Quoting from reference 7 ". . . for a wing-fuselage combination exhibiting neutral stability throughout the lift range, a tail located in a field of constant $d\epsilon/d\alpha$ can provide an adequate and constant static margin. [See case I, fig. 57 of present paper.] For a wing-fuselage combination exhibiting an abrupt decrease in stability through some part of the lift range, it would be advantageous to have the tail so located that $d\epsilon/d\alpha$ decreased abruptly at the same lift coefficient at which the decrease in stability occurred for the wing-fuselage combination. [See case II, fig. 57 of present paper.] The linearity in the stability characteristics of the complete configuration would, of course, be dependent on the degree of instability compensated for by the decrease in $d\epsilon/d\alpha$. A third condition can be considered in which the wing-fuselage combination exhibits an abrupt increase in the stability through the lift range of such a magnitude as to be undesirable. A tail located so as to experience an abrupt increase in $d\epsilon/d\alpha$ at the corresponding lift coefficient could conceivably provide linear stability characteristics for the complete configuration. [See case III, fig. 57 of present paper.] Although the.

term 'abrupt' has been used in these illustrations, any gradual change in the stability characteristics of the wing-fuselage combination would necessitate gradual changes in $d\epsilon/d\alpha$ at the tail. Further, the absolute values of dynamic-pressure ratios occurring in the wake have been ignored in the preceding discussion inasmuch as they only affect the effectiveness of the tail and are, therefore, only of secondary importance with respect to $d\epsilon/d\alpha$. Also ignored is the term $\alpha_t \frac{\partial\left(\frac{q_t}{q}\right)}{\partial\alpha}$ which under certain conditions can have a measurable effect on the tail contribution to the overall stability." The above discussion emphasizes the importance of the angle of attack where the tail contribution changes, but it must be borne in mind that the ability to obtain the desired result depends on the tail volume.

Tail Locations and Tail Volumes to Obtain Desirable Stability

Unswept wings.- For configurations with thin unswept wings, the tail-off pitching-moment curve exhibits a large stabilizing change as in case III of figure 57 which may be followed by a destabilizing change. The principal problem for this case is to avoid locating the tail where it would be ineffective during the destabilizing part of the tail-off curve without providing excessive stability at lower angles of attack. It appears that so far as the downwash variations are concerned the tail should be moving out of the wake at angles of attack where the tail-off C_m curve is destabilizing. It is difficult to generalize about desirable tail locations, however, because of the significant contribution of $\left(\frac{q_t}{q}\right)_e$ and possibly $\frac{d\left(\frac{q_t}{q}\right)_e}{d\alpha}$ to the value of τ (see eq. 4).

Unstable sweptback wings.- For sweptback-wing—body combinations which exhibit destabilizing pitching-moment changes (case II, fig. 57), the most desirable tail location from low-speed considerations is a low location for which the tail contribution increases with increasing angle of attack. The increase in the tail stability parameter τ for the low tail positions is equal to about 50 percent of the low angle-of-attack value of $d\epsilon_e/d\alpha$ inasmuch as the change in $d\epsilon_e/d\alpha$ in going from low angles of attack into the stalled range is also about 50 percent of the low angle-of-attack value. The change in the tail contribution is, then,

$$\Delta\left(\frac{\partial C_{m_t}}{\partial \alpha}\right) \approx -0.5\left(\frac{d\epsilon_e}{d\alpha}\right)_{\alpha=0} C_{L_{\alpha_t}} V \eta\left(\frac{q_t}{q}\right) \qquad (11)$$

It should be noted that for increasing wing aspect ratio the unstable change in the pitching-moment curve becomes greater, but the possible increase in tail contribution to counteract this unstable change becomes smaller because of the aspect-ratio effect on $d\epsilon_e/d\alpha$. As a result, a relatively large value of the tail volume is needed to minimize the unstable changes in the moment curves of wings which are only slightly on the unstable side of the stability boundary of reference 5. Some experimental results that demonstrate this fact are presented in figure 58.

A disadvantage of the low tail as compared with a high tail is the greater increase in the tail contribution at low lift coefficients obtained when going from subsonic to supersonic speeds. The change in the tail contribution is in the same direction as the change of stability of the wing-body combination.

Stable sweptback wings.- Wing-body combinations which do not have any destabilizing changes in pitching-moment characteristics through the lift range will come under cases I or III (fig. 57). Considerably more freedom in selection of tail locations is available for these configurations than for configurations with unstable wings. For case I the tail could be located at positions up to the boundary tail position shown in figure 32 without any destabilizing changes in stability, and for case III the tail could be located at higher positions. Results are shown in figure 59 for two similar configurations where the tail is located so that the downwash variations are destabilizing. Figure 59(b) shows that the tail volume should not be large if stability is to be obtained. Locating the tail in a very high position where the values of $d\epsilon_e/d\alpha$ may not be excessive and the angles of attack for maximum $d\epsilon_e/d\alpha$ are high appears to offer attractive solutions for obtaining stability for certain airplane configurations.

Sweptback wings with stall-control devices.- Incorporation of stall-control devices will usually ease the requirements of the horizontal tail because of the improved stability of the wing. As a result of this and the improved downwash characteristics behind the wing, the range of useful tail locations is greater or the possibility of attaining the desired stability characteristics is increased when stall-control devices are used.

The considerations discussed for stable plain wings apply to the case where stall-control devices provide stable pitching-moment variations. Investigations show that configurations incorporating wings of 35° to 40° sweepback and aspect ratios from 3.5 to 4.0 can be made stable readily

by using stall-control devices. For these cases stable pitching-moment variations may be obtained for tail heights of the order of 0.4b/2. (See refs. 60, 63, and 65.)

Although a completely linear pitching-moment curve was not obtained, the addition of stall-control devices to a twisted and cambered wing of high aspect ratio produced stable moment characteristics for the airplane configuration when the horizontal tail was mounted in a low position (refs. 40 and 66). For the configuration without stall-control devices, no tail position was found that would provide stable moment characteristics.

CONCLUSIONS

Available wind-tunnel data on the low-speed horizontal-tail contribution to the static longitudinal stability of high-speed airplane configurations incorporating unswept and sweptback wings are reviewed and analyzed. From these data, the following conclusions were drawn:

1. For the purpose of generalizing results on downwash and rolling-up of the trailing vortex sheet behind unstalled surfaces suitable for high-speed flight, wings are classified according to the sweep of the trailing edge and the shape of the span-loading curve.

(a) For unswept or sweptback wings having unswept trailing edges and nearly elliptical loadings, the shape and the motion of the trailing vortex sheet is considered to be satisfactorily determined by previous theoretical analyses of the development of the trailing vortex system. Limits of the applicability of the displaced-flat-sheet representation of the vortex system for calculating downwash are discussed. Agreement between experimental and calculated downwash for some low-aspect-ratio sweptback wings is good at low angles of attack when this representation is used.

(b) For sweptback wings having sweptback trailing edges and loadings which are uniform or reduced near the plane of symmetry, the shape of the vortex sheet at normal tail locations is characterized by a smaller vertical displacement at the wing center than that for stations farther outboard. This result is attributed to the smaller downwash near the center and the difference in vertical position of the trailing edge at various spanwise stations. The rate of rolling-in of the tip vortices for these wings is small compared with that for wings with unswept trailing edges. Fair agreement between experimental and calculated downwash was obtained for sweptback wings with sweptback trailing edges. Sweepback causes a considerable reduction in the downwash at a given lift coefficient or angle of attack for unstalled wings of moderate aspect ratio and taper. There is a corresponding increase of the movement between the wake and tail with increasing sweepback angle.

2. The effects of a fuselage on the downwash at low angles of attack have been analyzed by using a simplified theoretical model. A comparison of theoretical and limited experimental downwash results on wing-body combinations is considered inconclusive. For the comparison made the experimental flow near the body was more uniform than theory indicated. Additional studies of the flow behind wing-body configurations are needed.

3. The maximum value of downwash in regions occupied by a tail increases with angle of attack at a greater rate when a sweptback wing stalls. During stalling the downwash profile becomes unsymmetrical about the wake center line, and at high angles of attack the maximum downwash is obtained along the horizontal line connecting the regions of high vorticity which are shed at the edge of the unseparated-flow region. A comparison between the downwash obtained from experiment and from calculations based on the experimental load distribution indicates that the flow field behind a stalled 60° delta wing is reasonably approximated by a single swept horseshoe vortex. For stalled wings of lower sweepback and higher aspect ratio, neither the single horseshoe vortex nor multiple vortices distributed according to the span loading are a satisfactory approximation of the actual flow.

4. The trend of the nonlinear variations of downwash with angle of attack obtained with the tail at various heights is defined by the relative movement between the tail and the point of maximum downwash in the flow field. The change in the magnitude of downwash behind a sweptback wing because of wing stall increases the nonlinearities in the downwash curves. The initial changes in the slope of the downwash curves which occur in most cases when separation first appears on the wing are destabilizing for high tail positions and stabilizing for low tail positions. The maximum tail height in the vicinity of the wing-chord plane below which there is no destabilizing change in the downwash curve is defined by the distance of the wake center line from the wing-chord plane at the angle of attack where the variation of maximum downwash angle with angle of attack $d\epsilon_{max}/d\alpha$ increases or where the tail-off pitching-moment curve indicates a destabilizing change. The maximum value of the variation of the effective downwash angle with angle of attack $d\epsilon_e/d\alpha$ at the tail generally increases with increase of tail height and reaches a maximum at a tail height which appears to be related to the angle of attack for maximum lift coefficient $C_{L_{max}}$. The maximum values of $d\epsilon_e/d\alpha$ for tails located at various longitudinal distances behind a 60° delta wing configuration could be correlated when the tail location was given in terms of an angle formed by the wing-chord line and a line drawn from the point of the wing three-quarter mean aerodynamic chord to the tail. As a result of the large variation of $d\epsilon/d\alpha$ in the spanwise direction, changes in tail surface geometry offer a means of making important changes in horizontal-tail contribution when the wing is stalled.

[redacted]

5. Lack of systematic data prevents an accurate evaluation of the effect of sweep on the tail contribution for stalled configurations. However, the variations of the tail contribution with angle of attack for thin low-aspect-ratio wings of 0° and 50° sweepback are demonstrated to be qualitatively similar despite the differences in wing-stalling and air-flow characteristics behind the wing. The tail contribution for the sweptback wing was lower than that for the unswept wing for high tail positions.

6. The various stall-control devices which have been used to improve the stability of the basic wing at high angles of attack increase the tail contribution at these angles of attack when the tail is located in a relatively high position but these devices have no significant effect when the tail is located in a low position.

7. Deflecting trailing-edge flaps generally has little effect on the tail contribution at low angles of attack except for tail positions below the wing-chord plane where the tail contribution was reduced in some cases. For the stalled-wing condition, flaps increase the tail contribution for low tails and decrease the maximum unstable tail contribution for high tails. The maximum tail height for no destabilizing change in $d\epsilon/d\alpha$ was lowered by deflecting flaps, and the amount that it was lowered was influenced to a large extent by favorable downwash variations near the inboard end of the flap.

8. Quantitative rules for predicting the tail contribution were not obtained; however, it has been possible to summarize some quantitative data which are useful in estimating the tail contribution. The data are:

(a) The effective downwash characteristics of 19 wing-body combinations for unseparated and separated flow conditions. (For the latter case a reasonable correlation was obtained by assuming that $d\epsilon_e/d\alpha$ during stalling for any tail position was proportional to the low angle-of-attack value of $d\epsilon_e/d\alpha$ measured in the wing-chord plane.)

(b) Values of the tail lift parameter $\eta\left(\frac{q_t}{q}\right)_e$ for tail surfaces mounted on and detached from bodies.

(c) Tail-height boundaries for six wing-body combinations below which there are no significant destabilizing changes of $d\epsilon/d\alpha$ with angle of attack.

(d) Wake displacements.

(e) The increment of downwash due to deflecting trailing-edge flaps.

Langley Aeronautical Laboratory,
National Advisory Committee for Aeronautics,
Langley Field, Va., May 11, 1955.

REFERENCES

1. Silverstein, Abe, and Katzoff, S.: Design Charts for Predicting Downwash Angles and Wake Characteristics Behind Plain and Flapped Wings. NACA Rep. 648, 1939.

2. Silverstein, Abe, Katzoff, S., and Bullivant, W. Kenneth: Downwash and Wake Behind Plain and Flapped Airfoils. NACA Rep. 651, 1939.

3. Katzoff, S., and Sweberg, Harold H.: Ground Effect on Downwash Angles and Wake Location. NACA Rep. 738, 1943.

4. Spreiter, John R., and Sacks, Alvin H.: The Rolling Up of the Trailing Vortex Sheet and Its Effect on the Downwash Behind Wings. Jour. Aero. Sci., vol. 18, no. 1, Jan. 1951, pp. 21-32, 72.

5. Shortal, Joseph A., and Maggin, Bernard: Effect of Sweepback and Aspect Ratio on Longitudinal Stability Characteristics of Wings at Low Speeds. NACA TN 1093, 1946.

6. Purser, Paul E., Spearman, M. Leroy, and Bates, William R.: Preliminary Investigation at Low Speed of Downwash Characteristics of Small-Scale Sweptback Wings. NACA TN 1378, 1947.

7. Furlong, G. Chester, and McHugh, James G.: A Summary and Analysis of the Low-Speed Longitudinal Characteristics of Swept Wings at High Reynolds Number. NACA RM L52D16, 1952.

8. Tolhurst, William H., Jr.: An Investigation of the Downwash and Wake Behind Large-Scale Swept and Unswept Wings. NACA RM A7L05, 1948.

9. Hoggard, H. Page, Jr., and Hagerman, John R.: Downwash and Wake Behind Untapered Wings of Various Aspect Ratios and Angles of Sweep. NACA TN 1703, 1948.

10. Martina, Albert P., and Deters, Owen J.: Maximum Lift and Longitudinal Stability Characteristics at Reynolds Numbers Up to 7.8×10^6 of a 35° Sweptforward Wing Equipped With High-Lift and Stall-Control Devices, Fuselage, and Horizontal Tail. NACA RM L9H18a, 1950.

11. Polhamus, Edward C., and Becht, Robert E.: Low-Speed Stability Characteristics of a Complete Model With a Wing of W Plan Form. NACA RM L52A25, 1952.

12. Goodson, Kenneth W., and Becht, Robert E.: Wind-Tunnel Investigation at High Subsonic Speeds of the Stability Characteristics of a Complete Model Having Sweptback-, M-, W-, and Cranked-Wing Plan Forms and Several Horizontal-Tail Locations. NACA RM L54C29, 1954.

13. Foster, Gerald V., and Griner, Roland F.: Low-Speed Longitudinal and Wake Air-Flow Characteristics at a Reynolds Number of 5.5×10^6 of a Circular-Arc 52° Sweptback Wing With a Fuselage and a Horizontal Tail at Various Vertical Positions. NACA RM L51C30, 1951.

14. Furlong, G. Chester, and Bollech, Thomas V.: Downwash, Sidewash, and Wake Surveys Behind a 42° Sweptback Wing at a Reynolds Number of 6.8×10^6 With and Without a Simulated Ground. NACA RM L8G22, 1948.

15. Diederich, Franklin W.: Charts and Tables for Use in Calculations of Downwash of Wings of Arbitrary Plan Form. NACA TN 2353, 1951.

16. Schlichting, H.: Calculation of the Downwash Behind Sweptback Wings. Part I. Sweptback Wings of Large Aspect Ratio. Tech. Note No. Aero 1890, British R.A.E., May 1947.

17. Schlichting, H.: Calculation of the Downwash Behind Sweptback Wings. Part II: Wings of Small Aspect Ratio With Zero Sweep. Rep. No. Aero.2228, British R.A.E., Oct. 1947.

18. Ross, J. G., Hills, R., Lock, R. C., and Meiklem, P.: Wind Tunnel Tests on a 90° Apex Delta Wing of Variable Aspect Ratio (Sweepback 36.8°). Pt. I. General Stability, by Ross, Hills, and Lock. Pt. II. Measurements of Downwash and Effect of High Lift Devices, by Lock, Ross, and Meiklem. C.P. No. 83, British A.R.C., 1952.

19. Falkner, V. M.: The Calculation by Lifting Plane Theory of the Downwash Behind a Wing. Rep. No. 11,778, British A.R.C., Sept. 17, 1948.

20. Westwater, F. L.: The Rolling Up of the Surface of Discontinuity Behind an Aerofoil of Finite Span. R. & M. 1692, British A.R.C., 1935.

21. Tolhurst, William H., Jr.: Downwash Characteristics and Vortex-Sheet Shape Behind a 63° Swept-Back Wing-Fuselage Combination at a Reynolds Number of 6.1×10^6. NACA TN 3175, 1954. (Supersedes NACA RM A52J08.)

22. Luetgebrune: Wake and Drag Tests on Swept and Straight Wings. Rep. No. CGD-106, Ryan Aero. Co. Translation, Dec. 6, 1945. (FB Nr. 1672, Deutsche Luftfahrtforschung.)

23. Lange, Roy H., and Fink, Marvin P.: Studies of the Flow Field Behind a Large Scale 47.5° Sweptback Wing Having Circular-Arc Airfoil Sections and Equipped With Drooped-Nose and Plain Flaps. NACA RM L51L12, 1952.

24. Spahr, J. Richard, and Dickey, Robert R.: Wind-Tunnel Investigation of the Vortex Wake and Downwash Field Behind Triangular Wings and Wing-Body Combinations at Supersonic Speeds. NACA RM A53D10, 1953.

25. Weber, J., Kirby, D. A., and Kettle, D. J.: An Extension of Multhopp's Method of Calculating the Spanwise Loading of Wing-Fuselage Combinations. Rep. No. Aero. 2446, British R.A.E., Nov. 1951.

26. Martina, Albert P.: The Interference Effects of a Body on the Spanwise Load Distributions of Two 45° Sweptback Wings of Aspect Ratio 8 From Low-Speed Tests at a Reynolds Number of 4×10^6. NACA RM L51K23, 1952.

27. Griner, Roland F., and Foster, Gerald V.: Low-Speed Longitudinal and Wake Air-Flow Characteristics at a Reynolds Number of 6.0×10^6 of a 52° Sweptback Wing Equipped With Various Spans of Leading-Edge and Trailing-Edge Flaps, a Fuselage, and a Horizontal Tail at Various Vertical Positions. NACA RM L50K29, 1951.

28. Adams, Mac C., and Sears, W. R.: Slender Body Theory - Review and Extension. Jour. Aero. Sci., vol. 20, no. 2, Feb. 1953, pp. 85-98.

29. Recant, Isidore G., and Wallace, Arthur R.: Wind-Tunnel Investigation of the Effect of Vertical Position of the Wing on the Side Flow in the Region of the Vertical Tail. NACA TN 804, 1941.

30. Zlotnick, Martin, and Robinson, Samuel W., Jr.: A Simplified Mathematical Model for Calculating Aerodynamic Loading and Downwash for Wing-Fuselage Combinations With Wings of Arbitrary Plan Form. NACA TN 3057, 1954. (Supersedes NACA RM L52J27a.)

31. Anderson, Adrien E.: Chordwise and Spanwise Loadings Measured at Low Speed on Large Triangular Wings. NACA RM A9B17, 1949.

32. May, Ralph W., Jr., and Hawes, John G.: Low-Speed Pressure Distribution and Flow Investigation for a Large Pitch and Yaw Range of Three Low-Aspect-Ratio Pointed Wings Having Leading Edge Swept Back 60° and Biconvex Sections. NACA RM L9J07, 1949.

33. Kolbe, Carl D., and Boltz, Frederick W.: The Forces and Pressure Distribution at Subsonic Speeds on a Plane Wing Having 45° Sweepback, an Aspect Ratio of 3, and a Taper Ratio of 0.5. NACA RM A51G31, 1951.

34. Hunton, Lynn W., and Dew, Joseph K.: The Effects of Camber and Twist on the Aerodynamic Loading and Stalling Characteristics of a Large-Scale 45° Swept-Back Wing. NACA RM A50J24, 1951.

35. Pratt, George L.: Effects of Twist and Camber on the Low-Speed Longitudinal Stability Characteristics of a 45° Sweptback Wing of Aspect Ratio 8 at Reynolds Numbers From 1.5×10^6 to 4.8×10^6 As Determined by Pressure Distribution, Force Tests, and Calculations. NACA RM L52J03a, 1952.

36. Whittle, Edward F., Jr., and Hawes, John G.: Investigation at Low Speed of the Downwash, Sidewash, and Wake Characteristics Behind a Large-Scale Triangular Wing, Including the Effects of Yaw, Full-Span Trailing-Edge Flaps, and Two Leading-Edge Modifications. NACA RM L52H19, 1952.

37. Newman, Ernest E., and Cahill, Jones F.: Investigation at Low Speed of the Flow Field Behind the Lifting Surfaces of a Model Equipped With a 60° Triangular Wing and a 60° Triangular Canard Tail. NACA RM L53C30, 1953.

38. Frick, J. P.: Downwash and Total-Head Survey Behind a 60° Delta Wing Model in Incompressible Flow. Rep. ZA-198, Consolidated Vultee Aircraft Corp., Aug. 25, 1949.

39. Bird, John D., and Riley, Donald R.: Some Experiments on Visualization of Flow Fields Behind Low-Aspect-Ratio Wings by Means of a Tuft Grid. NACA TN 2674, 1952.

40. Foster, Gerald V.: Longitudinal Stability and Wake-Flow Characteristics of a Twisted and Cambered Wing-Fuselage Combination of 45° Sweepback and Aspect Ratio 8 With a Horizontal Tail and Stall-Control Devices at a Reynolds Number of 4.0×10^6. NACA RM L53D08, 1953.

41. Lagerstrom, P. A., and Graham, M. E.: Aerodynamic Interference in Supersonic Missiles. Rep. No. SM-13743, Douglas Aircraft Co., Inc., July, 1950.

42. Owen, P. R., and Maskell, E. C.: Interference Between the Wings and the Tailplane of a Slender Wing-Body-Tailplane Combination. Rep. No. Aero.2441, British R.A.E., Oct. 1951.

[redacted]

43. Bollech, Thomas V., and Hadaway, William M.: The Low-Speed Lift and Pitching-Moment Characteristics of a 45° Sweptback Wing of Aspect Ratio 8 With and Without High-Lift and Stall-Control Devices as Determined From Pressure Distributions at a Reynolds Number of 4.0×10^6. NACA RM L52K26, 1953.

44. Salmi, Reino J.: Horizontal-Tail Effectiveness and Downwash Surveys for Two 47.7° Sweptback Wing-Fuselage Combinations With Aspect Ratios of 5.1 and 6.0 at a Reynolds Number of 6.0×10^6. NACA RM L50K06, 1951.

45. Foster, Gerald V., and Griner, Roland F.: A Study of Several Factors Affecting the Stability Contributed by a Horizontal Tail at Various Vertical Positions on a Sweptback-Wing Airplane Model. NACA RM L9H19, 1949.

46. Coleman, W. S.: Investigation of the Effect of Full Span, High Lift Flaps on the Flow in the Region of the Tailplane, and upon Stability and Trim. Rep. W.T. 88/43, Blackburn Aircraft Ltd., Aug. 1943.

47. Koven, William, and Graham, Robert R.: Wind-Tunnel Investigation of High-Lift and Stall-Control Devices on a 37° Sweptback Wing of Aspect Ratio 6 at High Reynolds Numbers. NACA RM L8D29, 1948.

48. Lawrence, H. R., and Flax, A. H.: Wing-Body Interference at Subsonic and Supersonic Speeds. - Survey and New Developments. Jour. Aero. Sci., vol. 21, no. 5, May 1954, pp. 289-324.

49. Hadaway, William M., and Cancro, Patrick A.: Low-Speed Longitudinal Characteristics of Two Unswept Wings of Hexagonal Airfoil Sections Having Aspect Ratios of 2.5 and 4.0 With Fuselage and Horizontal Tail Located at Various Vertical Positions. NACA RM L53H14a, 1953.

50. Jaquet, Byron M.: Effects of Horizontal-Tail Position, Area, and Aspect Ratio on Low-Speed Static Longitudinal Stability and Control Characteristics of a 60° Triangular-Wing Model Having Various Triangular-All-Movable Horizontal Tails. NACA RM L51I06, 1951.

51. Mitchell, Jesse L.: The Static and Dynamic Longitudinal Stability Characteristics of Some Supersonic Aircraft Configurations. NACA RM L52A10a, 1952.

52. Foster, Gerald V., Mollenberg, Ernst F., and Woods, Robert L.: Low-Speed Longitudinal Characteristics of an Unswept Hexagonal Wing With and Without a Fuselage and a Horizontal Tail Located at Various Positions at Reynolds Numbers From 2.8×10^6 to 7.6×10^6. NACA RM L52L11b, 1953.

53. McKee, John W., and Riebe, John M.: An Investigation of a 0.16-Scale Model of the Douglas X-3 Airplane To Determine Means of Improving the Low-Speed Longitudinal Stability and Control Characteristics. NACA RM L52H01, 1952.

54. Delany, Noel K., and Hayter, Nora-Lee F.: Low-Speed Investigation of a 0.16-Scale Model of the X-3 Airplane - Longitudinal Characteristics. NACA RM A50G06, 1950.

55. Johnson, Ben H., Jr., and Rollins, Francis W.: Investigation of a Thin Wing of Aspect Ratio 4 in the Ames 12-Foot Pressure Wind Tunnel. V - Static Longitudinal Stability and Control Throughout the Subsonic Speed Range of a Semispan Model of a Supersonic Airplane. NACA RM A9I01, 1949.

56. Weil, Joseph, Campbell, George S., and Diederich, Margaret S.: An Analysis of Estimated and Experimental Transonic Downwash Characteristics As Affected by Plan Form and Thickness for Wing and Wing-Fuselage Configurations. NACA RM L52I22, 1952.

57. Trienes, Hans (With Abstract by H. M. Lyon): Systematic Measurements of Downwash Behind Sweptback Wings. Tech. Note No. Aero.1819, British R.A.E., Aug. 1946. (Addendum, Oct. 1946.)

58. Graham, David, and Koenig, David G.: Tests in the Ames 40- by 80-Foot Wind Tunnel of an Airplane Configuration With an Aspect Ratio 2 Triangular Wing and an All-Movable Horizontal Tail - Longitudinal Characteristics. NACA RM A51B21, 1951.

59. Franks, Ralph W.: Tests in the Ames 40- by 80-Foot Wind Tunnel of Two Airplane Models Having Aspect Ratio 2 Trapezoidal Wings of Taper Ratios 0.33 and 0.20. NACA RM A52L16, 1953.

60. Spooner, Stanley H., and Martina, Albert P.: Longitudinal Stability Characteristics of a 42° Sweptback Wing and Tail Combination at a Reynolds Number of 6.8×10^6. NACA RM L8E12, 1948.

61. Salmi, Reino J., and Jacques, William A.: Effect of Vertical Location of a Horizontal Tail on the Static Longitudinal Stability Characteristics of a 45° Sweptback-Wing—Fuselage Combination of Aspect Ratio 8 at a Reynolds Number of 4.0×10^6. NACA RM L51J08, 1952.

62. Graham, David, and Koenig, David G.: Tests in the Ames 40- by 80-Foot Wind Tunnel of an Airplane Configuration With an Aspect Ratio 4 Triangular Wing and an All-Movable Horizontal Tail - Longitudinal Characteristics. NACA RM A51H10a, 1951.

63. Woods, Robert L., and Spooner, Stanley H.: Effects of High-Lift and Stall-Control Devices, Fuselage, and Horizontal Tail on a Wing Swept Back 42° at the Leading Edge and Having Symmetrical Circular-Arc Airfoil Sections at a Reynolds Number of 6.9×10^6. NACA RM L9B11, 1949.

64. Goodson, Kenneth W., and Few, Albert G., Jr.: Low-Speed Static Longitudinal and Lateral Stability Characteristics of a Model With Leading-Edge Chord-Extensions Incorporated on a 40° Swept-back Circular-Arc Wing of Aspect Ratio 4 and Taper Ratio 0.50. NACA RM L52I18, 1952.

65. Jaquet, Byron M.: Effects of Chord Discontinuities and Chordwise Fences on Low-Speed Static Longitudinal Stability of an Airplane Model Having a 35° Sweptback Wing. NACA RM L52C25, 1952.

66. Foster, Gerald V.: Effects of Twist and Camber, Fences, and Horizontal-Tail Height on the Low-Speed Longitudinal Stability Characteristics of a Wing-Fuselage Combination With a 45° Swept-back Wing of Aspect Ratio 8 at a Reynolds Number of 4.0×10^6. NACA RM L52J03, 1952.

67. Kemp, William B., Jr., Becht, Robert E., and Few, Albert G., Jr.: Investigation of the Low-Speed Aerodynamic Characteristics of a Variable-Sweep Airplane Model With a Twisted and Cambered Wing. NACA RM L51K22, 1952.

68. Tinling, Bruce E.: The Longitudinal Characteristics at Mach Numbers Up to 0.9 of a Wing-Fuselage-Tail Combination Having a Wing With 40° of Sweepback and an Aspect Ratio of 10. NACA RM A52I19, 1952.

69. Bandettini, Angelo, and Selan, Ralph: The Effects of Horizontal-Tail Height and of a Partial-Span Leading-Edge Extension on the Static Longitudinal Stability of a Wing-Fuselage-Tail Combination Having a Sweptback Wing. NACA RM A53J07, 1954.

70. Tinling, Bruce E., and Lopez, Armando E.: The Effects of Horizontal-Tail Location and Size on the Subsonic Longitudinal Aerodynamic Characteristics of an Airplane Model Having a Triangular Wing of Aspect Ratio 3. NACA RM A53L15, 1954.

71. Coppolino, Domenic A.: The Effective Downwash Characteristics at Transonic Speeds of a 6-Percent-Thick Wing With 47° of Sweepback in Combination With a Cylindrical Body as Determined From Force Measurements of a Horizontal Tail. NACA RM L52J15, 1952.

[redacted]

72. Allen, Edwin C.: Investigation of a Triangular Wing in Conjunction With a Fuselage and Horizontal Tail To Determine Downwash and Longitudinal-Stability Characteristics - Transonic Bump Method. NACA RM A51F12a, 1951.

73. Bielat, Ralph P., and Campbell, George S.: A Transonic Wind-Tunnel Investigation of the Longitudinal Stability and Control Characteristics of a 0.09-Scale Model of the Bell X-5 Research Airplane and Comparison With Flight. NACA RM L53H18, 1953.

74. Tinling, Bruce E., and Lopex, Armando E.: The Effects of Nacelles and of Extended Split Flaps on the Longitudinal Characteristics of a Wing-Fuselage-Tail Combination Having a Wing With 40° of Sweepback and an Aspect Ratio of 10. NACA RM A53D06, 1953.

75. Franks, Ralph W.: Test in the Ames 40- by 80-Foot Wind Tunnel of an Airplane Model With an Aspect Ratio 4 Triangular Wing and an All-Movable Horizontal Tail - High-Lift Devices and Lateral Controls. NACA RM A52K13, 1953.

76. Foster, Gerald V., and Fitzpatrick, James E.: Longitudinal-Stability Investigation of High-Lift and Stall-Control Devices on a 52° Sweptback Wing With and Without Fuselage and Horizontal Tail at a Reynolds Number of 6.8×10^6. NACA RM L8I08, 1948.

77. Koenig, David G.: Tests in the Ames 40- by 80-Foot Wind Tunnel of an Airplane Configuration With an Aspect Ratio 3 Triangular Wing and an All-Movable Horizontal Tail - Longitudinal and Lateral Characteristics. NACA RM A52L15, 1953.

78. Trouncer, J., and Moss, G. F.: Low-Speed Wind-Tunnel Tests on Two 45 Deg Sweptback Wings of Aspect Ratios 4.5 and 3.0 (Models A and B). R. & M. 2710, British A.R.C., June 1947.

79. Weil, Joseph, Comisarow, Paul, and Goodson, Kenneth W.: Longitudinal Stability and Control Characteristics of an Airplane Model Having a 42.8° Sweptback Circular-Arc Wing With Aspect Ratio 4.00, Taper Ratio 0.50, and Sweptback Tail Surfaces. NACA RM L7G28, 1947.

TABLE I.- INDEX OF AIR-FLOW DATA OBTAINED FROM LOW-SPEED SURVEYS AT REYNOLDS NUMBER GREATER THAN 4.0×10^6

Wing geometry					Stall-control devices		Trailing-edge flaps		Body	Survey location, $\frac{x_0}{b/2}$	Test conditions		Quantities presented in reference	Figure number	Reference
Λ_{LE}	$\Lambda_{c/4}$	A	λ	[a]Airfoil	Span (b)	Type	Span (b)	Type			R	Maximum α, deg			
3.6	0	4.62	0.550	Root: NACA 0015 Tip: NACA 23009	-----	None	-----	None	None	1.286	5.5×10^6	14.5	c and wake limits	----------	8
9.5	4.8	4.00	.500	Wedge	-----	None	-----	None	On	1.819	2.0×10^6 to 10.0×10^6	14.1	Wake center line and limits	----------	55 55
					.000	L.E. flap	0.609	Plain							
33.3	30.0	4.84	.440	Root: NACA 0015 Tip: NACA 23009	-----	None	-----	None	None	1.243	6.4×10^6	15.9	c and wake limits	----------	8
37.3	35.0	6.00	.500	[b]NACA 64_1-212	.500	Slat	.500	Double slotted	None	0.690	6.8	15.2	c and c_l/q	----------	47
42.0	40.0	4.01	.625	[b]NACA 64_1-112	-----	None	-----	None	None	1.020	6.8	16.0	c, σ, and c_l/q	4, 5	24
					.575	L.E. flap	.500	Split	None	1.020		16.8		24, 25, 26	24
					.575	L.E. flap	.500	Split	None	1.420		16.0		26	24
					-----	None	-----	None	None	1.420		16.8		----------	24
					.575	L.E. flap	.500	Split	On	.980		19.5		24, 25	45
46.3	45.0	8.00	.450	NACA 63-X12 Twisted and cambered	-----	None Fence	-----	None Extended Split	On	.790	4.0	25.1 25.2	c, σ, and c_l/q	10(c), 13, 14(d)	40
47.5	45.0	3.50	.500	[b]Circular arc	-----	None	-----	None	None	.544	4.3	18.0	c and c_l/q	----------	25
					-----	None	-----	None		.857		18.0		----------	
					-----	None	-----	None		1.130		18.0		10(b), 12, 14(b), 17	
					1.000	L.E. droop	-----	None		.544		22.0		----------	
					1.000	L.E. droop	-----	None		1.130		22.0		----------	
					1.000	L.E. droop	.500	Plain		1.230		21.5		----------	
47.7	45.0	5.10	.383	[b]NACA 64-210	-----	None	-----	None	On	.876	6.0	25.1	c, σ, and c_l/q	22, 23	44
					.475	L.E. flap	-----	None				25.2		22, 25, 27	
					.475	L.E. flap	.400	Split				25.3		----------	
					.475	L.E. flap	.400	Double slotted				25.3		27, 35	
48.0	45.0	3.64	.420	Root: NACA 0015 Tip: NACA 23009	-----	None	-----	None	None	1.638	8.0	21.1	c and wake limits	----------	8
52.0	50.0	2.88	.625	[b]NACA 64_1-112	-----	None	-----	None	On	1.168	6.0	25.1	c, σ, and c_l/q	14(c), 36	27
					.400	L.E. flap	.400	Split							
52.0	50.0	2.84	.616	[b]Circular arc	-----	None	-----	None	On	1.228	5.5	19.0	c, σ, and c_l/q	----------	13
					.250	L.E. flap	.400	Split							
60.0	52.4	2.31	0	Circular arc	-----	None	-----	None	None	.610	6.0	27.7	c, σ, and c_l/q	11(d)	36
				Circular arc			-----	None	None	1.210	6.0	27.7		11(c)	36
				Circular arc			-----	None	None	1.820	6 0	27.7		10(a), 11(a), 11(b)	36
				Circular arc			1.000	Plain	None	1.210	6 0	21.6		14(a), 15	36
				NACA 65-006.5			-----	None	None	1.210	6.0	22.1		----------	38
				NACA 65-010			-----	None	None	1.210	6.0	22.1		----------	38
				NACA 65A006			-----	None	On	1.440	9.0	33.9		----------	37
				NACA 65A006			-----	None	On	2.040	9.0	33.9		----------	37
63.0	60.8	3.50	.250	NACA 64A006	-----	None	-----	None	On	.570	6.2	10.5	c and vortex sheet shape	----------	21
										.720		10.6			
										.980		10.8			
										1.110		10.9			
										1.310		11.0			
										1.650		11.2			
										2.000		11.5			
										2.360		11.8			
										2.710		12.0			

[a]Streamwise sections unless otherwise noted.
[b]Airfoil sections normal to chord line in the 0.25c to 0.55c range.
[c]Ground effects for several ground heights.

TABLE II.- INDEX OF THE HORIZONTAL-TAIL AIR-FLOW CHARACTERISTICS AND TAIL STABILITY PARAMETERS OBTAINED FROM LOW-SPEED FORCE TESTS AT REYNOLDS NUMBERS GREATER THAN 4.0×10^6

Wing geometry					Stall-control device	Trailing-edge flaps	Wing position
Λ_{LE}	$A_c/4$	A	λ	[a]Airfoil			
6.6	3.4	4.00	0.625	Hexagonal	L.E. droop	Plain	Mid
9.5	4.8	4.00	.500	Wedge	L.E. droop	Plain	Mid
10.5	5.3	2.50	.625	Hexagonal	L.E. droop	Plain	Mid
42.4	40.0	10.00	.400	[b]Root: Mod. NACA 0014 Tip: Mod. NACA 0011 Twisted and cambered	Fences	Extended split	High
42.0	40.0	4.01	.625	[b]NACA 64_1-112	L.E. flaps L.E. flaps and fences L.E. flaps, slats and fences L.E. flaps	Split	High Mid Low Mid
42.0	40.0	3.94	.625	[b]Circular arc	L.E. flaps, L.E. droop, fences	Split	Low
45.0	36.9	4.00	0	Mod. NACA 0005	----------	Slotted and plain	Mid
45.0	36.9	2.00	.330	Mod. NACA 0005	----------	Slotted	Mid
46.3	45.0	8.00	.450	NACA 63_1A012 NACA 63 series Twisted and cambered	L.E. flaps, fences	Split and extended split	Medium high
47.7 47.7	45.0 45.0	5.10 6.00	.383 .313	[b]NACA 64-210 [b]NACA 64-210	L.E. flaps, L.E. droop L.E. flaps	Split and double slotted	Mid
52.0	50.0	2.88	.625	[b]NACA 64_1-112	L.E. flaps, fences	Split Split Split and extended split	Mid Low Mid
52.0	50.0	2.84	.616	[b]Circular arc	L.E. flaps	Split and extended split	Mid
53.2	45.0	2.00	.200	Mod. NACA 0005	----------	Slotted	Mid
53.2	45.0	3.00	0	Mod. NACA 0005	----------	Slotted	Mid
63.4	56.3	2.00	0	Mod. NACA 0005	----------	Slotted	Mid

[a]Streamwise sections unless otherwise noted.
[b]Airfoil sections normal to chord line in the 0.25c to 0.33c range.
[c]Ground effects for several ground heights (see fig. 56).

TABLE II.- INDEX OF THE HORIZONTAL-TAIL AIR-FLOW CHARACTERISTICS AND TAIL STABILITY PARAMETERS OBTAINED FROM LOW-SPEED FORCE TESTS AT REYNOLDS NUMBERS GREATER THAN 4.0×10^6 - Concluded

Tail geometry and location					R	Figure number	Reference
Plan form	b_t/b	l/c'	$2l/b$	$2h/b$			
Straight Tapered	0.50	3.260	1.660	.400, .177, -.177	6.2×10^6	38, 46, 52	49
Straight Tapered	.50	3.385	1.755	.362 and 0	10.0	----------	55
Straight Tapered	.50	2.000 3.000	1.630 2.441	.400, .177, -.177	7.6	38, 41, 46, 52 38, 46	52
Sweptback	.30	3.250	.699	.050 and 0 .150, .100, .050, 0	2.0×10^6 to 8.0×10^6 4.0×10^6	28 ----------	68 74
Sweptback	.40	2.000	1.018	.254, -.146 .417, .162, -.061 .509, .254, .031 .417, .162, -.061	6.8	46, 52 43, 46, 52, 58 46, 47 ----------	[c]60 [c]60 [c]60 45
Sweptback	.40	2.000	1.033	.466, .339, .211, -.011	6.9	44, 46, 47	63
Straight Tapered	.45 .52 .32 .39 .32	1.910	1.275	.360, .180 0 .360, .180 0 0	10.9	44, 47 ---------- ---------- ---------- 52	62 62 62 62 75
Straight Tapered	.67 .78 .78	1.820	1.975	.537, .269 0 0	12.4	42, 46, 47, 59 ---------- 52	59
Sweptback	.28	3.000	.767	.300, .140, .045, -.060 .300, .140, .045, -.060, -.150	4.0	43, 46, 47, 51, 52, 53, 54 30, 31, 51	61, 66 40, 66
Sweptback	.37 .33	2.222 2.220	.928 .799	.380, -.050 .340, -.050	6.0	46, 47, 48, 52, 53, 54 ----------	44
Sweptback	.48	1.736	1.229	.504, .372, .196, -.074 .625, .482, .307, -.037 .504, .196, -.074	6.8 6.8 6.0	46, 47 ---------- 30, 31, 46, 45, 47, 52	76 76 27
Sweptback	.48	1.696	1.229	.442, .136, -.132	5.5	41, 45, 46, 47, 52	43
Straight Tapered	.65 .75 .75	1.720	1.978	.516, .259 0 0	13.0	46, 47 ---------- 52	59
Straight Tapered	.50 .60	1.751	1.560	.41, .21 0	12.8	46, 47, 54 46, 47, 54	77
Straight Tapered	.63 .74	1.351	1.800	.506, .254 0	14.6	42, 46, 47 28, 42, 46, 47	58

TABLE III.- INDEX OF FIGURES

Figure	Ordinate	Abscissa	Description
1	--	--	Schematic representation of trailing vortex sheet behind wings.
2	$\frac{2z}{b}$	$\frac{ds}{d\alpha}$	Experimental and calculated downwash behind unstalled low-aspect-ratio wings.
3	$\frac{2z_{TE}}{b}$	$\frac{2y}{b}$	Experimental positions of the tip vortex behind three sweptback wings with unseparated flow.
4	$\frac{d\epsilon}{d\alpha}$, $\frac{2z_{TE}}{b}$	$\frac{2y}{b}$, ϵ	Experimental and calculated downwash behind an unstalled 40-4.0-.63 wing.
5	$\frac{2z}{b}$	$\frac{2y}{b}$	Contours of dynamic-pressure ratio and the calculated positions of the vortex sheet behind an unstalled 40-4.0-.63 wing.
6	$57.3\frac{d\left(\frac{z}{y}\right)_{vor}}{d\alpha}$	Λ	Effect of wing sweep on wake location in linear C_L range.
7	$\frac{d\epsilon}{d\alpha}$	$\frac{2y}{b}$	Calculated components of downwash behind a 50-2.9-.63 wing mounted on a circular cylinder.
8	$\frac{c_l c}{a\bar{c}}$	$\frac{2y}{b}$	Calculated load distribution for a 50-2.9-.63 wing and wing-body combination.
9	$\frac{d\epsilon}{d\alpha}$	$\frac{2y}{b}$	Experimental and calculated downwash behind a 50-2.9-.63 wing-body combination at low angles of attack.
10	$\frac{c_l c}{\bar{c}}$, ϵ_{max}, C_m	$\frac{2y}{b}$, α, α	Experimental maximum downwash, load distribution, and pitching-moment characteristics for three sweptback wings.
11	$\frac{2z}{b}$	$\frac{2y}{b}$	Flow characteristics at several longitudinal stations behind a stalled 60° delta wing.
12	$\frac{2z}{b}$	$\frac{2y}{b}$	Flow characteristics behind a stalled 45-3.5-.50 wing.
13	$\frac{2z}{b}$	$\frac{2y}{b}$	Flow characteristics behind a stalled 45-3.0-.45 wing-body combination.
14	$\frac{2z_{TE}}{b}$	ϵ	Downwash profiles at several angles of attack behind four sweptback wings.
15	ϵ_{max}, vertical distance from maximum ϵ	α, ϵ	Experimental and calculated downwash behind a 60° delta wing.
16	$\frac{c_l c}{C_L \bar{c}}$	$\frac{2y}{b}$	Circulation distribution on and behind a stalled 45-3.5-.50 wing.
17	ϵ_{max}	α	Experimental and calculated downwash behind a 45-3.5-.50 wing.
18	$\frac{2z_{TE}}{b}$	ϵ	Downwash and dynamic pressure ratio profiles at two longitudinal stations behind a stalled 3.4-4.0-.63 wing.
19	ϵ_{max}	α	Maximum downwash behind a 3.4-4.0-.63 wing and wing-body combination.
20	$\frac{2z_{TE}}{b}$	ϵ	Downwash and dynamic-pressure-ratio profiles behind a stalled 3.4-4.0-.63 wing and wing-body combination.
21	$\frac{c_l c}{\bar{c}}$	$\frac{2y}{b}$	Effect of leading-edge flaps on the experimental load distribution of a stalled 45-8.0-.45 wing.
22	ϵ_{max}, $\left(\frac{q_t}{q}\right)_{min}$	$\frac{2y}{b}$	Effect of leading-edge flaps on the spanwise variation of ϵ_{max} and $\left(\frac{q_t}{q}\right)_{min}$ behind a stalled 45-5.1-.38 wing-body combination.
23	ϵ_{max}	α	Effect of leading-edge flaps on the variation of ϵ_{max} with angle of attack for a 45-5.1-.38 wing-body combination.
24	$\frac{2z_{TE}}{b}$	ϵ	Downwash at a low angle of attack behind a 40-4.0-.63 wing and wing-body combination with trailing-edge split flaps.
25	$\frac{2z}{b}$	$\frac{2y}{b}$	Contours of dynamic-pressure ratio at low angle of attack behind a 40-4.0-.63 wing and wing-body combination with trailing-edge split flaps.
26	Distance from wake center line	$\frac{q_t}{q}$	Experimental and calculated dynamic-pressure characteristics at several lateral and longitudinal stations behind a 40-4.0-.63 wing with trailing-edge split flaps.
27	Downwash profile, $\frac{2z}{b}$	$\frac{2y}{b}$	Effect of double slotted trailing-edge flaps on the downwash and wake characteristics of a 45.1-5.1-.38 wing-body combination at several angles of attack.
28	$\eta\left(\frac{q_t}{q}\right)_e$	$\frac{d_t}{c_t}$	Summary of values of $\eta\left(\frac{q_t}{q}\right)_e$ obtained with tail surfaces mounted on bodies.
29	ϵ	α	Calculated downwash at tail due to a pair of vortices.
30	ϵ_e	α	Effective downwash for three sweptback wing-body combinations.

TABLE III.- INDEX OF FIGURES - Concluded

Figure	Ordinate	Abscissa	Description
31	$\eta\left(\frac{q_t}{q}\right)_e$, $\frac{d\varepsilon_e}{d\alpha}$	α	Values of $\eta\left(\frac{q_t}{q}\right)_e$ and $\frac{d\varepsilon_e}{d\alpha}$ for three sweptback wing-body combinations.
32	$\frac{2h}{b}$	Distance from T.E. of wing mean aerodynamic chord	Maximum tail height for no destabilizing change in $\frac{d\varepsilon}{d\alpha}$ of various sweptback wing-body combinations.
33	$\frac{2h}{b}$	$\frac{d\varepsilon_e}{d\alpha}$	Illustration showing the variation of the maximum value of $\frac{d\varepsilon_e}{d\alpha}$ with tail location.
34	ε_e	α	Effect of tail length on the effective downwash of a 52.4-2.3-0 wing-body combination.
35	$\frac{2h}{b}$, $\frac{h}{m}$	max. $\frac{d\varepsilon_e}{d\alpha}$	Effect of tail length on the maximum value of $\frac{d\varepsilon_e}{d\alpha}$ for a 52.8-2.3-0 wing-body combination.
36	$\frac{2z}{b}$	$\frac{2y}{b}$	Contours of $\frac{d\varepsilon}{d\alpha}$ behind a stalled 40-2.9-.63 wing-body combination.
37	τ, ε_e	α	Effect of tail dihedral on the stability parameter and the effective downwash of a 40-3.5-.58 wing-body combination.
38	ε_e, $\eta\left(\frac{q_t}{q}\right)_e$, τ	α	Tail characteristics of several unswept wing-body combinations.
39	ε	α	Variations of downwash at several spanwise stations and heights behind a 3.4-4.0-.63 wing with and without a body.
40	$\frac{\pi A}{57.3}\frac{d\varepsilon}{dC_L}$ $\frac{\varepsilon}{\varepsilon_{A=0}}$ at constant α	A	Effect of wing plan-form variables on the calculated wing downwash at a low angle of attack.
41	ε_e, $\eta\left(\frac{q_t}{q}\right)_e$, τ	α	Effect of variation of wing sweep from 5° to 50° on tail characteristics of wing-body combinations.
42	$-\left(1-\frac{d\varepsilon_e}{d\alpha}\right)$, ε_e	α	Effect of the variation of wing sweep from 37° to 56° on tail characteristics of wing-body combinations.
43	τ, ε_e	α	Effect of wing aspect ratio on tail characteristics of sweptback wing-body combinations.
44	ε_e	α	Effect of wing taper ratio on ε_e of sweptback wing-body combinations.
45	ε_e, τ	α	Effect of wing airfoil section on tail characteristics of sweptback wing-body combinations.
46	$\frac{\pi A}{57.3}\frac{d\varepsilon_e}{dC_L}$	$\frac{2h}{b}$	Summary of downwash characteristics for wing-body combinations at low angles of attack.
47	$\frac{h}{m}$	$\frac{\left(\frac{d\varepsilon_e}{d\alpha}\right)_{stalled}}{\left(\frac{d\varepsilon_e}{dc}\right)_{\frac{z}{c}=0}}$	Summary of $\frac{d\varepsilon}{d\alpha}$ in the stalled range of lift coefficients for various sweptback wing-body combinations.
48	ε_e, τ	α	Effect of wing leading-edge flaps on tail characteristics of a 45-5.1-.38 wing-body combination.
49	τ	α	Effect of wing leading-edge chord extensions on the tail stability parameter of a 40-3.5-.58 wing-body combination.
50	τ	α	Effect of wing fences on the tail stability parameter of a 40-3.5-.58 wing-body combination.
51	ε_e, τ	α	Effect of wing twist and camber on tail characteristics of a 45-8.0-.45 wing-body combination.
52	$\frac{\Delta\varepsilon_e}{\Delta C_L\left/A\frac{b_f}{b}\right.}$	$\frac{2h}{b}$	Summary of data on downwash due to trailing-edge flaps on wing-body combinations at $\alpha = 0$.
53	τ, ε_e	α	Effect of trailing-edge flaps on tail characteristics of several 45° sweptback wing-body combinations with the horizontal tail mounted in a high position.
54	τ, ε_e	α	Effect of trailing-edge flaps on tail characteristics of several 45° sweptback wing-body combinations with the horizontal tail mounted in a low position.
55	$\frac{2z}{b}$	$\frac{2y}{b}$	Contours of $\frac{d\varepsilon}{d\alpha}$ behind a 45-5.1-.38 wing-body combination with double slotted flaps.
56	ε_e	α	Effect of ground on the downwash behind a sweptback wing-body combination.
57	ε, C_m	α	Idealized illustration of the improvement in pitching-moment characteristics by the horizontal tail.
58	ε_e, C_m	α	Effect of a horizontal tail on pitching-moment characteristics of configurations having unstable sweptback wings.
59	ε_e, C_m	α	Effect of a horizontal tail on pitching-moment characteristics of configurations having stable sweptback wings.

TABLE IV.- DATA ON MAXIMUM TAIL HEIGHT FOR NO

DESTABILIZING CHANGE OF $\frac{d\epsilon}{d\alpha}$

Wing	Airfoil section	$2l/b$	Maximum tail height, $\frac{b}{2}$	α_1, deg (a)	Wake-center location at α_1, $\frac{b}{2}$ (b)	α_2, deg (c)	Wake-center location at α_2, $\frac{b}{2}$ (b)
40-4.0-.63	NACA 64_1-112	1.02	0.10	17	0.10	17	0.10
45-3.5-.50	Circular arc	1.21	.07	10	.10	9	.09
45-5.1-.38	NACA 64-210	.88	.13	15	.14	13	.12
50-2.9-.63	NACA 64_1-112	1.17	.15	18	.14	18	.14
50-2.8-.63	Circular arc	1.23	.05	8	.06	10	.08
52.4-2.3-0	NACA $65_{(006)}$-006.5	1.74	.12	12	.10	--	---

[a]Angle of attack for increase in $\frac{d\epsilon_{max}}{d\alpha}$.

[b]Location measured from chord plane at $\frac{2y}{b} = 0.25$.

[c]Angle of attack for unstable C_m change of tail-off configuration.

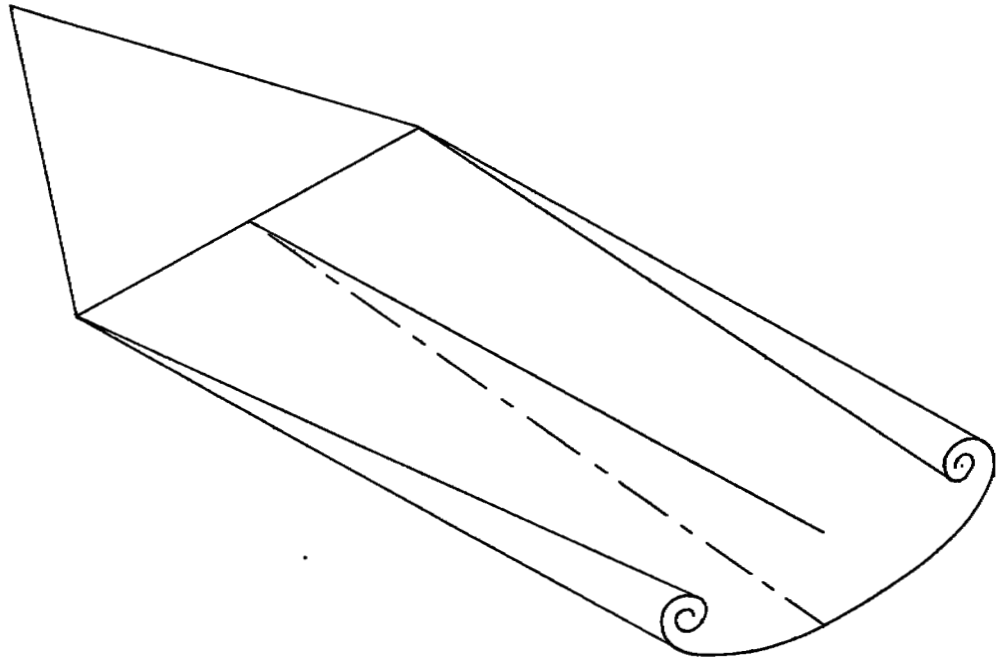

(a) Wings with unswept trailing edges.

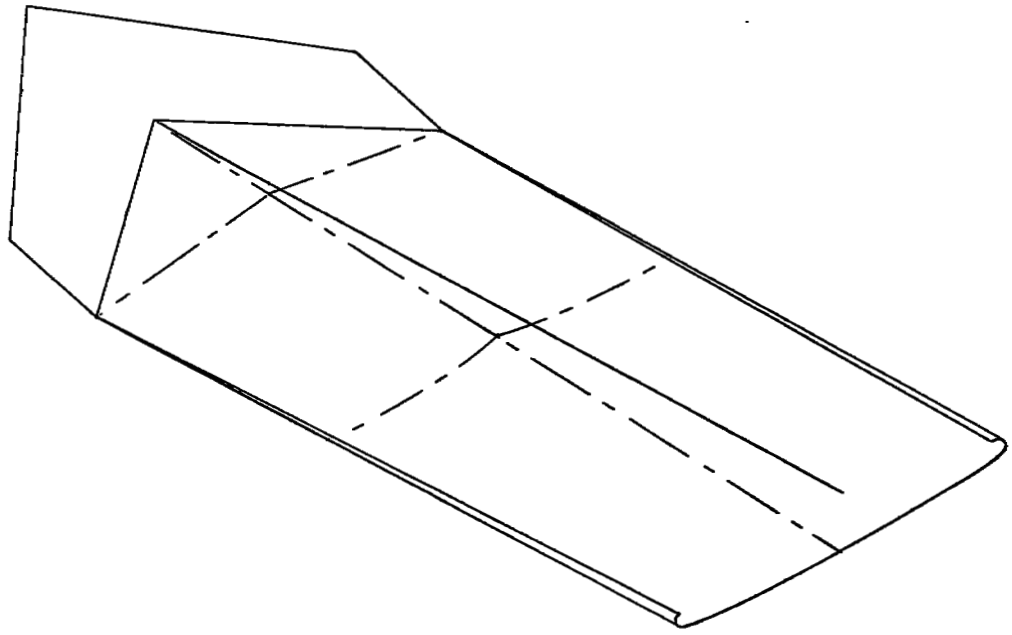

(b) Sweptback wings with sweptback trailing edges.

Figure 1.- Schematic representation of trailing vortex sheet behind wings.

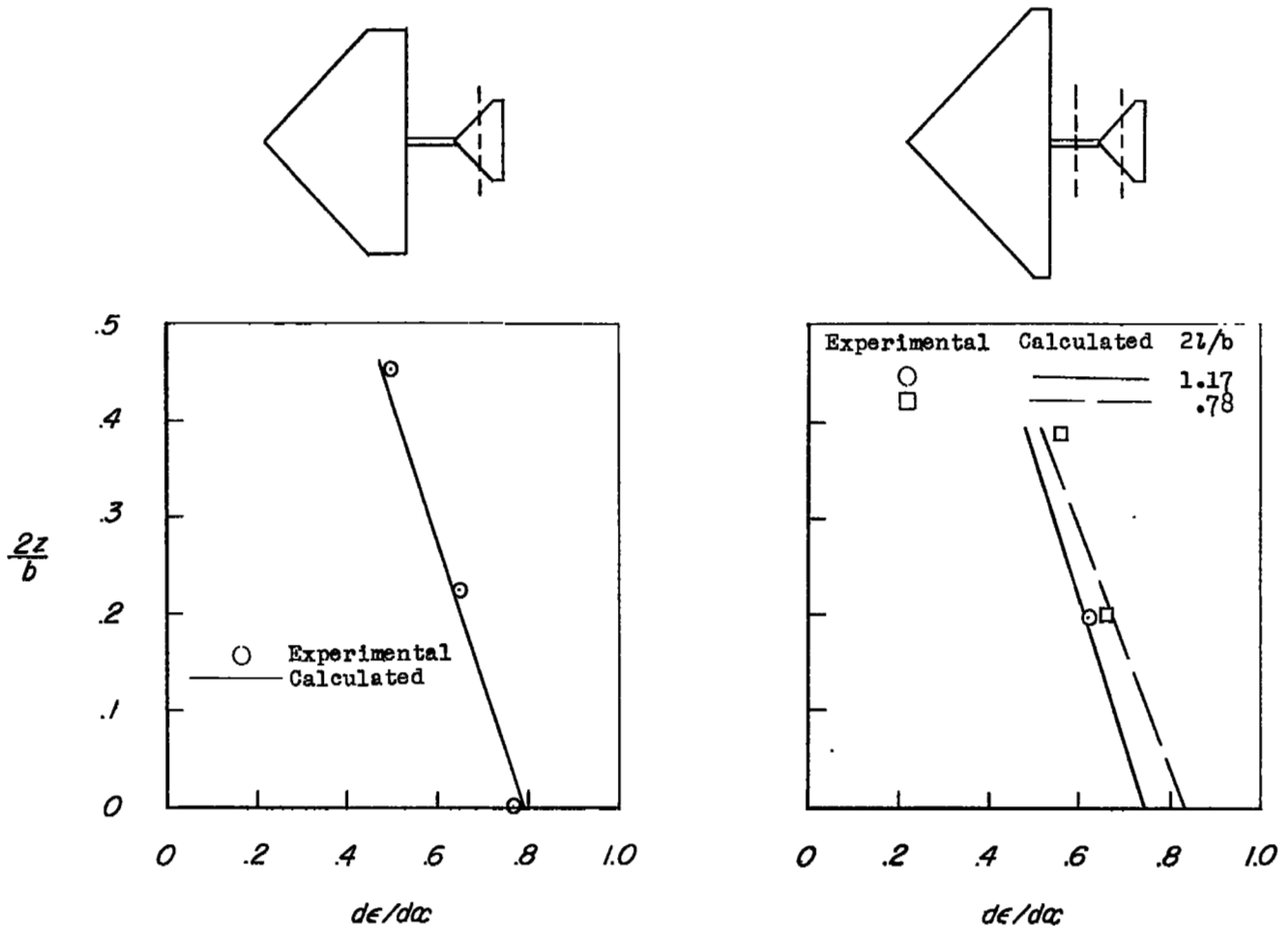

(a) 36.8-2.3-.25; 2l/b = 1.37. (b) 36.8-3.0-.14.

Figure 2.- Comparison of experimental and calculated downwash behind unstalled low-aspect-ratio sweptback wings. Reference 18.

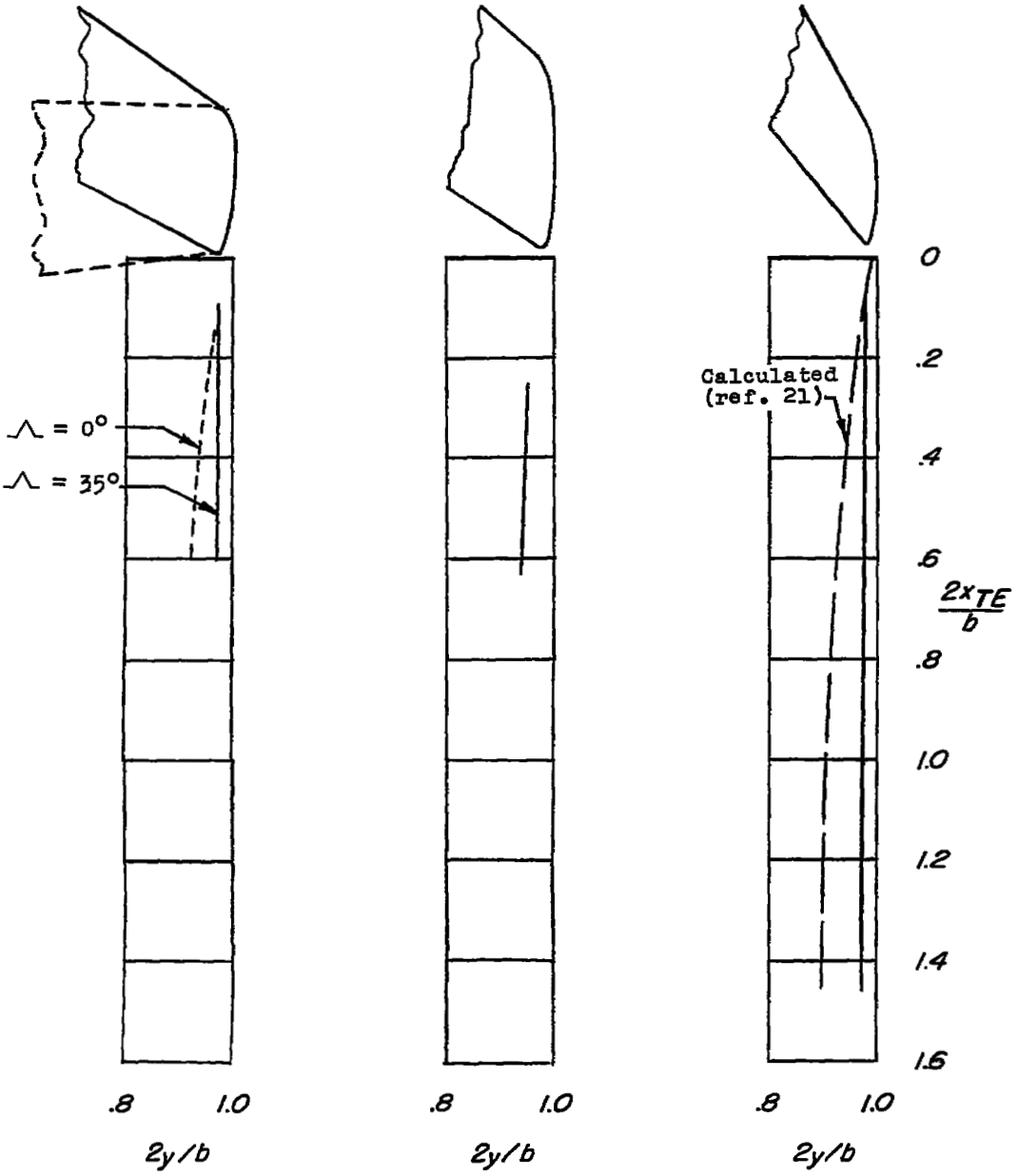

(a) 35-5.1-.50; $C_L = 0.47$; maximum $\frac{x_{TE}}{b}\frac{C_L}{A} = 0.042$; reference 22.

(b) 40-4.0-.63; $C_L = 0.97$; maximum $\frac{x_{TE}}{b}\frac{C_L}{A} = 0.078$; reference 14.

(c) 60.8-3.5-.25; $C_L = 0.50$; maximum $\frac{x_{TE}}{b}\frac{C_L}{A} = 0.107$; reference 21.

Figure 3.- Experimental positions of the tip vortex behind three sweptback wings with unseparated flow.

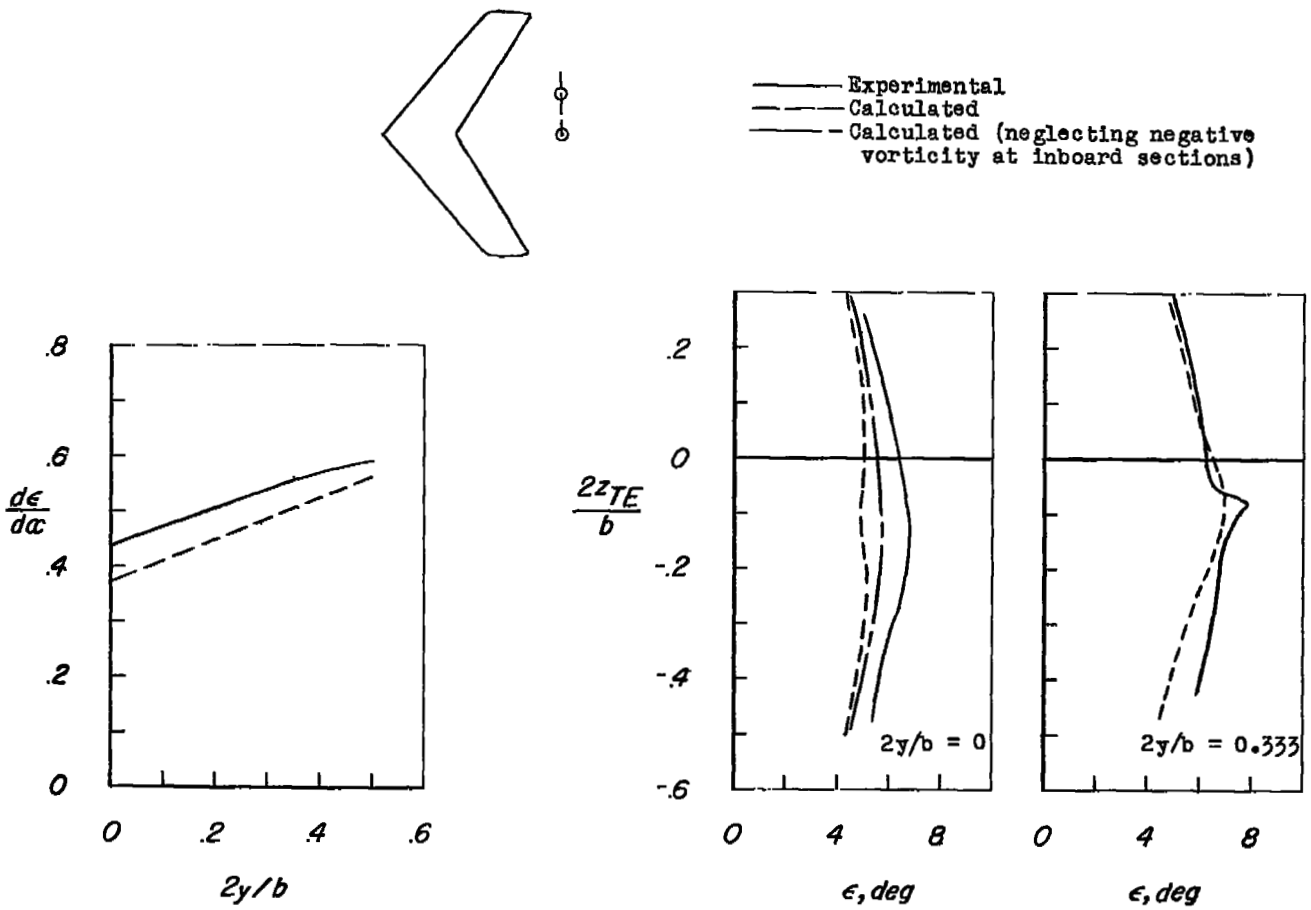

(a) $d\epsilon/d\alpha$ at vortex-sheet center line against $2y/b$.

(b) Downwash profiles; $C_L = 0.81$; $\alpha = 13.1^\circ$.

Figure 4.- Comparison of experimental and calculated downwash behind an unstalled 40-4.0-.63 wing having NACA 64_1-112 airfoil sections normal to the 0.273 chord line. $2x_0/b = 1.04$; reference 14.

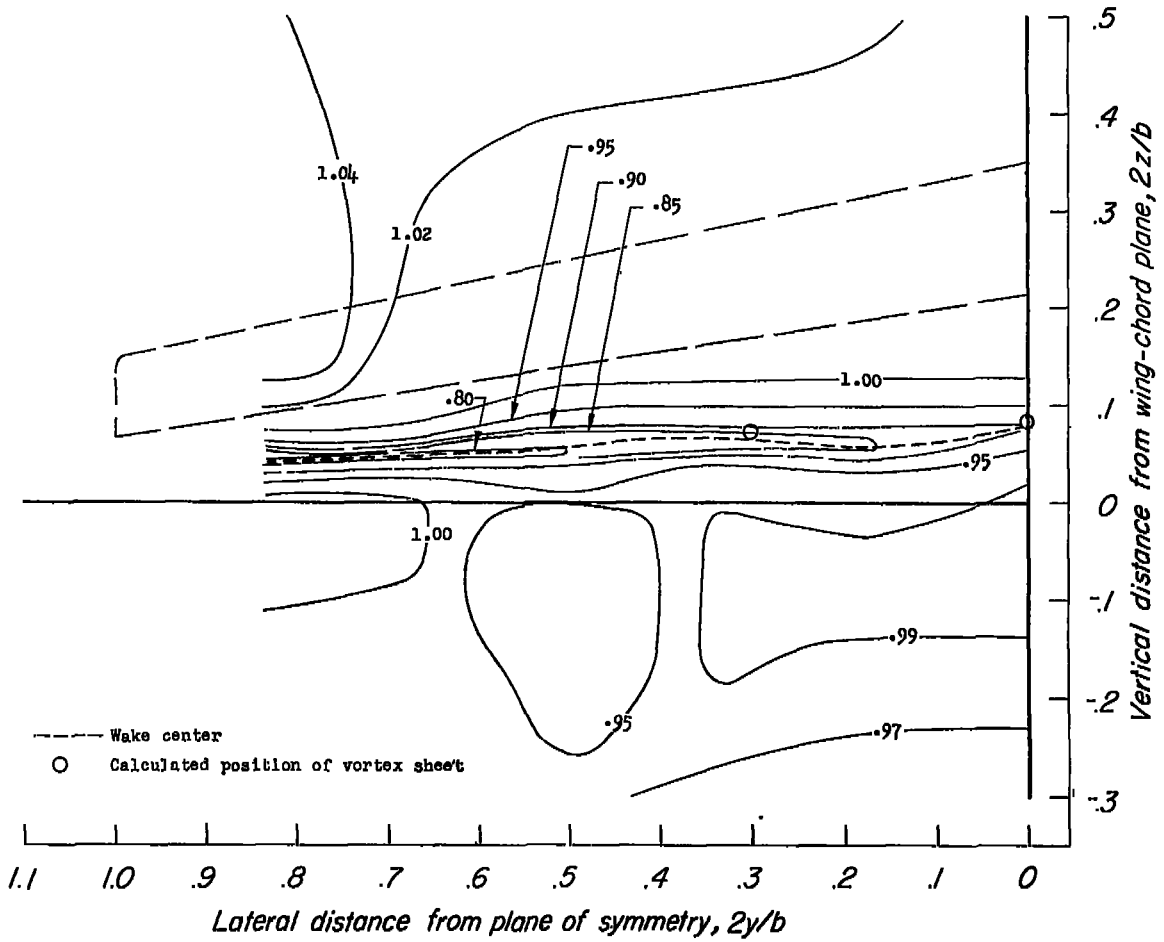

Figure 5.- Contours of dynamic-pressure ratio behind an unstalled 40-4.0-.63 wing having NACA 64_1-112 airfoil sections normal to the 0.273 chord line. $\alpha = 13.1^\circ$; $C_L = 0.81$; $2x_0/b = 1.04$; $R = 6.8 \times 10^6$; reference 14.

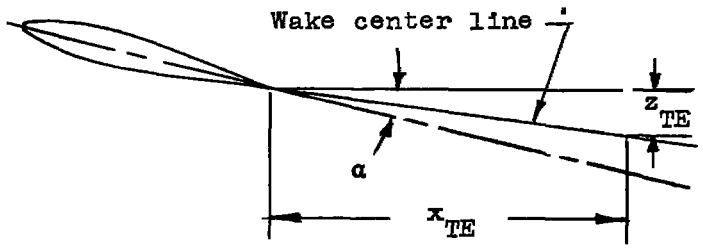

	Wing	Reference
○	0-3.0-1.00	9
□	40-4.0- .63	14
◇	45-3.5- .50	23
△	50-2.9- .63	27
▽	60-3.0-1.00	9
▷	60-3.5- .25	21

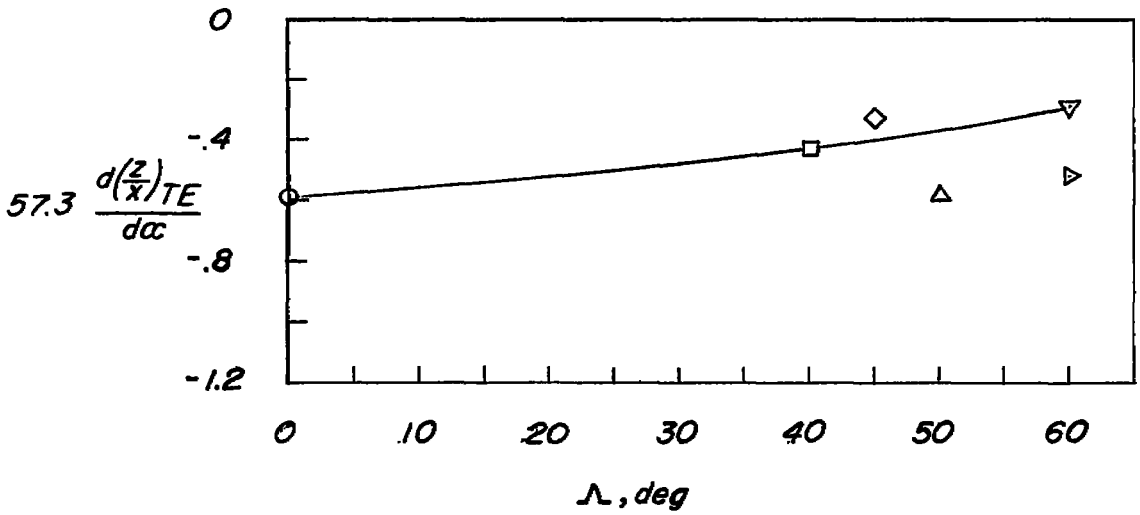

Figure 6.- Effect of wing sweep on wake location in linear lift-coefficient range. A = 3 to 4; 2y/b = 0.25.

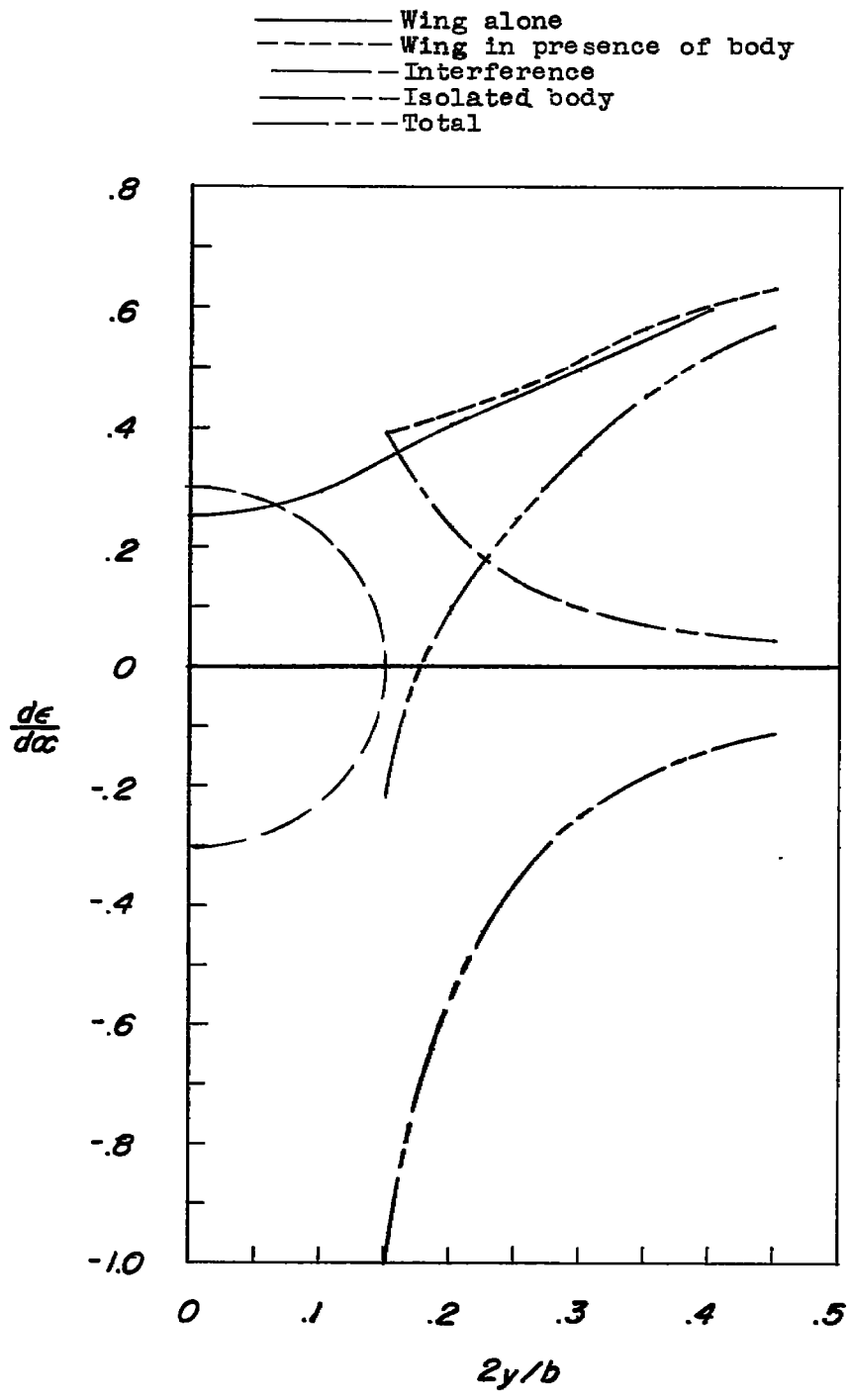

Figure 7.- Calculated downwash behind a 50-2.9-.63 wing centrally mounted on an infinite circular cylinder. $x = \infty$; $z = 0$.

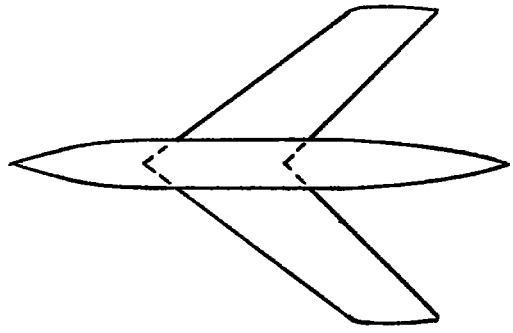

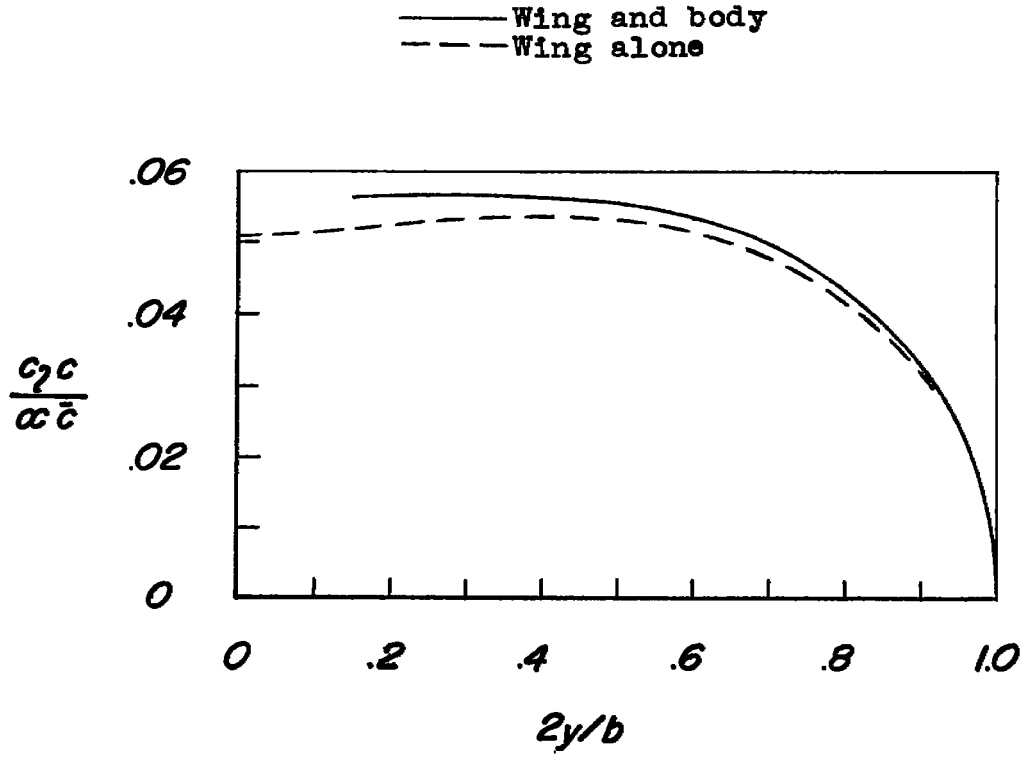

Figure 8.- Calculated load distribution for a 50-2.9-.63 wing and wing-body combination. d/b = 0.15.

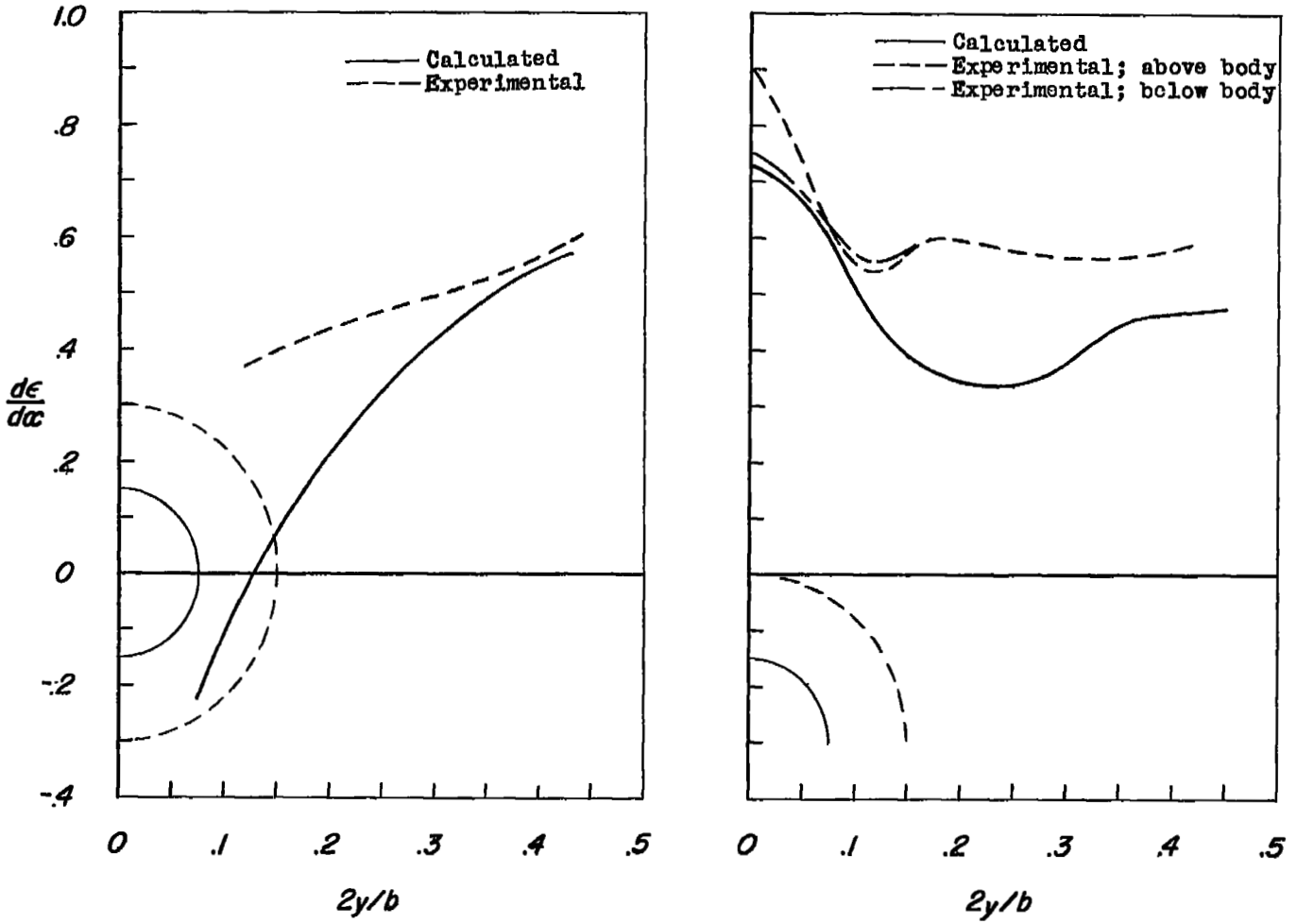

(a) Plane at center of body. (b) Plane at 0.15b/2 from center of body.

Figure 9.- Comparison of experimental and calculated downwash characteristics behind a 50-2.9-.63 wing-body combination.

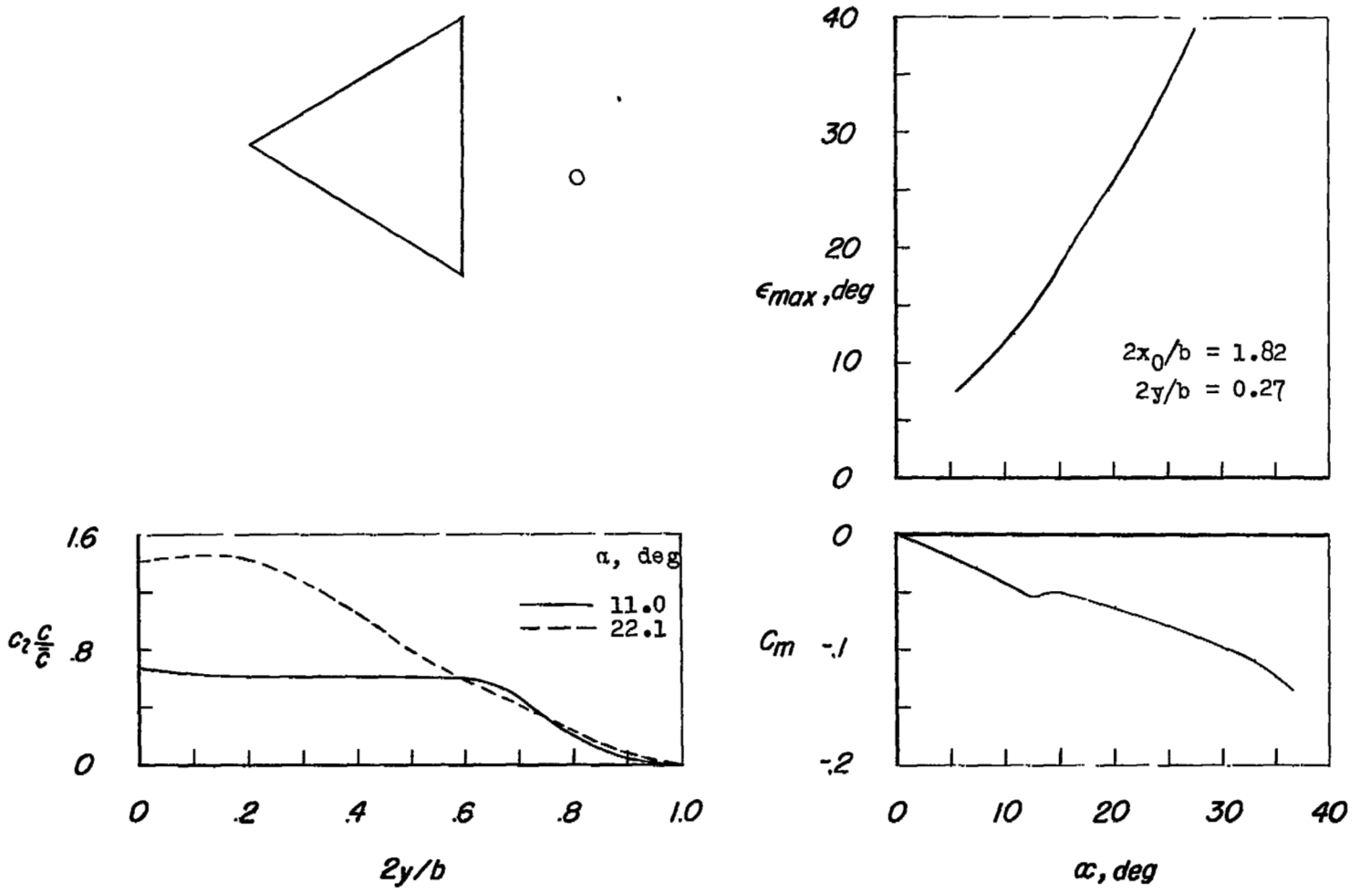

(a) 52.4-2.3-0 wing having 10-percent-thick circular airfoil sections. $R = 6.0 \times 10^6$; references 32 and 36.

Figure 10.- Experimental maximum downwash, load distribution, and pitching-moment characteristics for three sweptback wings.

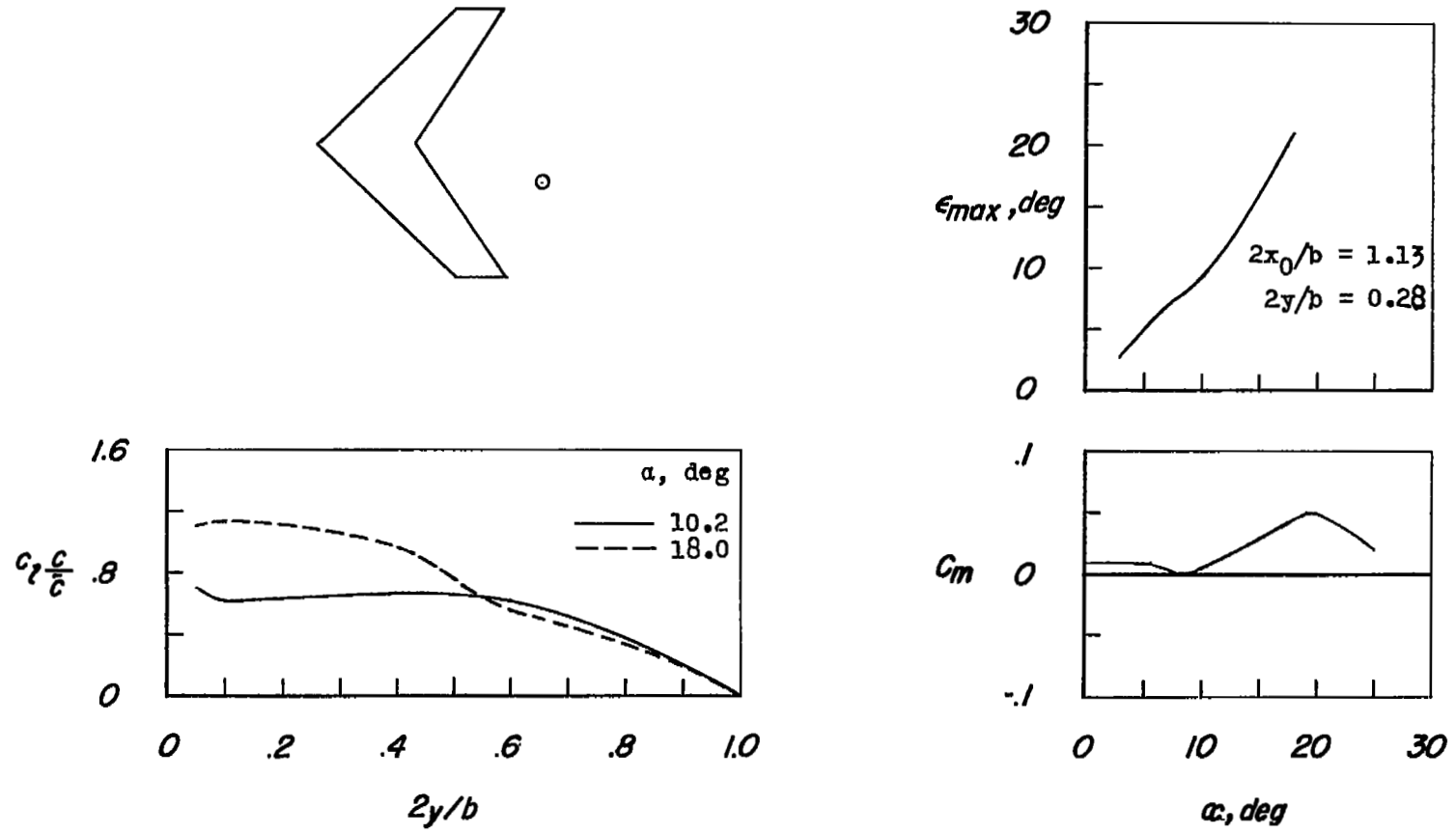

(b) 45-3.5-.50 wing having 10-percent-thick circular-arc airfoil sections normal to line of maximum thickness. R = 4.3×10^6; reference 23.

Figure 10.- Continued.

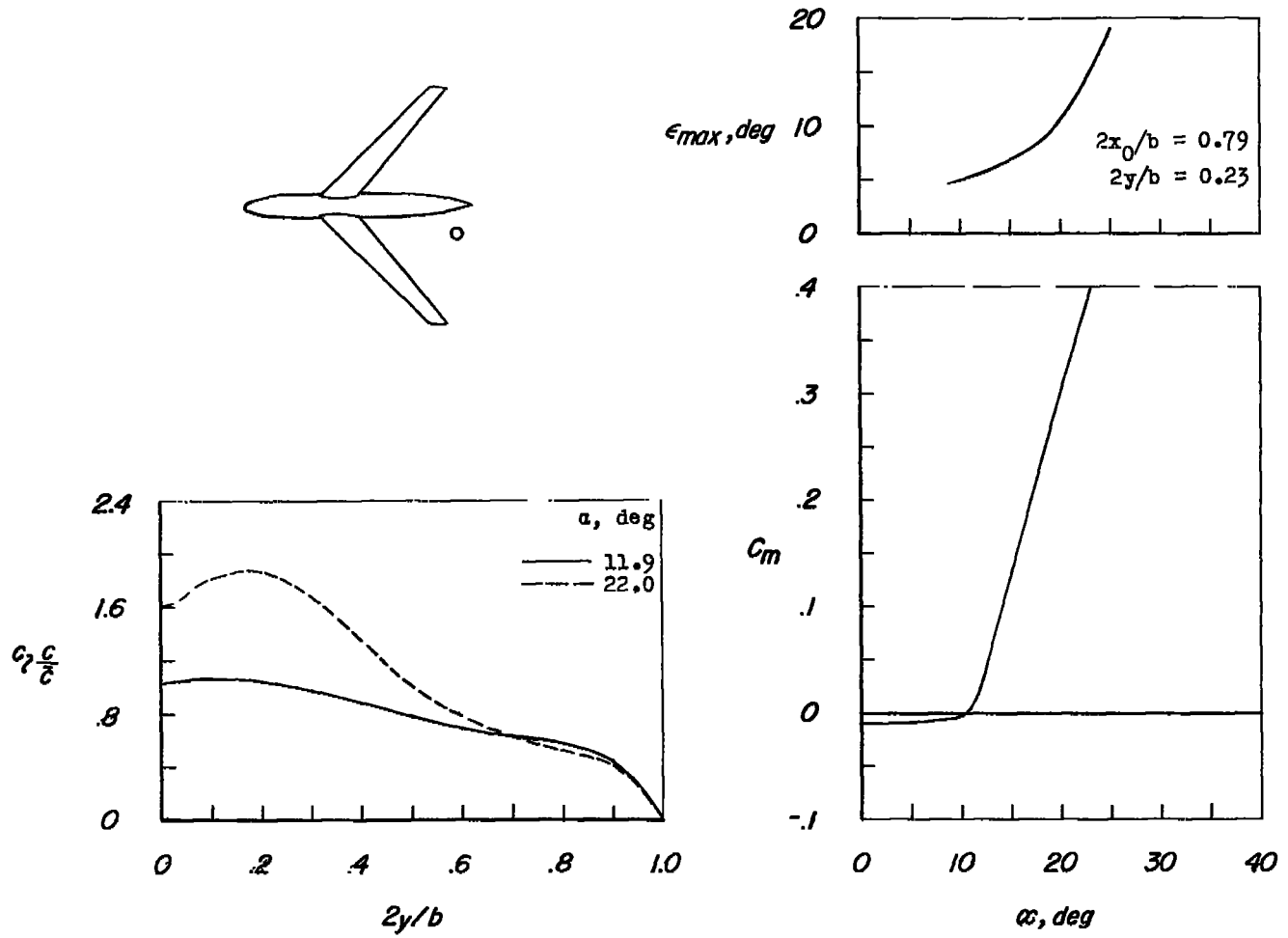

(c) 45-8.0-.45 wing-body combination incorporating a 12-percent-thick wing with twist and camber. $R = 4.0 = 10^6$; references 35 and 40.

Figure 10.- Concluded.

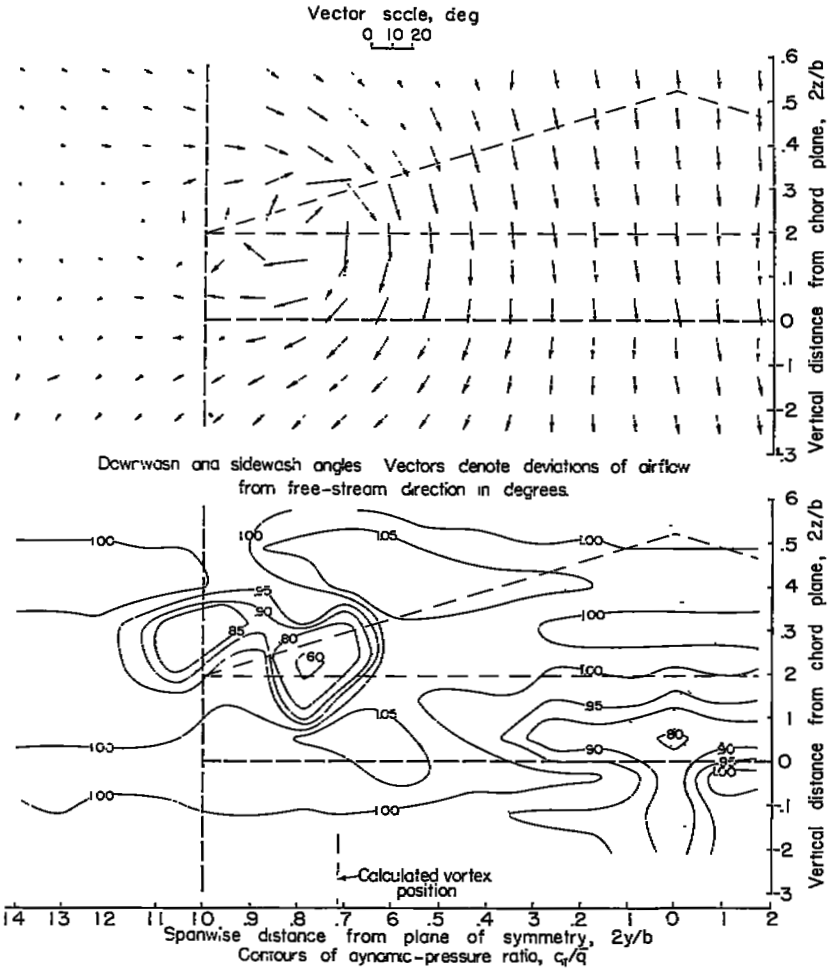

(a) $\alpha = 11.0^{\circ}$; $C_L = 0.47$; $2x_0/b = 1.82$; $\frac{x_{TE}}{b}\frac{C_L}{A} = 0.100$.

Figure 11.- Flow characteristics behind a stalled 60° delta 52.4-2.3-0 wing having 10-percent-thick circular-arc airfoil sections. $R = 6.0 \times 10^6$; reference 36.

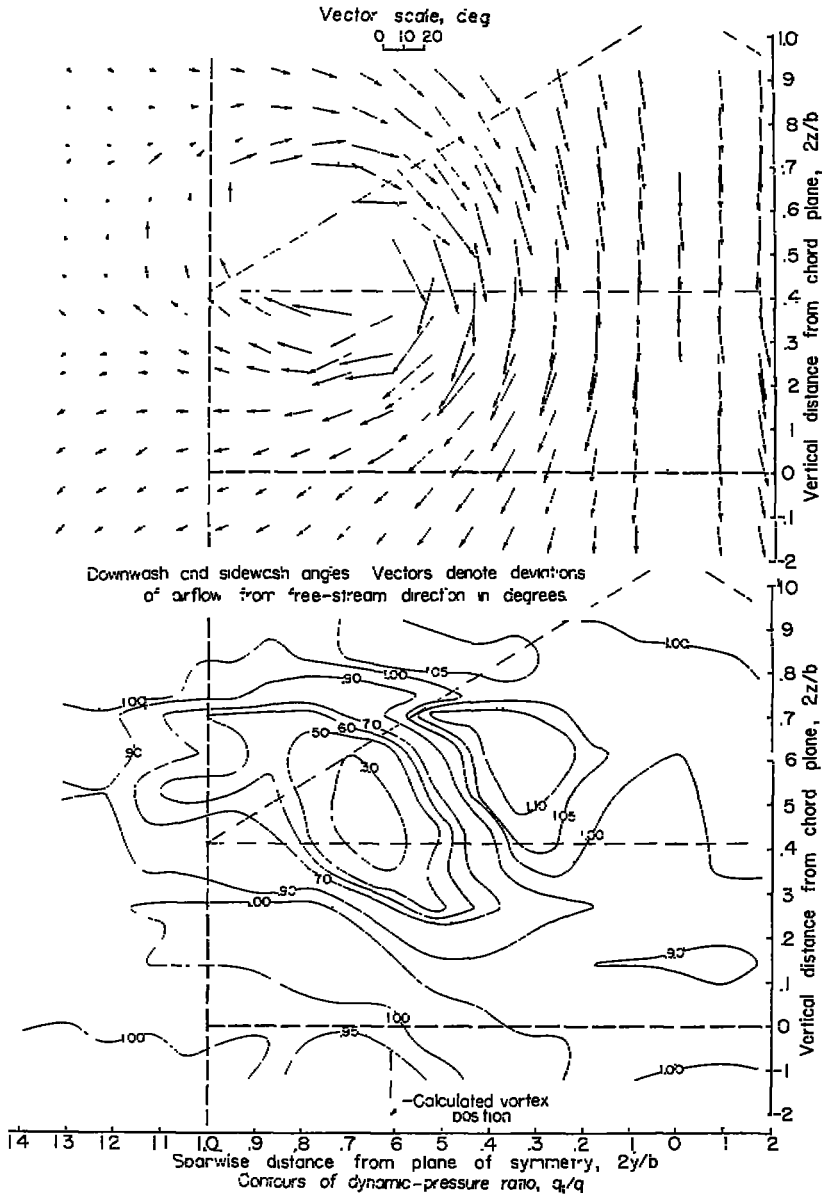

(b) $\alpha = 22.1^\circ$; $C_L = 0.86$; $2x_0/b = 1.82$; $\frac{x_{TE}}{b}\frac{C_L}{A} = 0.184$.

Figure 11.- Continued.

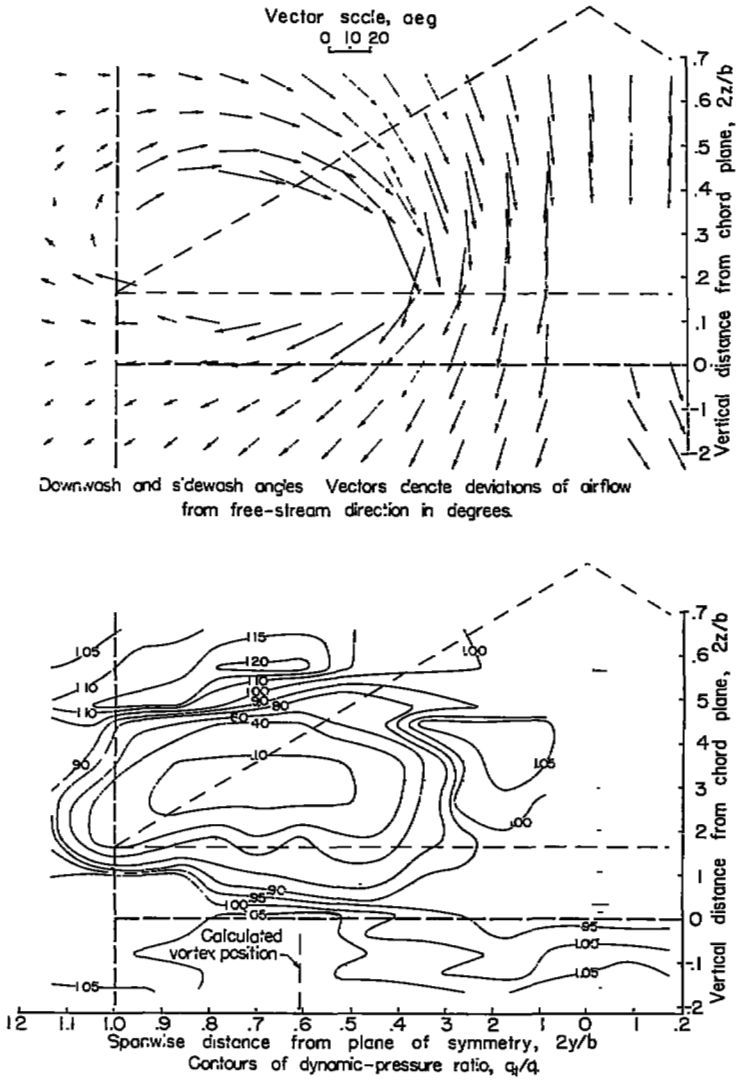

(c) $\alpha = 22.1°$; $C_L = 0.86$; $2x_0/b = 1.21$; $\frac{x_{TE}}{b}\frac{C_L}{A} = 0.071$.

Figure 11.- Continued.

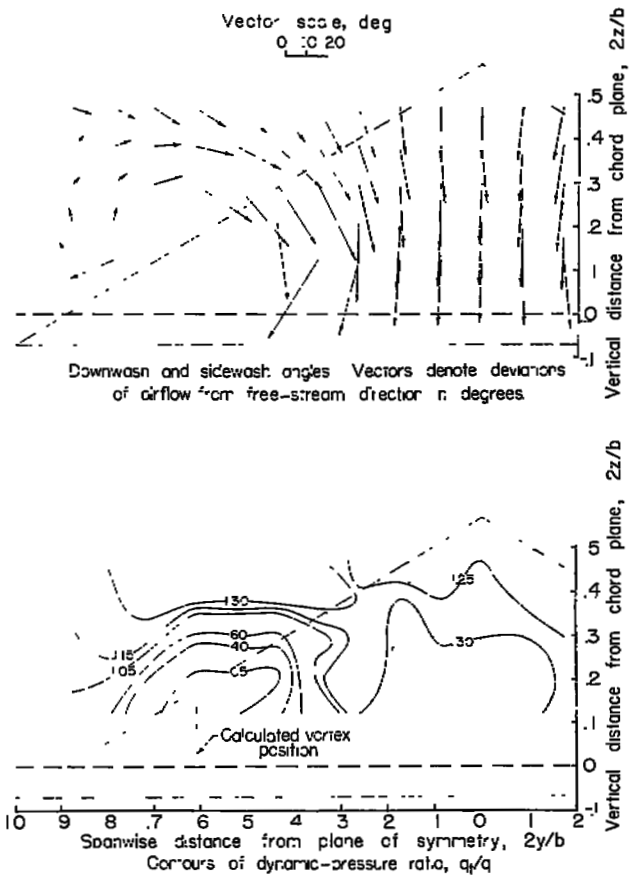

(d) $\alpha = 22.1^\circ$; $C_L = 0.86$; $2x_O/b = 0.61$; $\frac{x_{TE}}{b}\frac{C_L}{A} = -0.040$.

Figure 11.- Concluded.

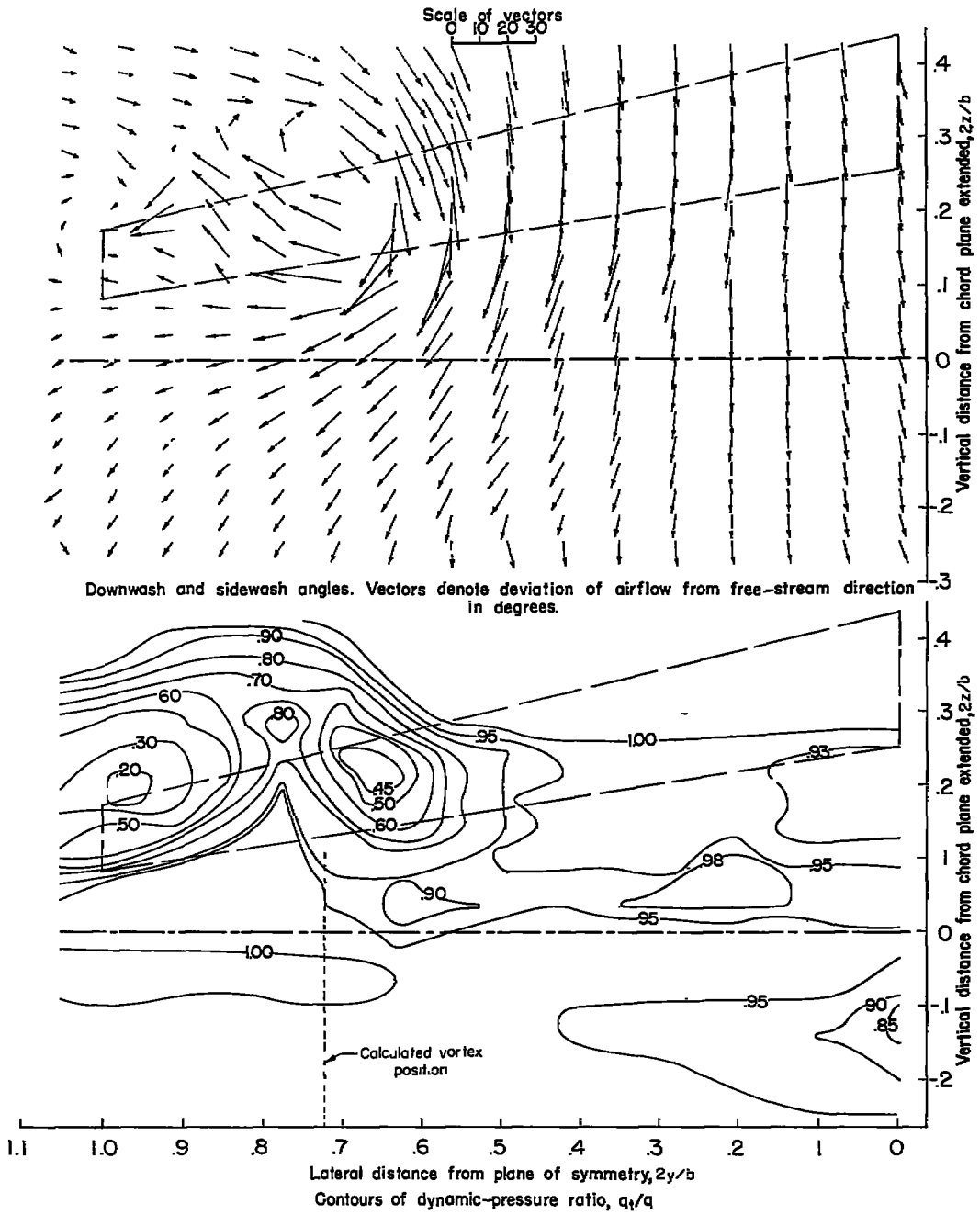

Figure 12.- Flow characteristics behind a stalled 45-3.5-.50 wing having 10-percent-thick circular-arc airfoil sections. $\alpha = 14.0^{\circ}$; $C_L = 0.69$; $2x_O/b = 1.13$; $\frac{x_{TE}}{b}\frac{C_L}{A} = 0.078$; x_{TE} measured at mean aerodynamic chord; $R = 4.3 \times 10^6$; reference 23.

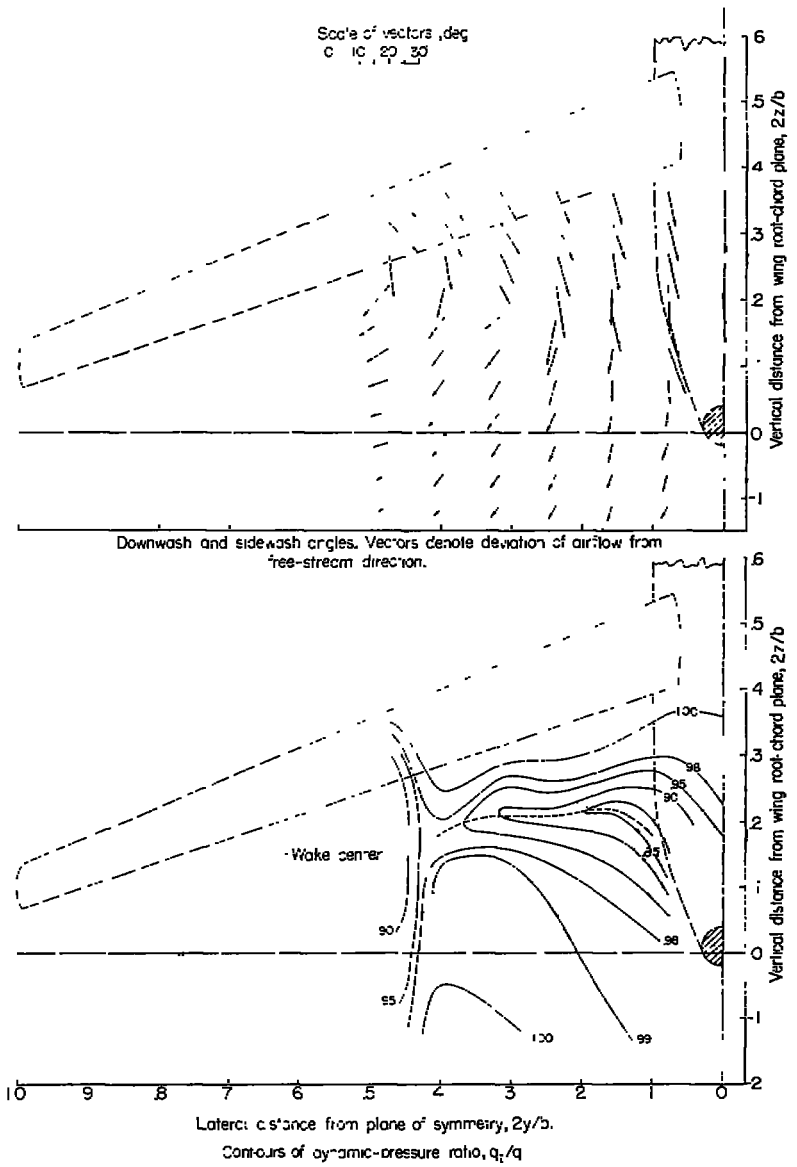

Figure 13.- Flow characteristics behind a stalled 45-8.0-.45 wing-body combination incorporating a 12-percent-thick wing with twist and camber. $\alpha = 25.1^{\circ}$; $C_L = 1.25$; $2x_0/b = 0.79$; $\frac{x_{TE}}{b}\frac{C_L}{A} = 0.056$; x_{TE} measured at mean aerodynamic chord; $R = 4.0 \times 10^6$; reference 40.

[redacted]

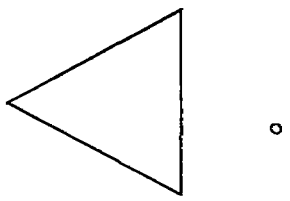

Airfoil: circular-arc

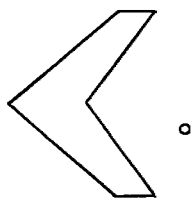

Airfoil: circular-arc

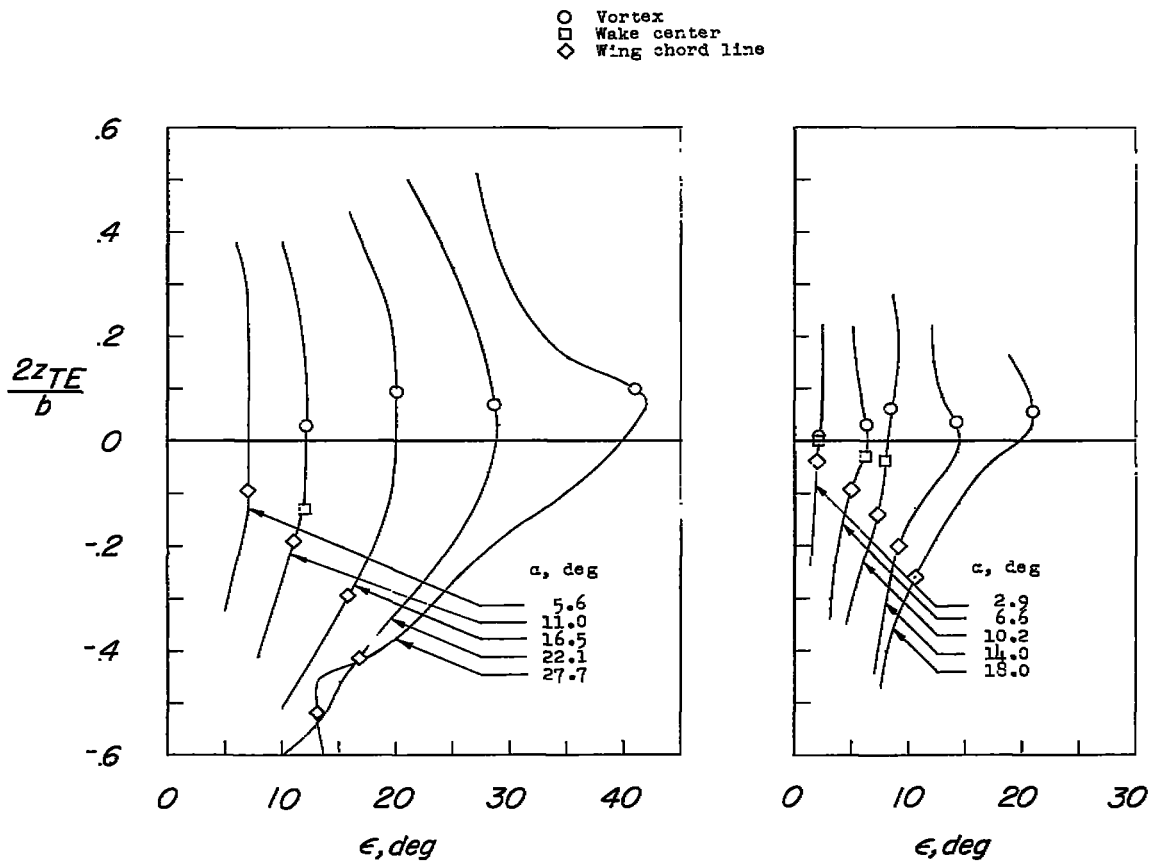

(a) 52.4-2.3-0; $2y/b = 0.27$; $2x_0/b = 1.82$; $R = 6.0 \times 10^6$; reference 36.

(b) 45-3.5-.50; $2y/b = 0.28$; $2x_0/b = 1.13$; $R = 4.3 \times 10^6$; reference 23.

Figure 14.- Downwash profiles at several angles of attack behind four sweptback wings.

[redacted]

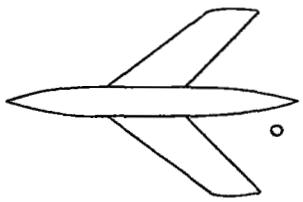

Airfoil: NACA 64_1-112
(normal to 0.25 chord line)

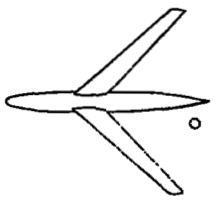

Airfoil: NACA 63-series with twist and camber

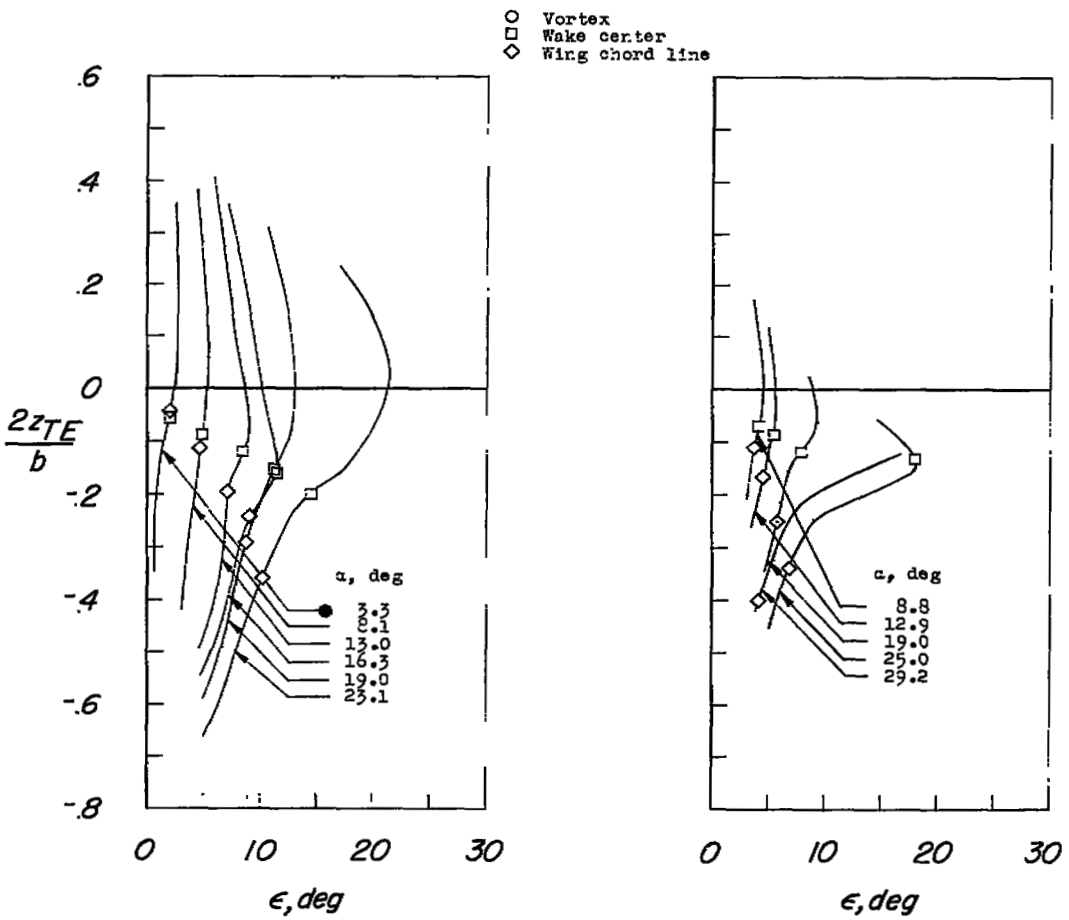

(c) 50-2.9-.63; $2y/b = 0.313$; $2x_0/b = 1.168$; $R = 6.0 \times 10^6$; reference 27.

(d) 45-8.0-.45; $2y/b = 0.23$; $2x_0/b = 0.79$; $R = 4.0 \times 10^6$; reference 40.

Figure 14.- Concluded.

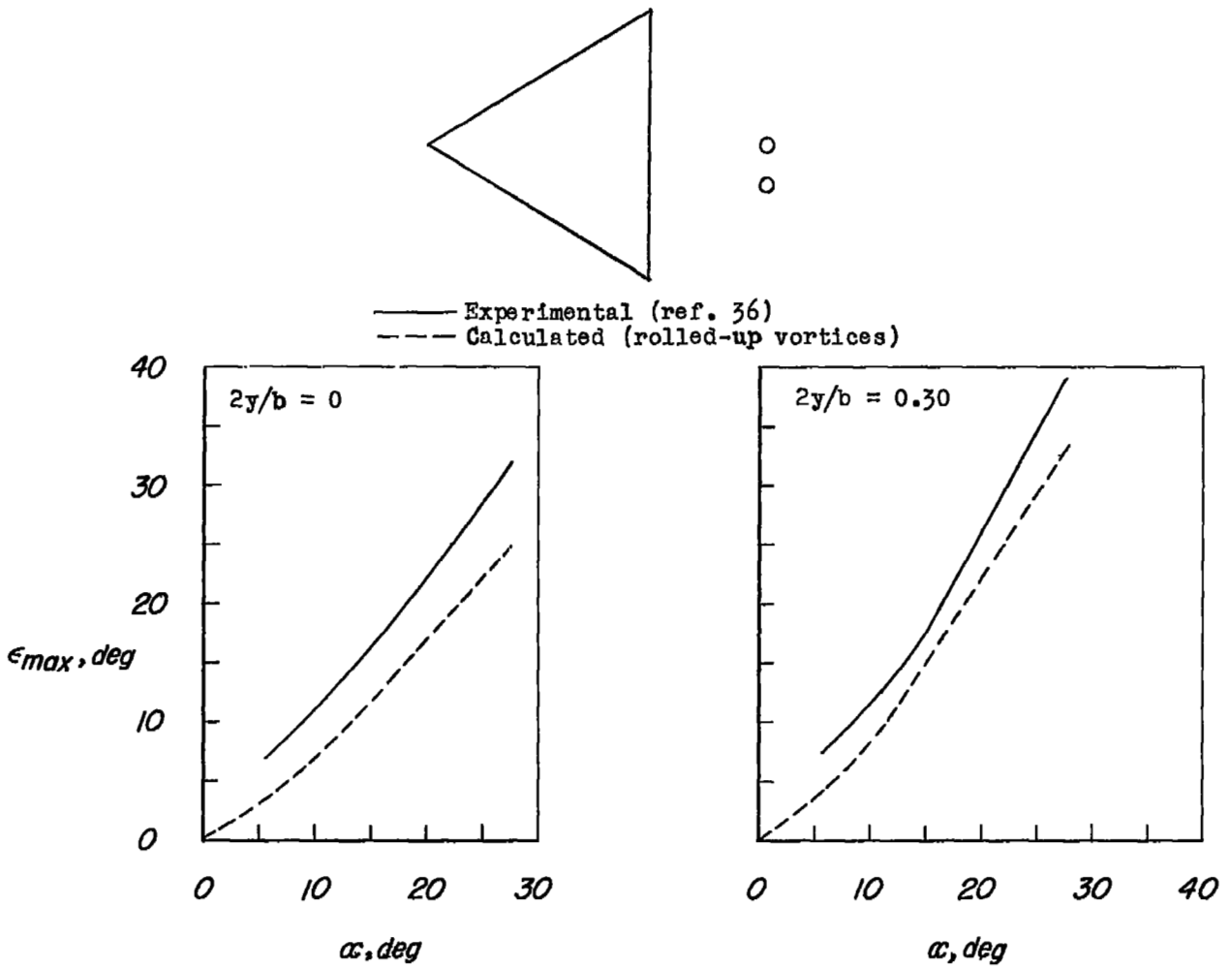

(a) ϵ_{max} against α.

Figure 15.- Comparison of experimental and calculated downwash behind a 52.4-2.3-0 wing having circular-arc airfoil sections. $2x_0/b = 1.82$.

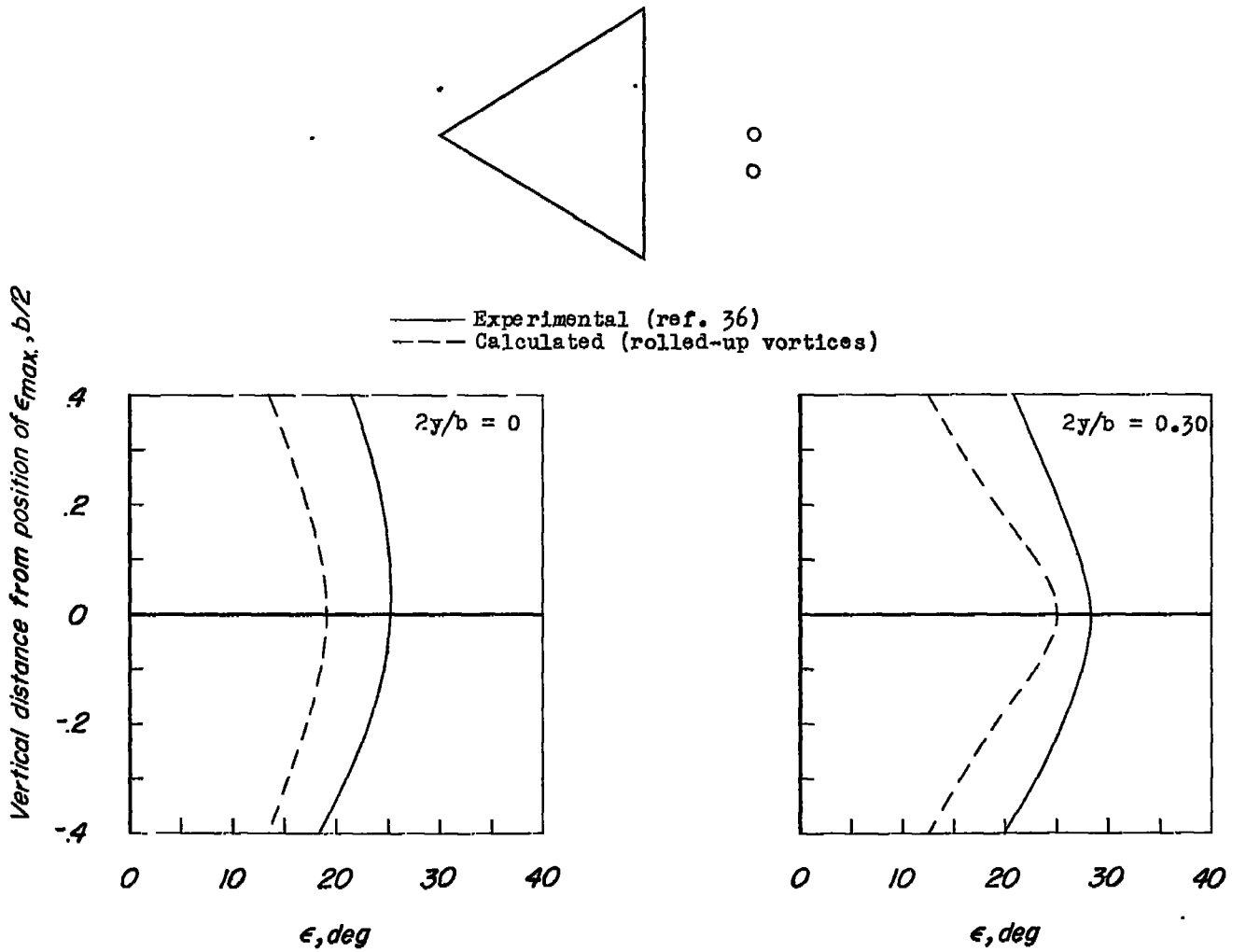

(b) Downwash profiles at $\alpha = 22^{\circ}$.

Figure 15.- Concluded.

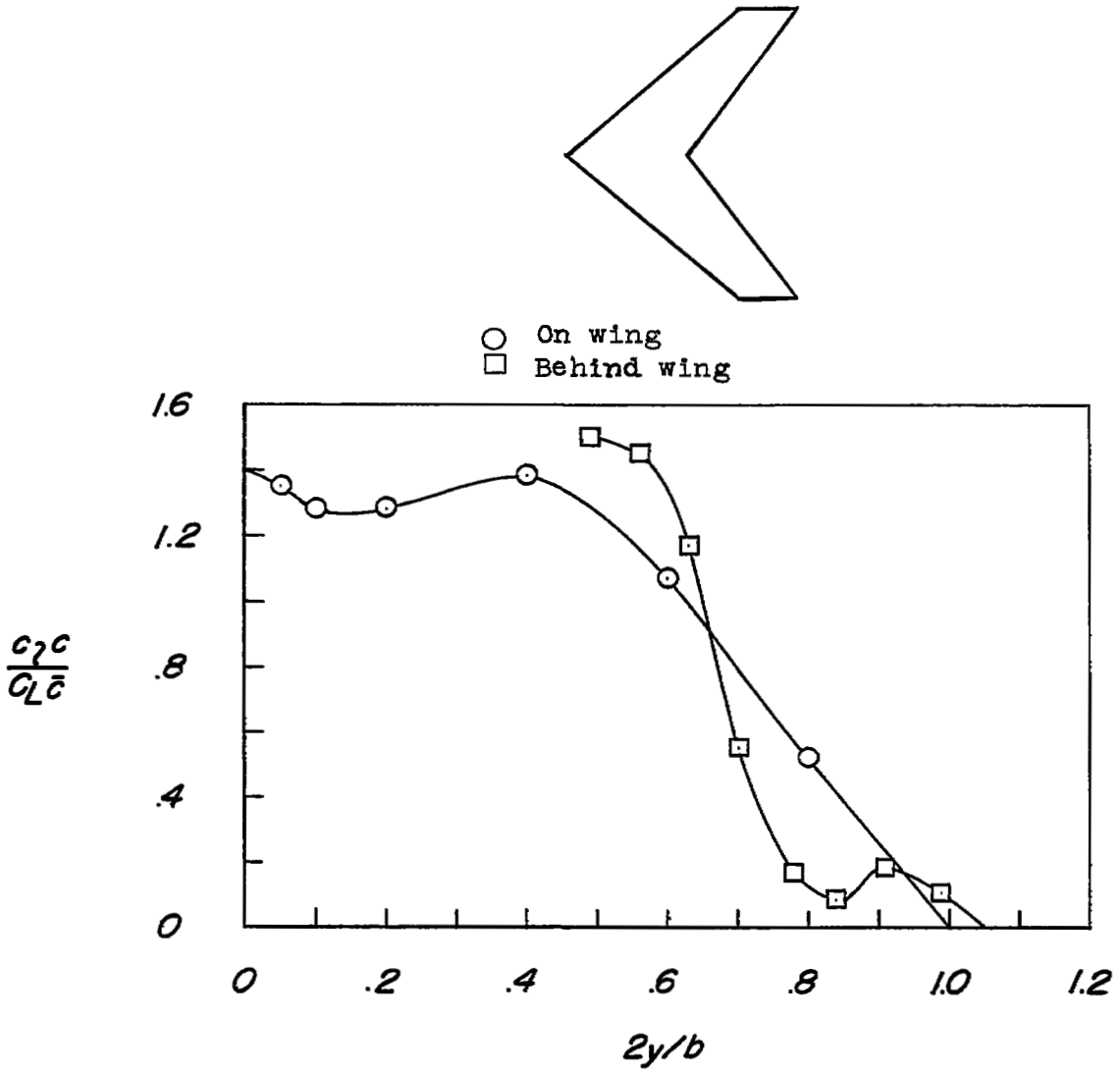

Figure 16.- Circulation distribution on and behind a 45-3.5-.50 wing having 10-percent-thick circular-arc airfoil sections. $\alpha = 14.0^{\circ}$; $C_L = 0.69$; $R = 4.3 \times 10^6$; reference 23.

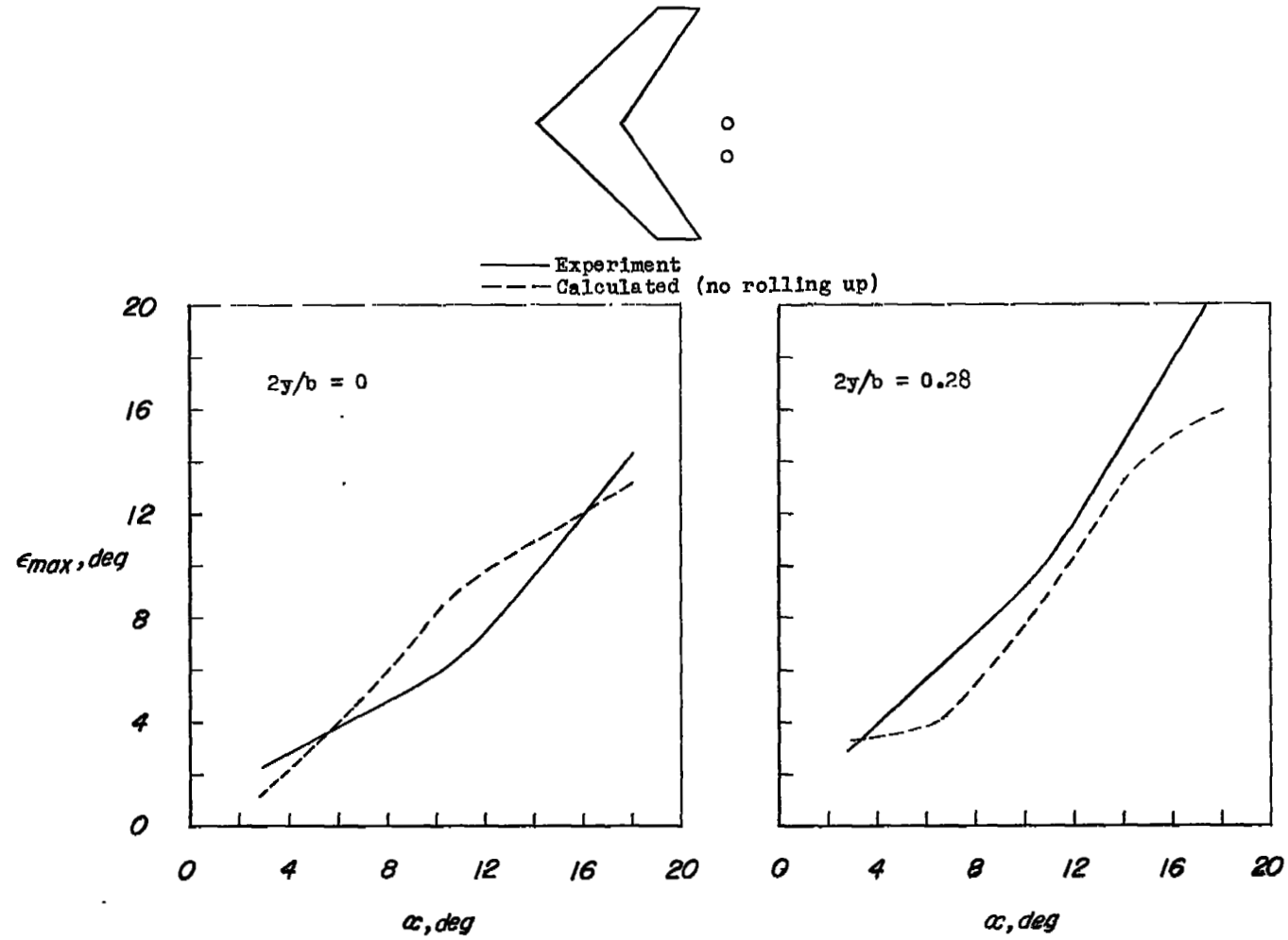

Figure 17.- Comparison of experimental and calculated downwash behind a 45-3.5-.50 wing having 10-percent-thick circular-arc airfoil sections. $2x_0/b = 1.13$; reference 23.

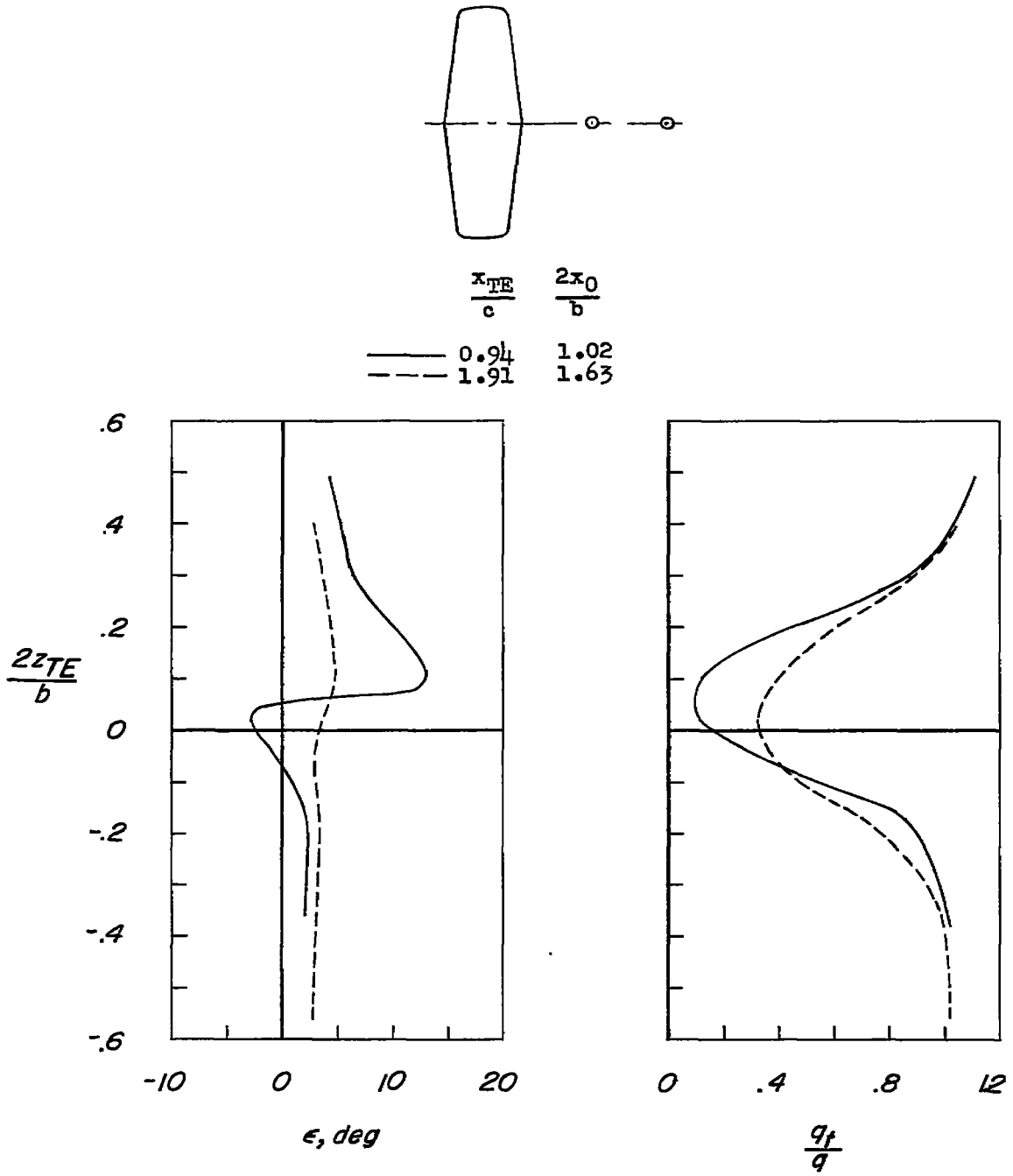

Figure 18.- Downwash and dynamic-pressure ratio at two longitudinal stations behind a stalled 3.4-4.0-.63 wing having 6-percent-thick hexagonal airfoil sections. $2y/b = 0$; $\alpha = 16.9°$; $R = 4.3 \times 10^6$; unpublished data from Langley 19-foot pressure tunnel.

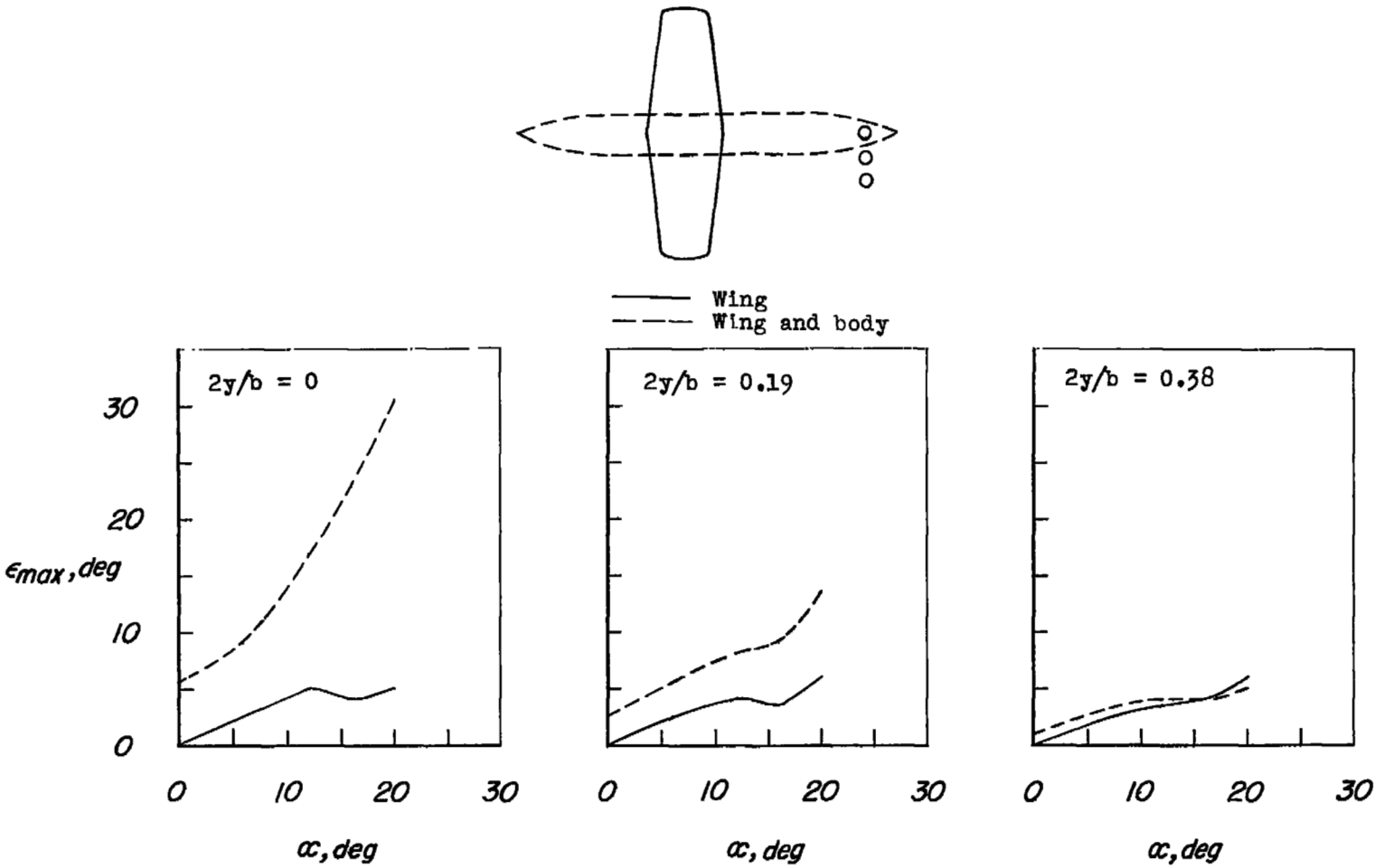

Figure 19.- Variation of maximum downwash with angle of attack for a 3.4-4.0-.63 wing and wing-body combination. Wing has 6-percent-thick hexagonal airfoil sections; $2x_0/b = 1.63$; $R = 4.3 \times 10^6$; unpublished data from Langley 19-foot pressure tunnel.

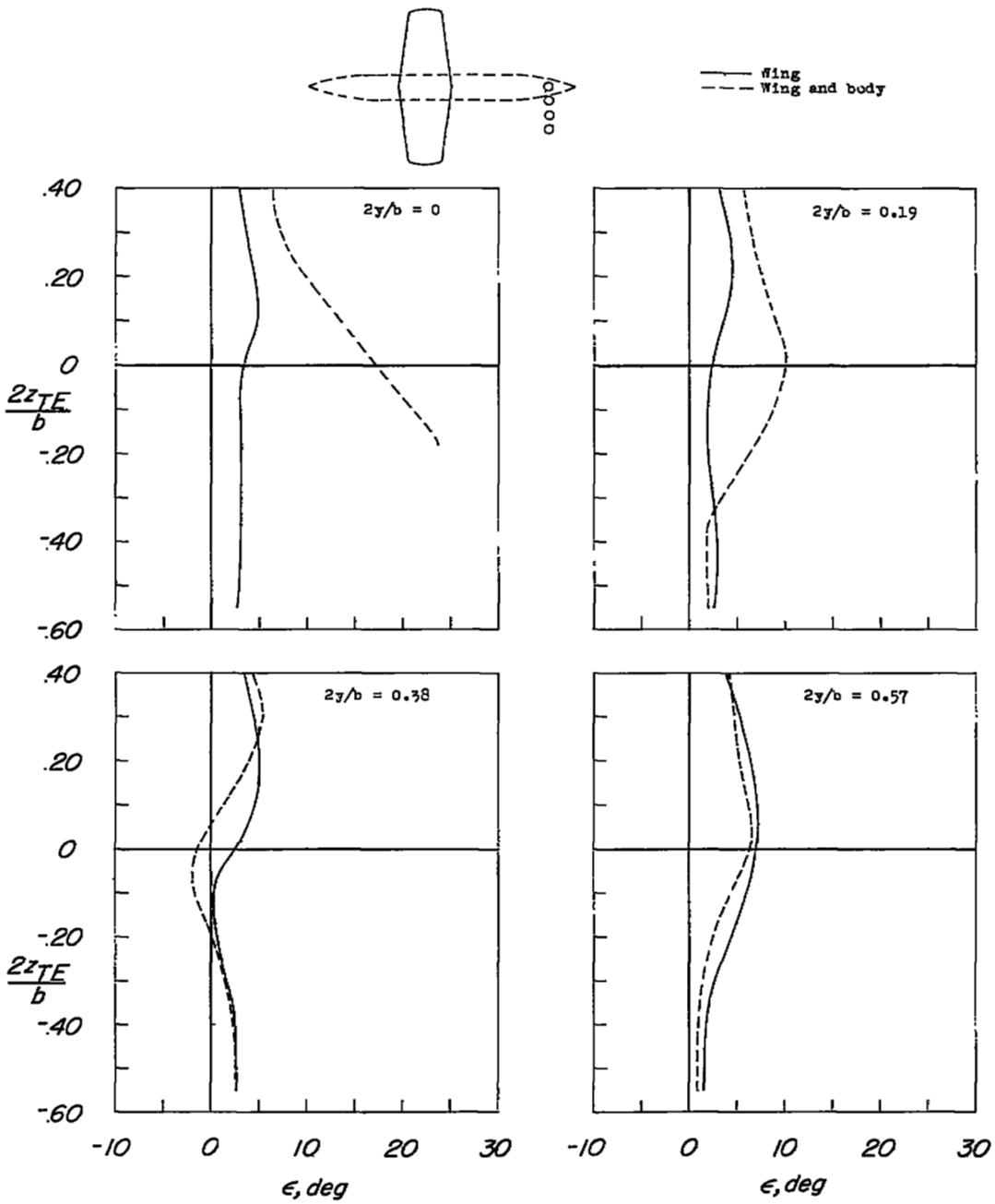

(a) Downwash.

Figure 20.- Downwash and dynamic-pressure ratio profiles behind a stalled 3.4-4.0-.63 wing and wing-body combination. Wing has 6-percent-thick hexagonal airfoil sections; $\alpha = 16.9^{\circ}$; $2x_0/b = 1.63$; $R = 4.3 \times 10^6$; unpublished data from Langley 19-foot pressure tunnel.

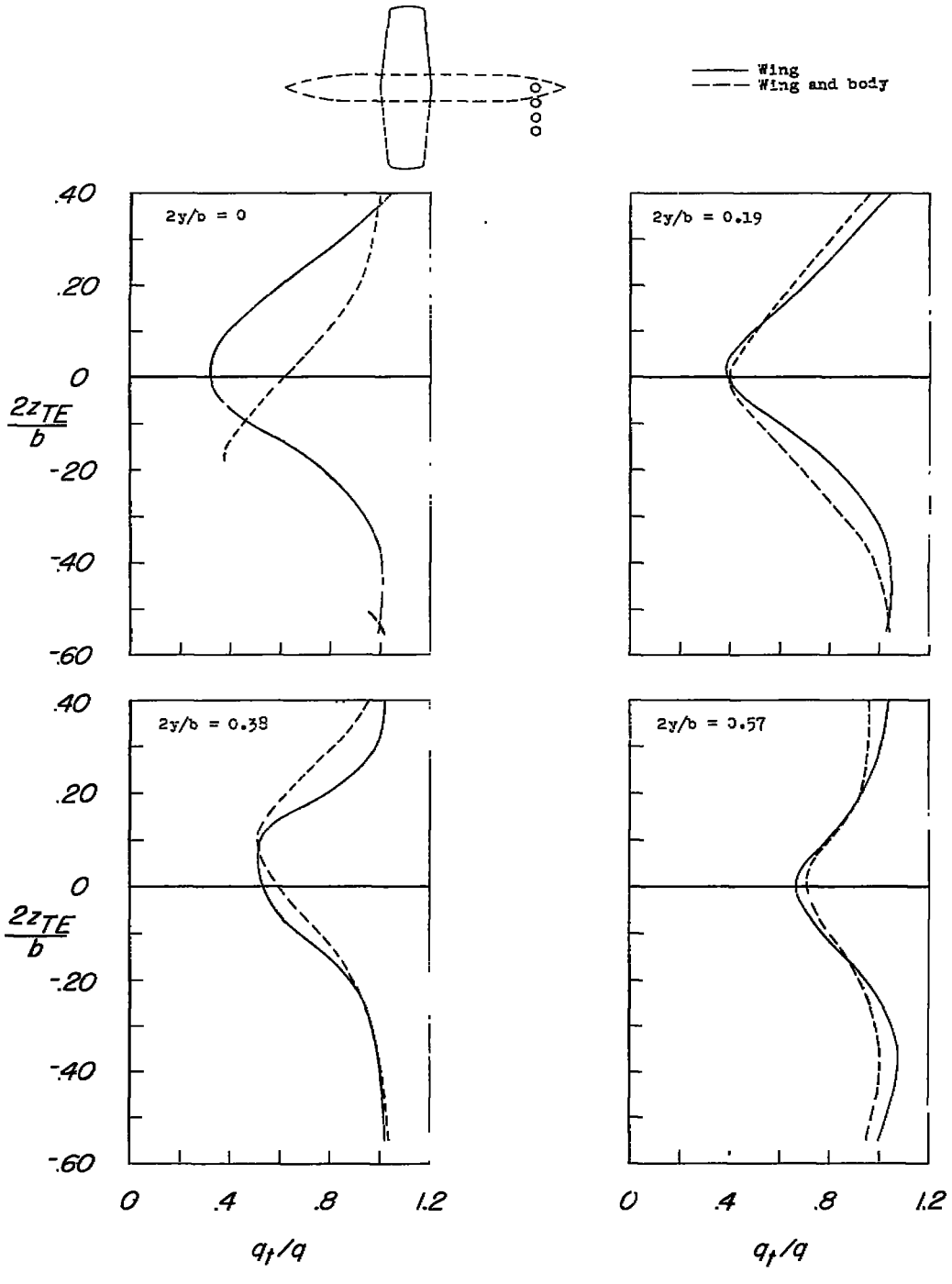

(b) Dynamic-pressure ratio.

Figure 20.- Concluded.

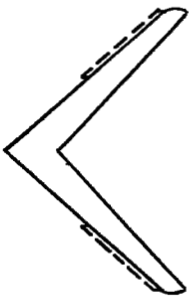

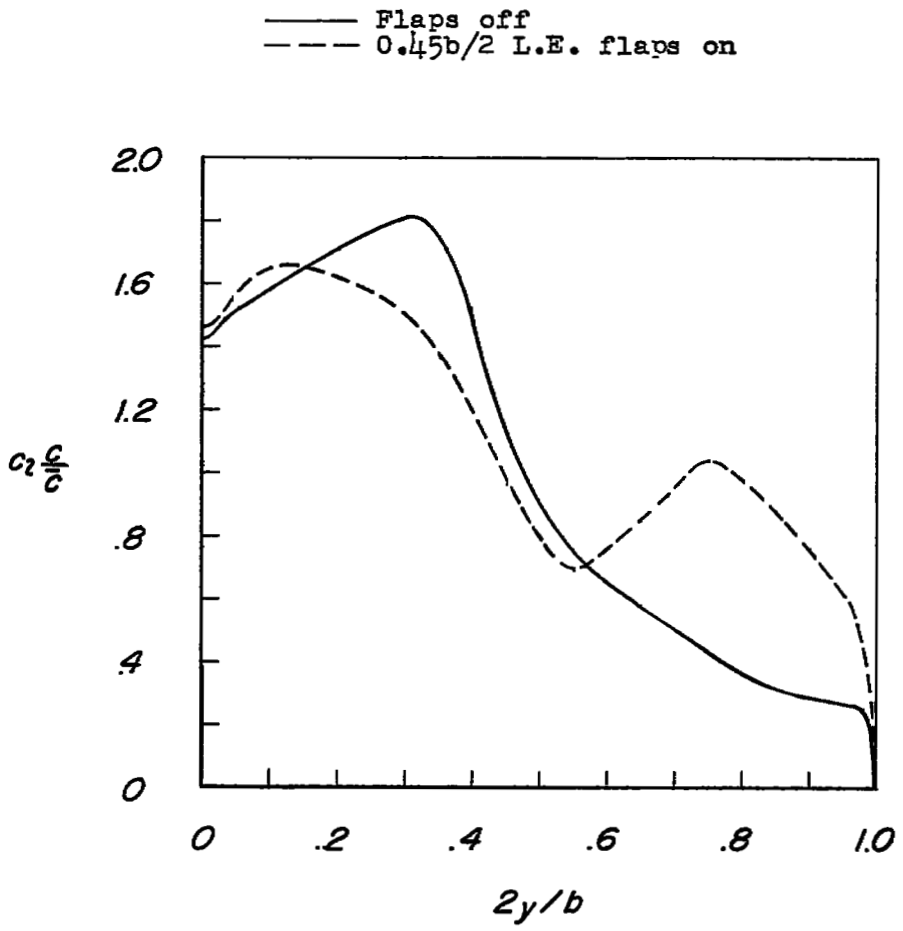

Figure 21.- Effect of leading-edge flaps on the experimental load distribution of a stalled 45-8.0-.45 wing. The wing had NACA 63_1A012 airfoil sections. $\alpha = 20.8^{\circ}$; $R = 4.0 \times 10^6$; reference 43.

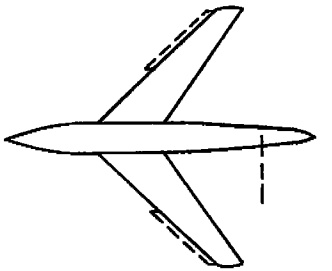

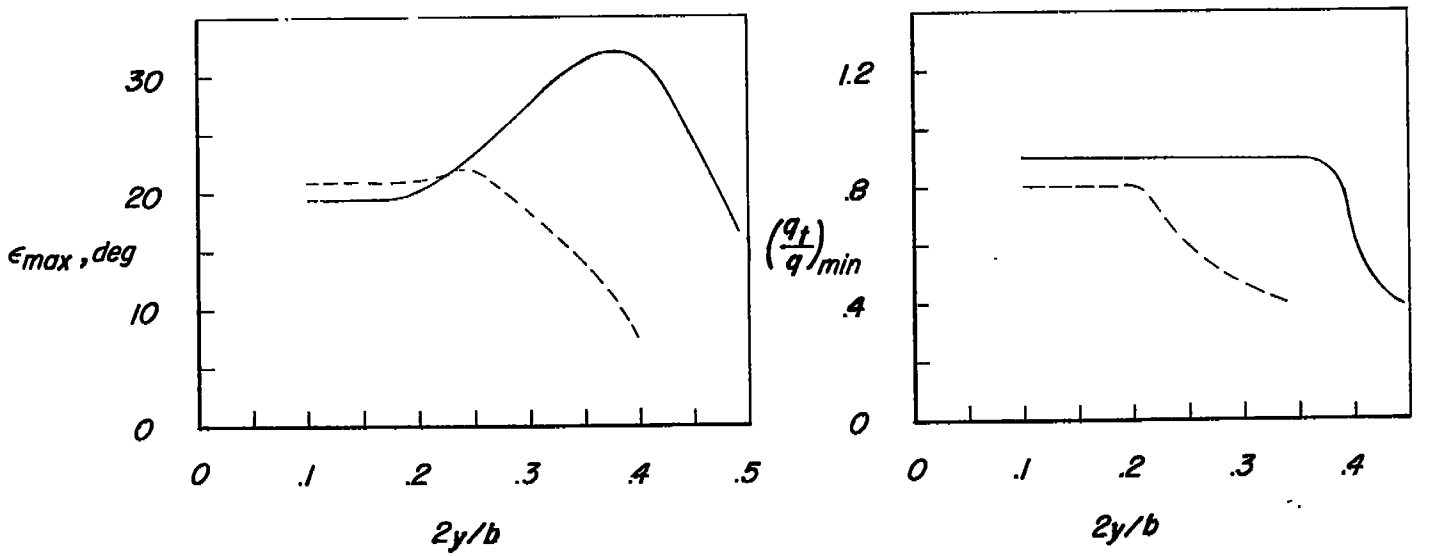

Figure 22.- Effect of leading-edge flaps on the spanwise variation of ϵ_{max} and $(q_t/q)_{min}$ behind a 45-5.1-.38 wing-body combination at $\alpha = 23.1^{\circ}$. The wing has NACA 64-210 airfoil sections normal to the 0.286 chord line. $2x_0/b = 0.88$; $R = 6.0 \times 10^6$; reference 44.

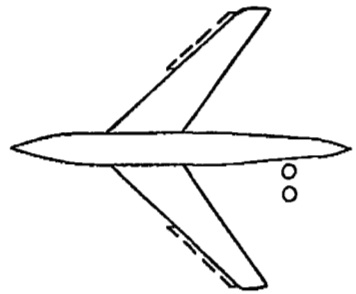

Flaps off
0.475b/2 L.E. flaps on

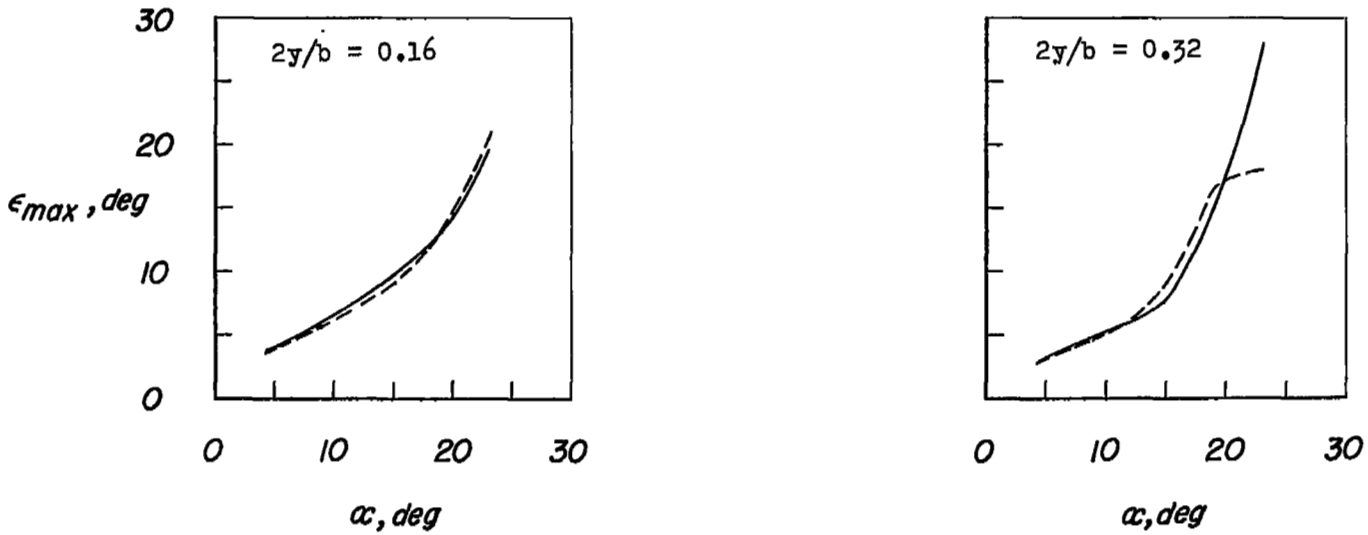

Figure 23.- Effect of leading-edge flaps on the variation of ϵ_{max} with angle of attack at two spanwise survey stations for a 45-5.1-.38 wing-body combination. The wing had NACA 64-210 airfoil sections normal to the 0.286 chord line. $2x_0/b = 0.88$; $R = 6.0 \times 10^6$; reference 44.

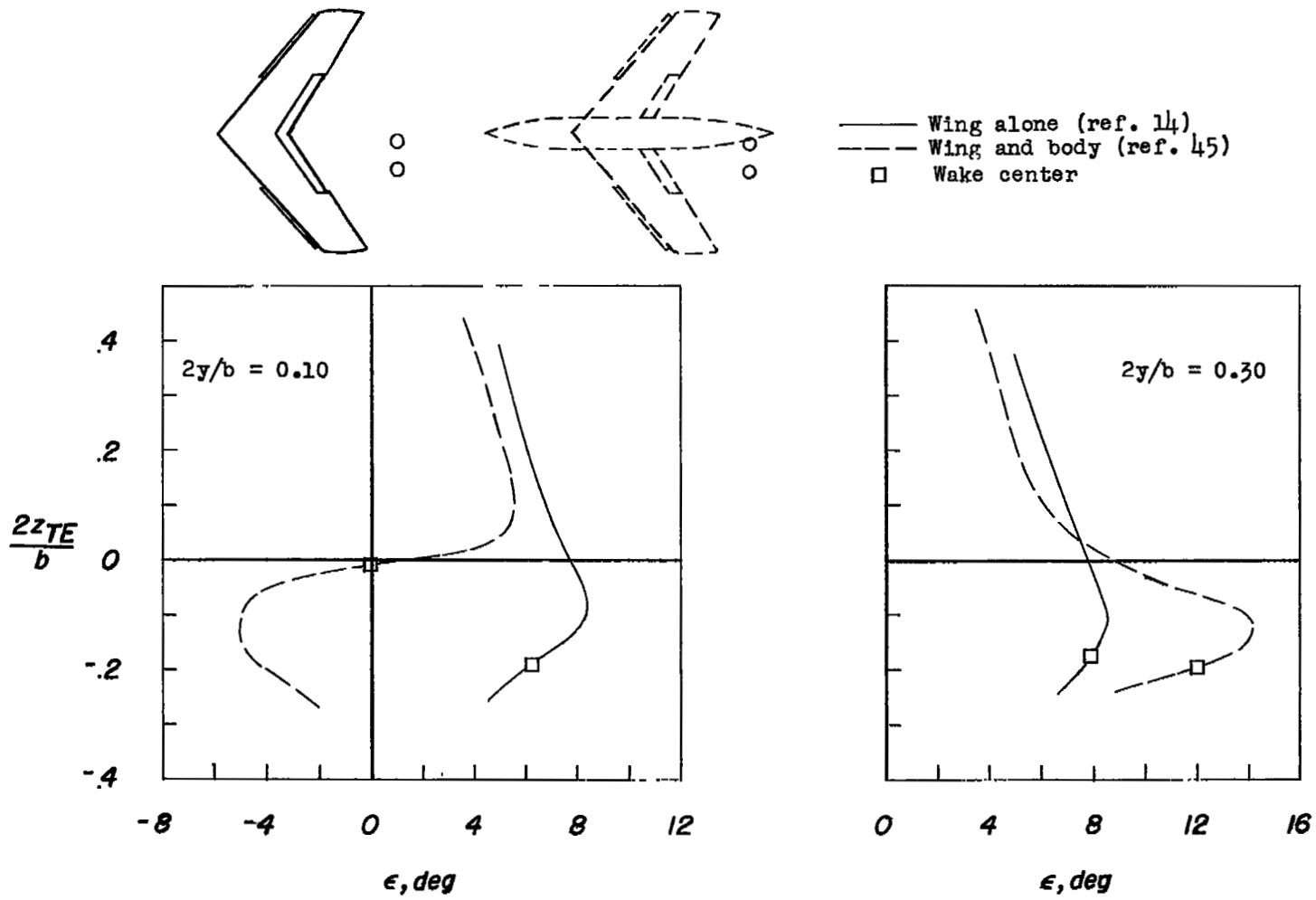

Figure 24.- Downwash at two spanwise stations behind a 40-4.0-.63 wing with and without a body. 0.5b/2 trailing-edge split flaps deflected 60°; 0.575b/2 leading-edge flaps; $2x_0/b = 1.00$; $\alpha = 3.6°$; $R = 6.8 \times 10^6$.

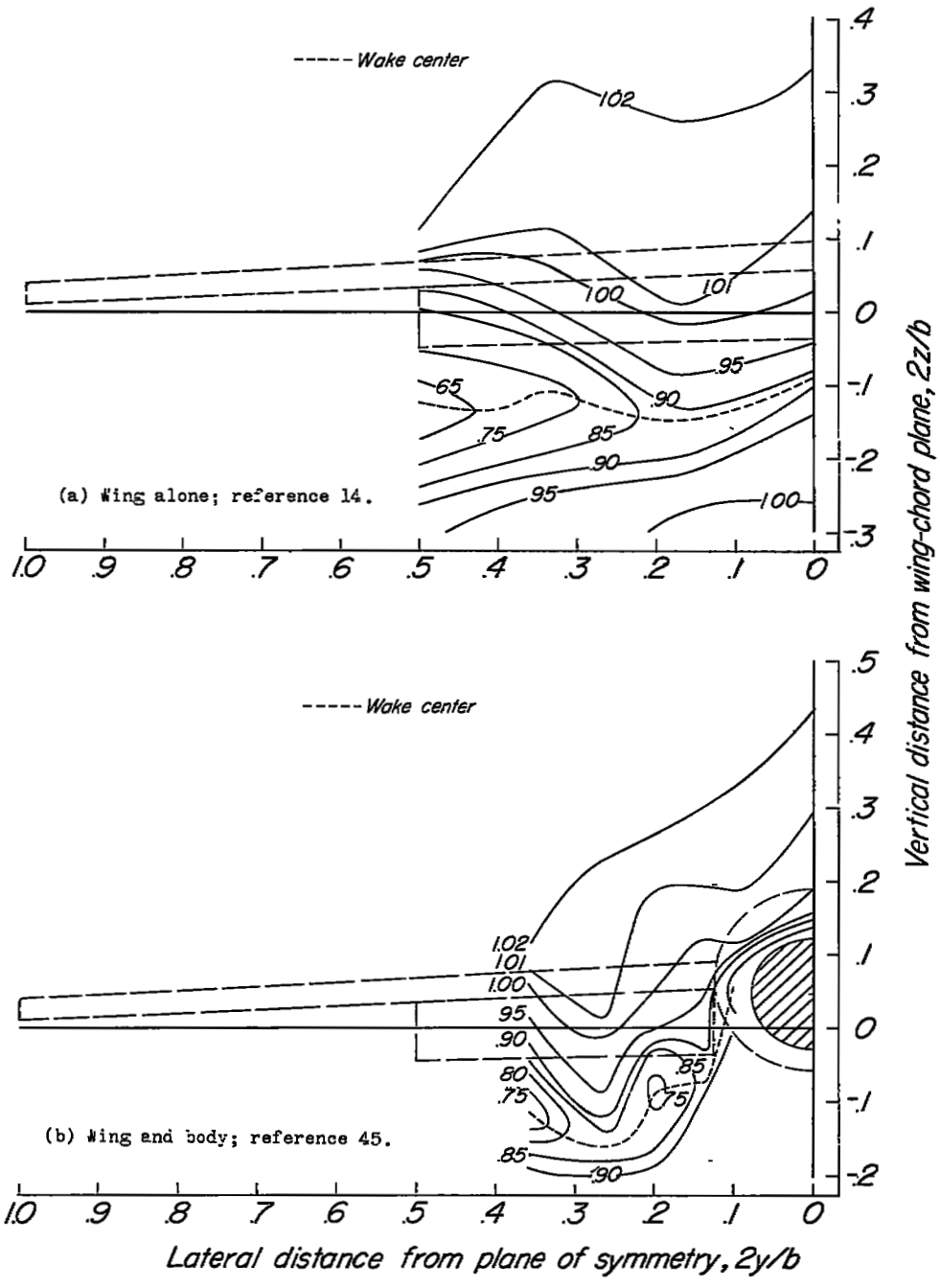

Figure 25.- Contours of dynamic-pressure ratio (q_t/q) behind a flapped 40-4.0-.63 wing with and without a body. 0.5b/2 trailing-edge split flaps deflected 60°; 0.575b/2 leading-edge flaps; $2x_0/b = 1.02$; $\alpha = 3.6°$; $R = 6.8 \times 10^6$.

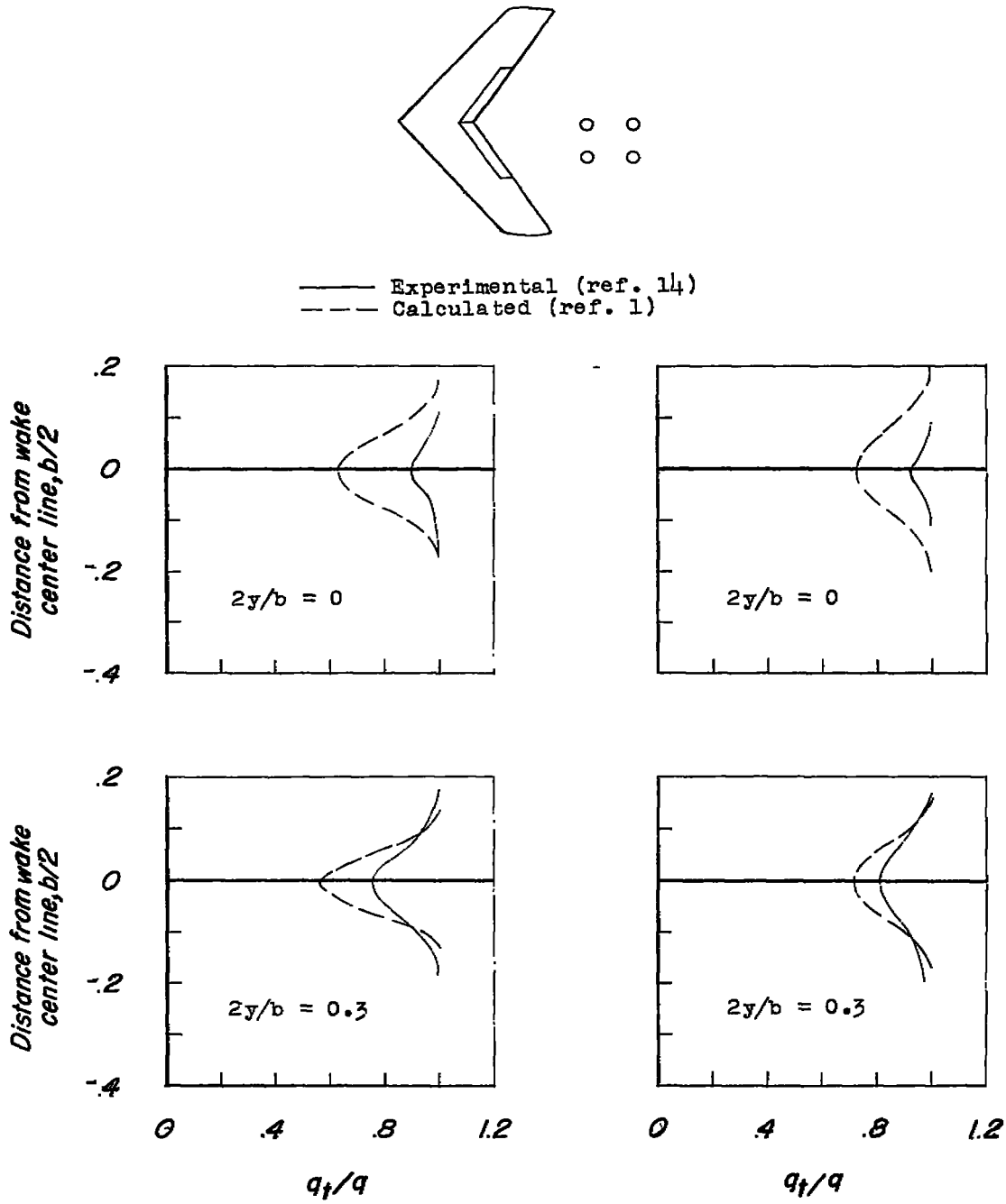

(a) $2x_0/b = 1.02$. (b) $2x_0/b = 1.42$.

Figure 26.- Comparison between experimental and calculated dynamic-pressure characteristics behind a 40-4.0-.63 wing with 0.5b/2 split flaps deflected 60°. $\alpha = 3.6°$; $R = 6.8 \times 10^6$.

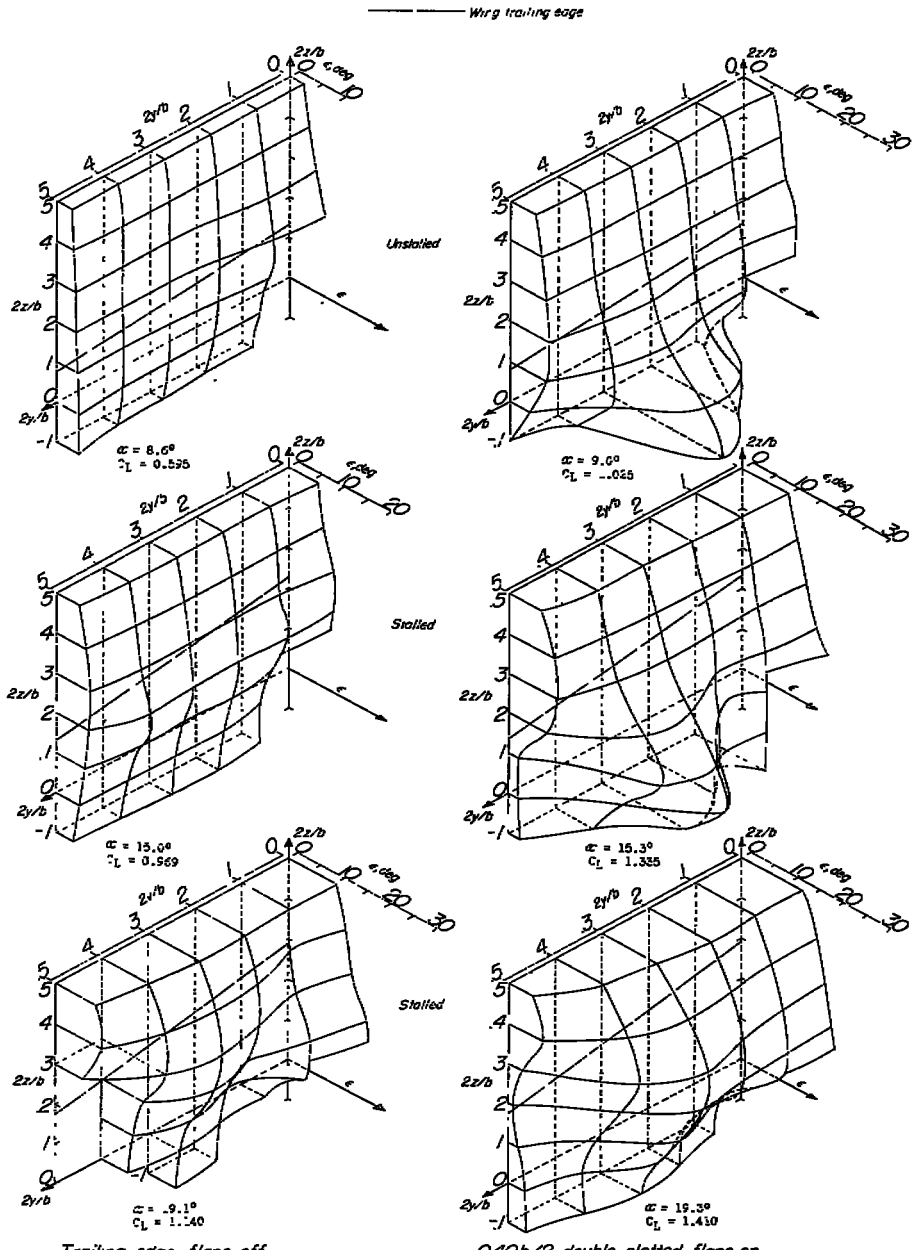

(a) Downwash.

Figure 27.- Effects of trailing-edge flaps deflected 50° on the downwash and wake characteristics of a 45.1-5.1-.38 wing-body combination with 0.475b/2 leading-edge flaps. The wing had NACA 64-210 airfoil sections normal to 0.286 wing chord line. $2x_0/b$ = 0.88; R = 6.0 × 10^6; reference 44.

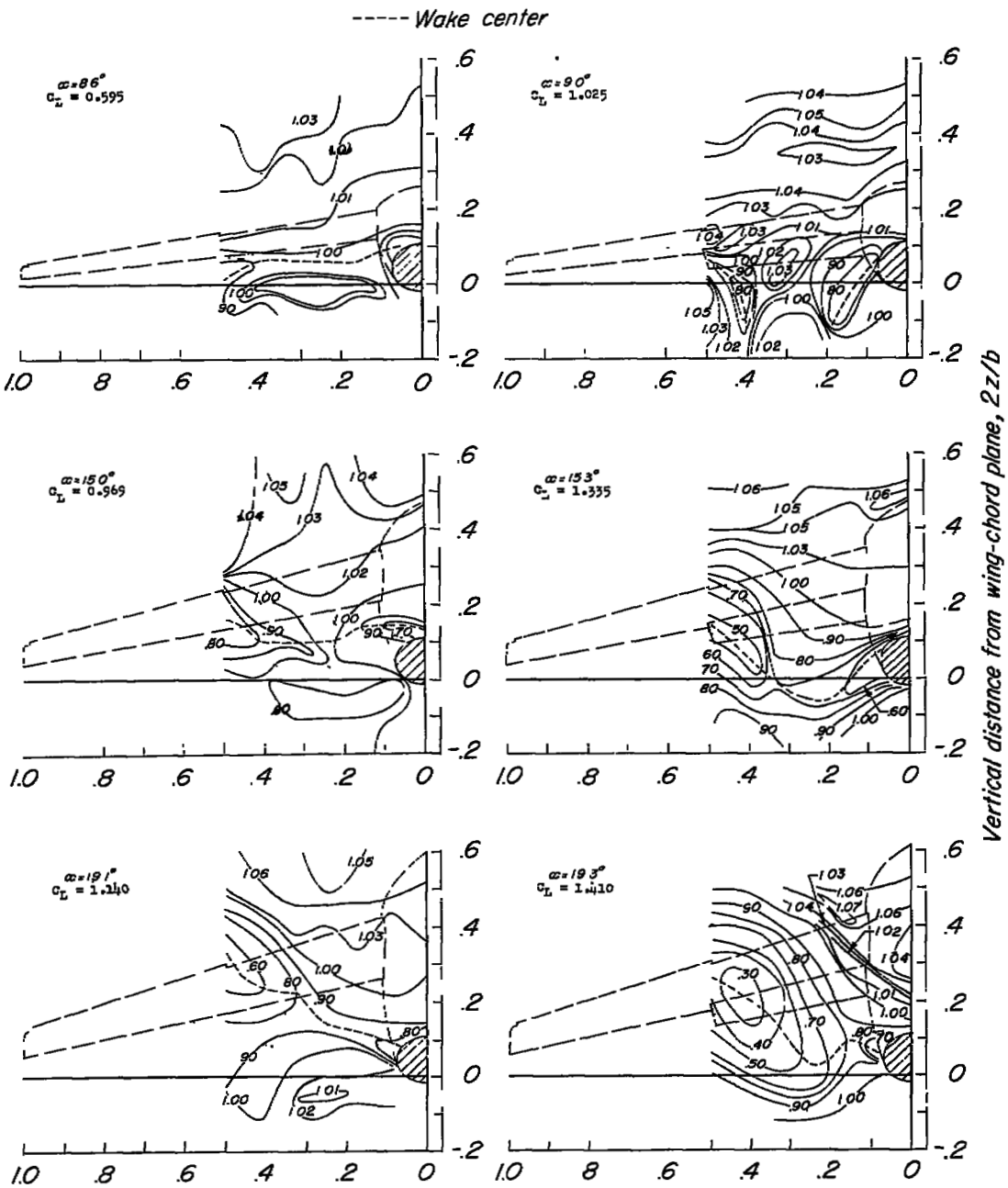

(b) Dynamic-pressure ratio.

Figure 27.- Concluded.

Tail plan form	Afterbody shape	Distance from body center line	Distance from wing chord plane	Reference
○ 0-4.4-.46	Closed	0	0	58
□ 0-4.0-.33	Blunt	0	0	70
◇ 0-4.0-.33	Blunt	0	-0.10b/2	70
△ 45-3.0-.54	Closed	0	0	78
▽ 45-3.0-.46	Blunt	-0.086b/2	-0.12b/2	Unpublished

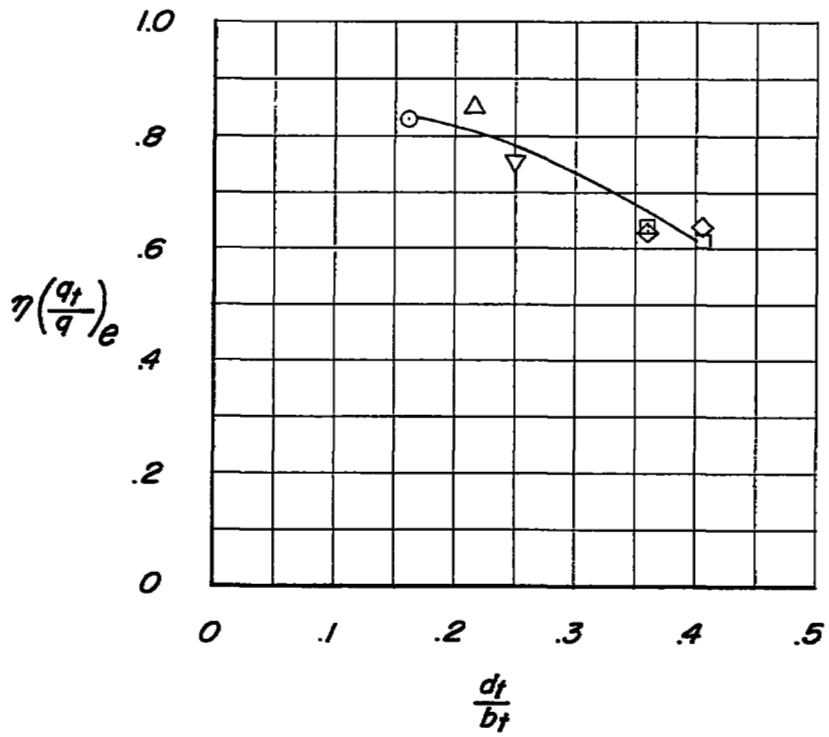

Figure 28.- Summary of values of $\eta\left(\frac{q_t}{q}\right)_e$ obtained with tail surfaces mounted on bodies.

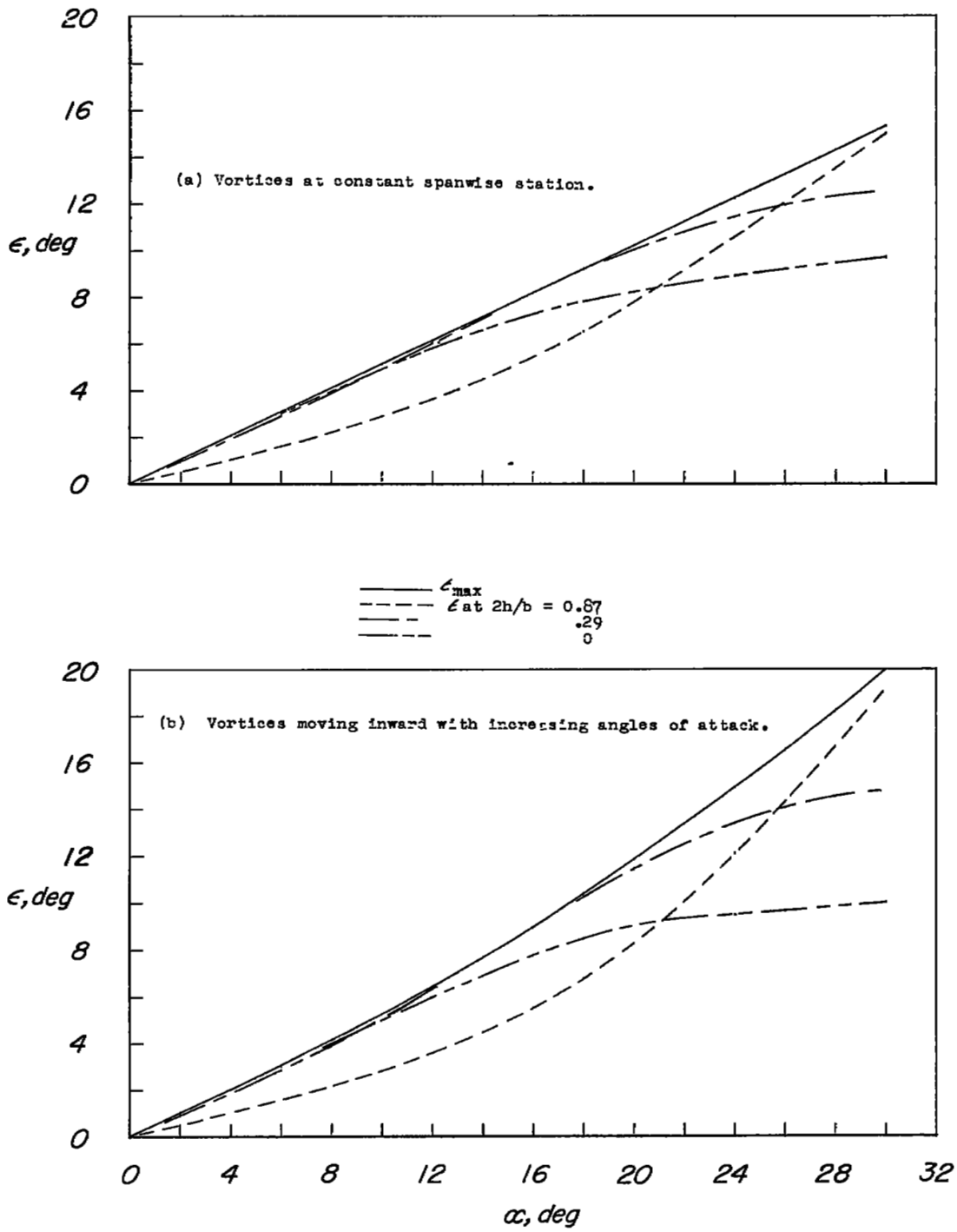

Figure 29.- Calculated downwash at tail due to a pair of vortices.

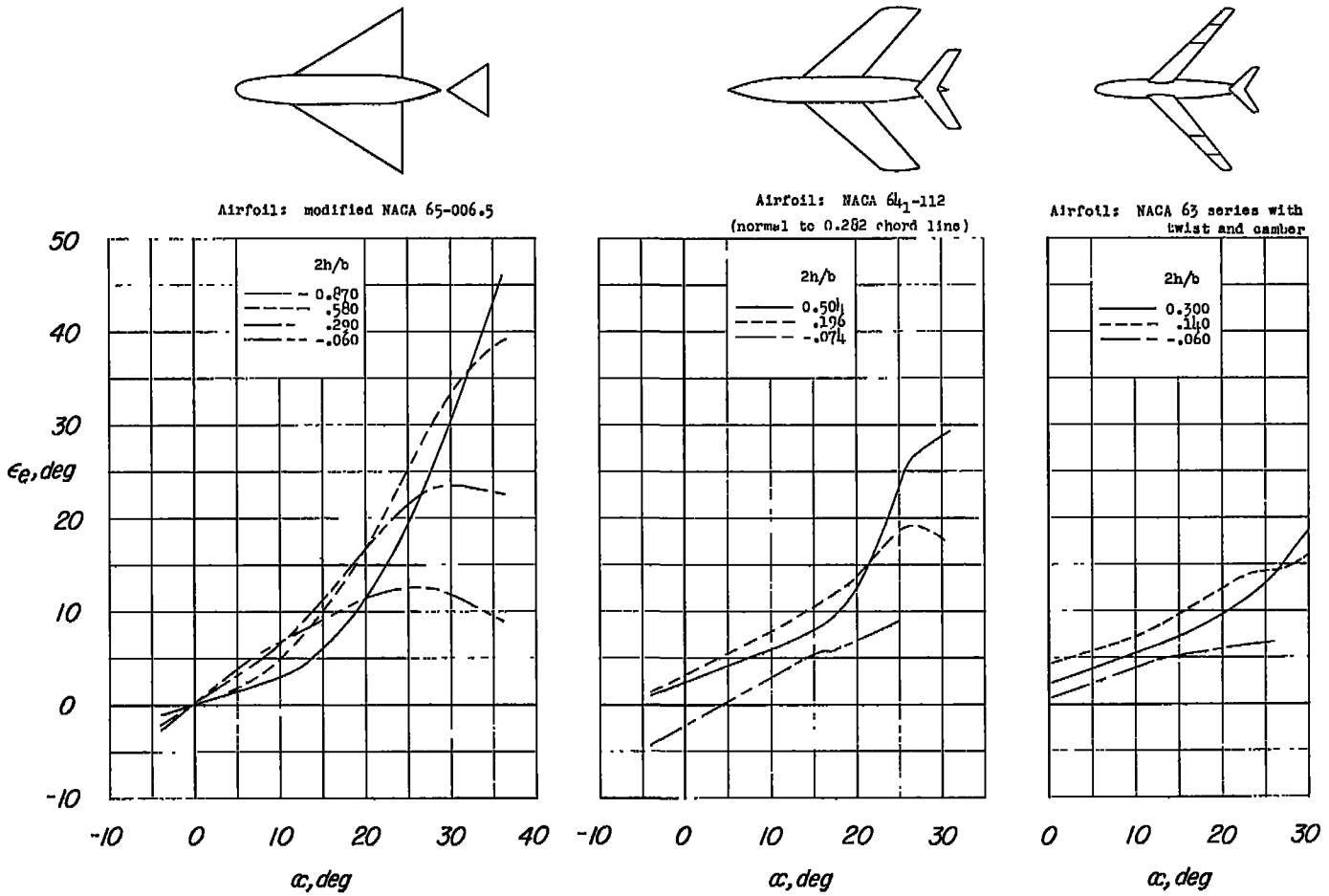

(a) 52.4-2.3-0; $2l/b = 1.73$; $R = 2.06 \times 10^6$; α for $C_{L_{max}} = 31^\circ$; reference 50.

(b) 50-2.9-.63; $2l/b = 1.23$; $R = 6.0 \times 10^6$; α for $C_{L_{max}} = 26.6^\circ$; reference 27.

(c) 45-8.0-.45; $2l/b = 0.77$; $R = 4.0 \times 10^6$; α for $C_{L_{max}} = 27^\circ$; reference 40.

Figure 30.- Effective downwash for three sweptback wing-body combinations.

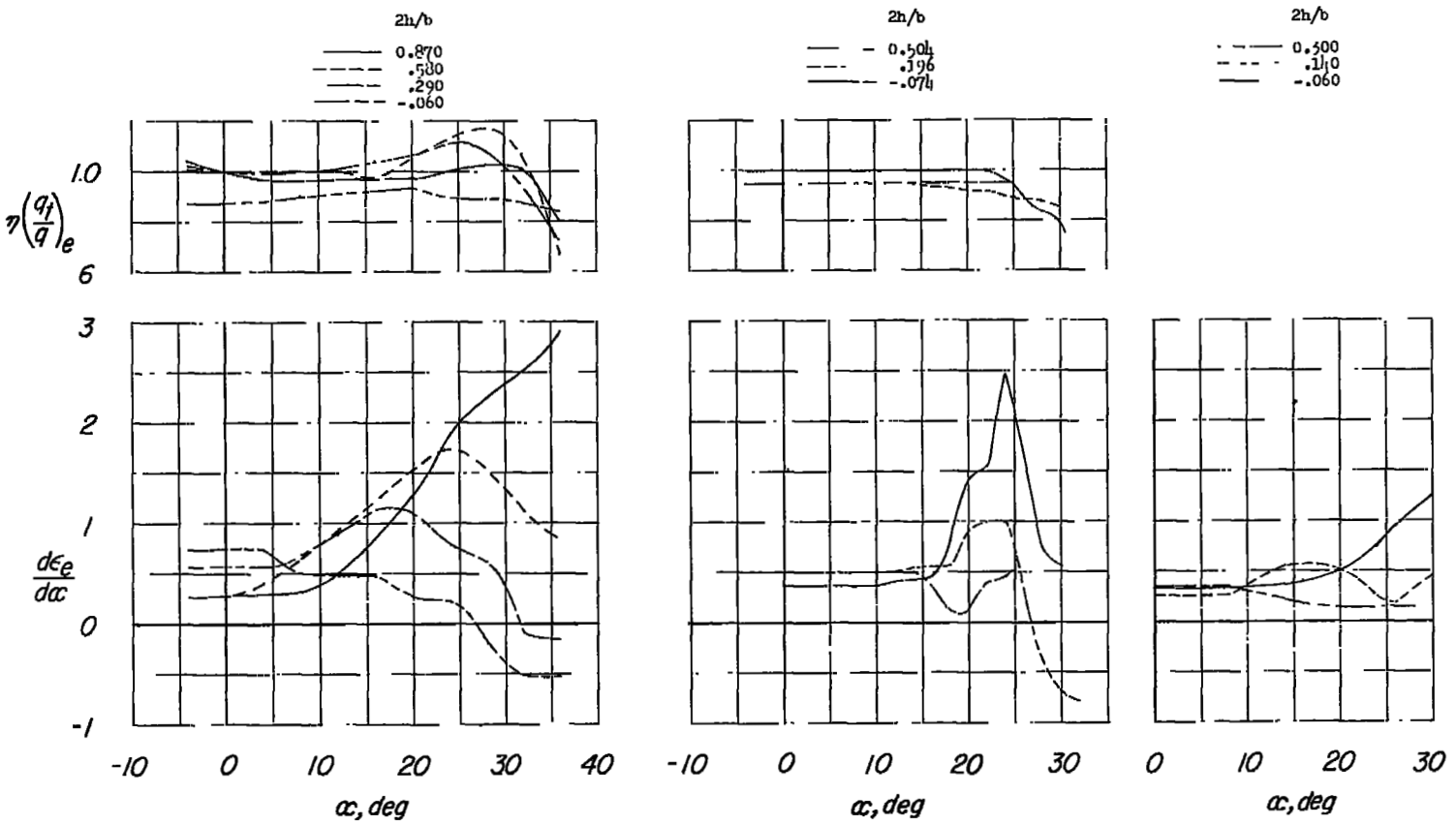

(a) 52.4-2.3-0; $2l/b = 1.73$; $R = 2.06 \times 10^6$; α for $C_{L_{max}} = 31^\circ$; reference 50.

(b) 50-2.9-.63; $2l/b = 1.23$; $R = 6.0 \times 10^6$; α for $C_{L_{max}} = 26.6^\circ$; reference 27.

(c) 45-8.0-.45; $2l/b = 0.77$; $R = 4.0 \times 10^6$; α for $C_{L_{max}} = 27^\circ$; reference 40.

Figure 31.- Values of $\eta\left(\frac{q_t}{q}\right)_e$ and $d\epsilon_e/d\alpha$ for three sweptback wing-body combinations.

Wing	Airfoil section	Ref.
○ 40-4.0-.63	NACA 64_1-112 (normal to 0.273 chord line)	60
□ 40-3.5-.50	Circular arc	23
◇ 45-5.1-.38	NACA 64-210 (normal to 0.286 chord line)	44
△ 50-2.9-.63	NACA 64_1-112 (normal to 0.282 chord line)	27
▽ 50-2.8-.63	Circular arc (normal to line of max. thickness)	13
▷ 52.4-2.3-0	NACA $65_{(006)}$-006.5	50

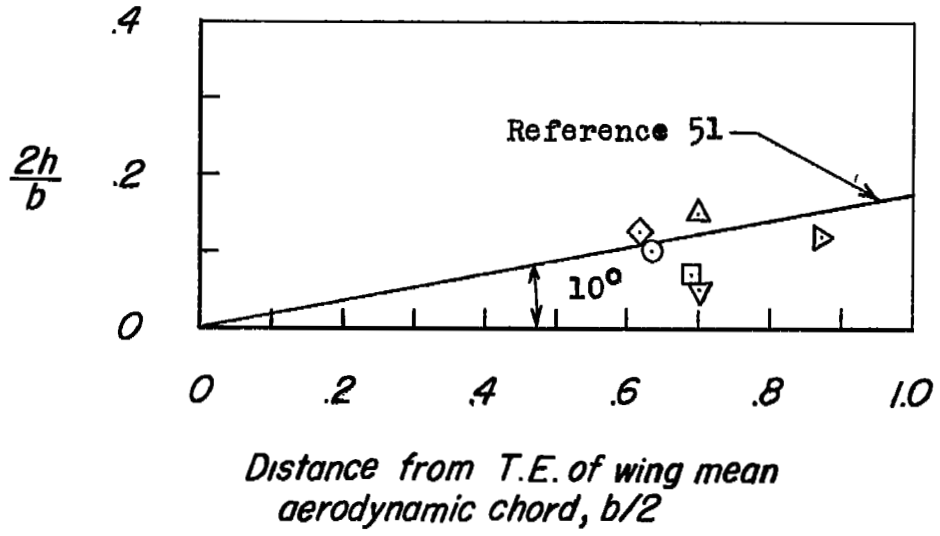

Figure 32.- Maximum tail heights for no destabilizing change in $d\epsilon/d\alpha$.

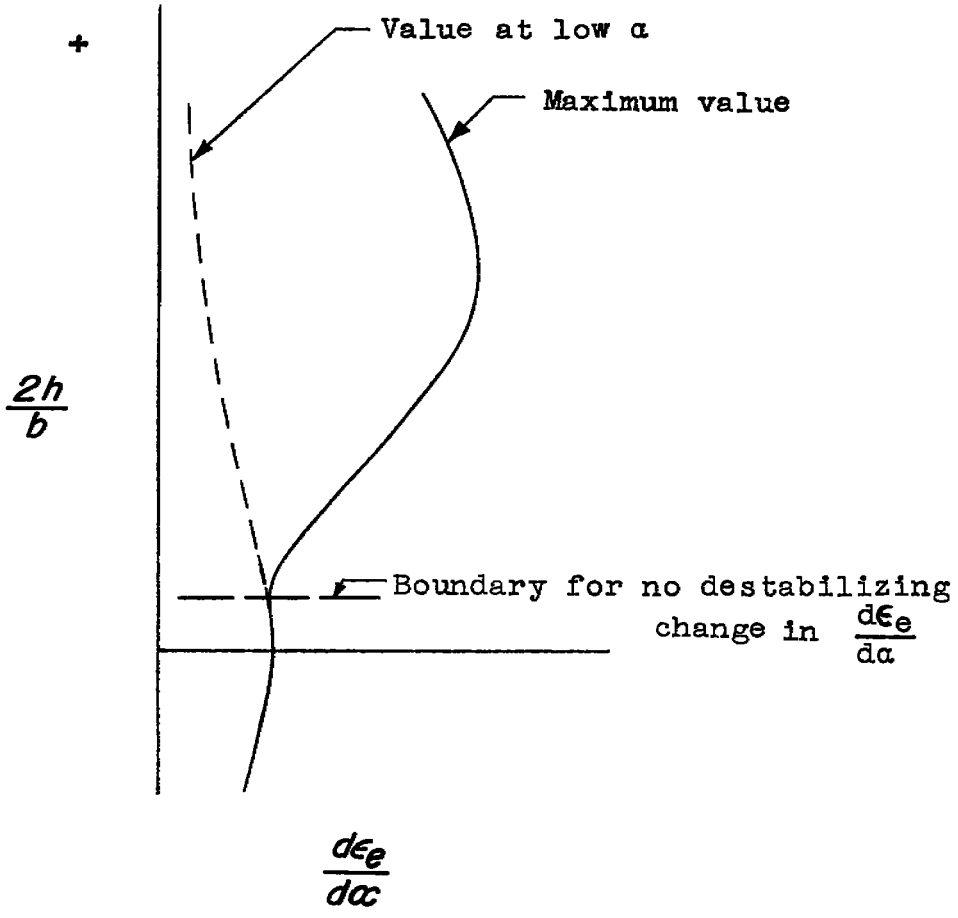

Figure 33.- Illustration showing the variation of $d\epsilon_e/d\alpha$ with tail location.

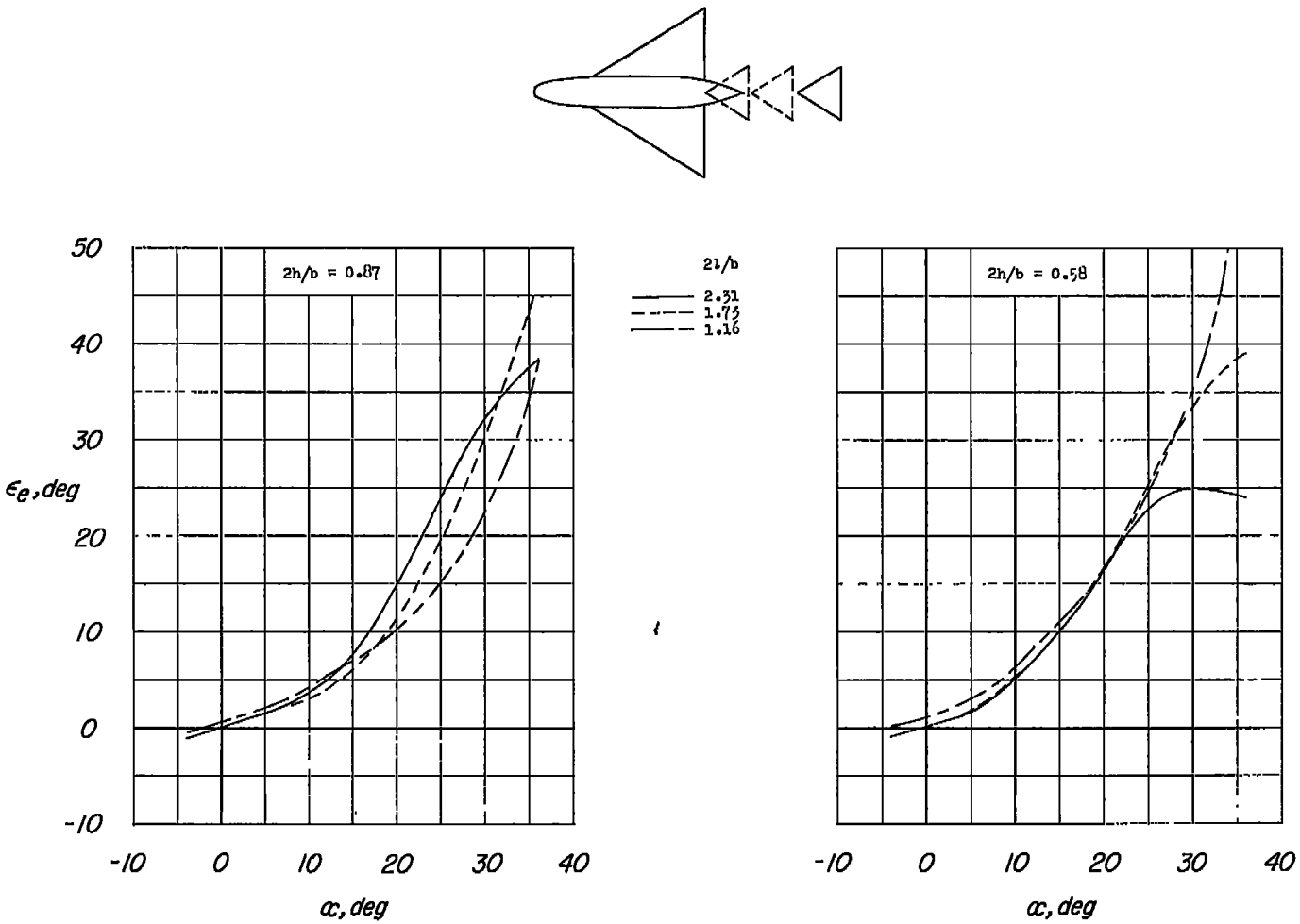

Figure 34.- Effect of tail length on the effective downwash characteristics of a 52.4-2.3-0 wing-body combination with the tail at various heights. The wing had modified NACA $65_{(06)}$-006.5 airfoil sections. R = 2.06×10^6; reference 50.

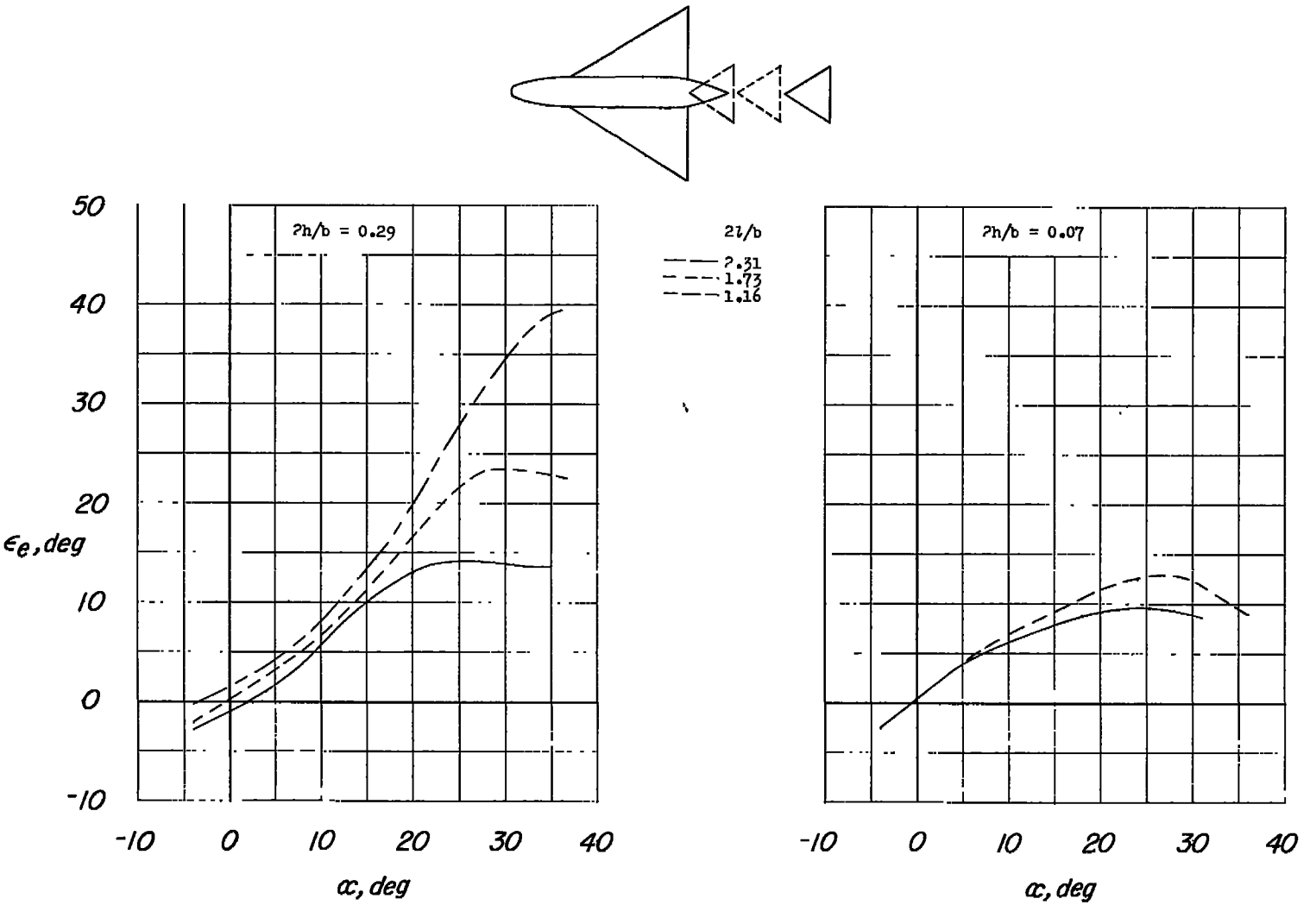

Figure 34.- Concluded.

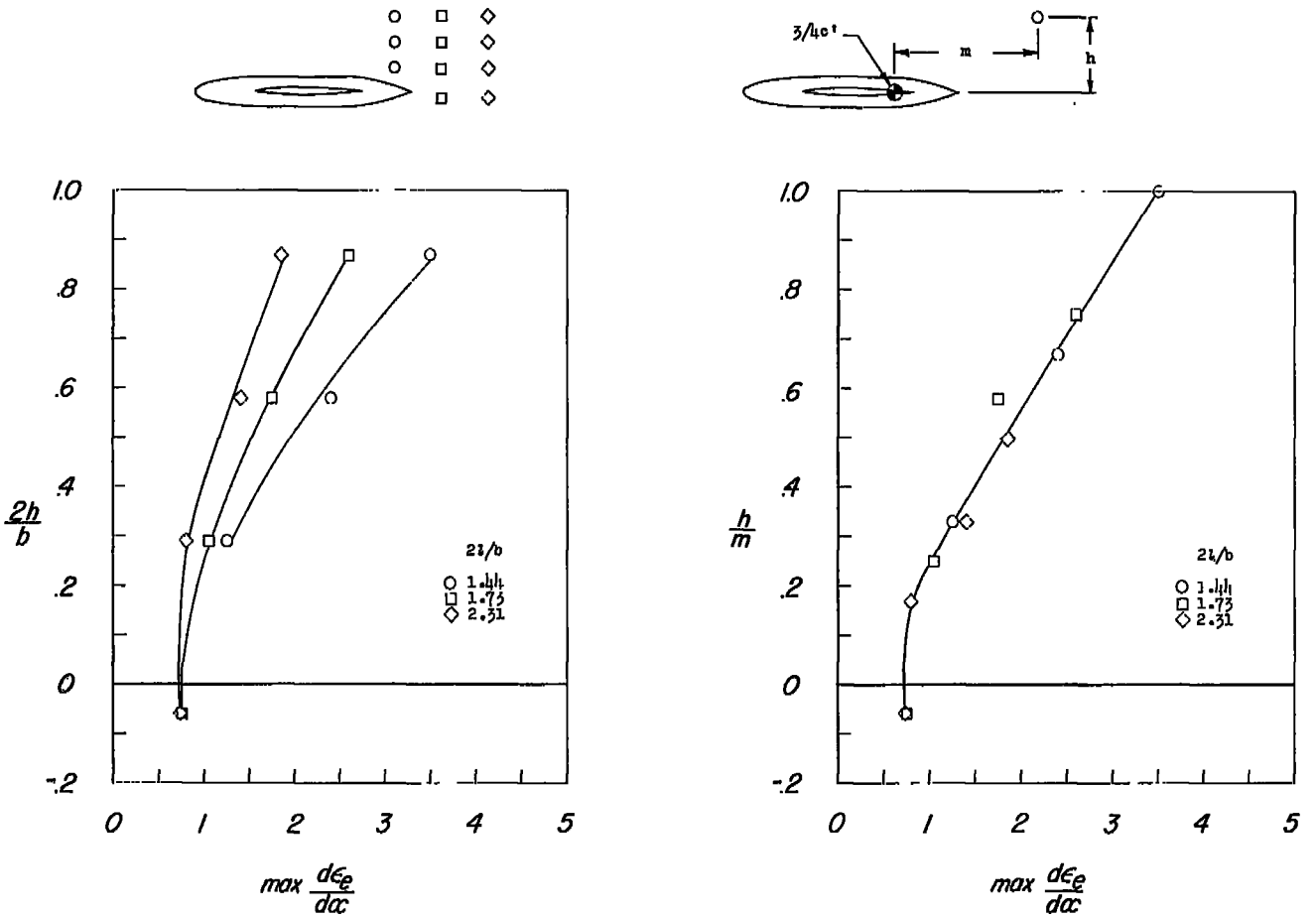

(a) 2h/b against maximum $d\epsilon_e/d\alpha$. (b) h/m against maximum $d\epsilon_e/d\alpha$.

Figure 35.- Effect of tail length on the maximum value of $d\epsilon_e/d\alpha$ for a 52.8-2.3-0 wing-body combination. The wing has modified NACA $65_{(06)}$-006.5 airfoil sections. $R = 2.06 \times 10^6$; reference 50.

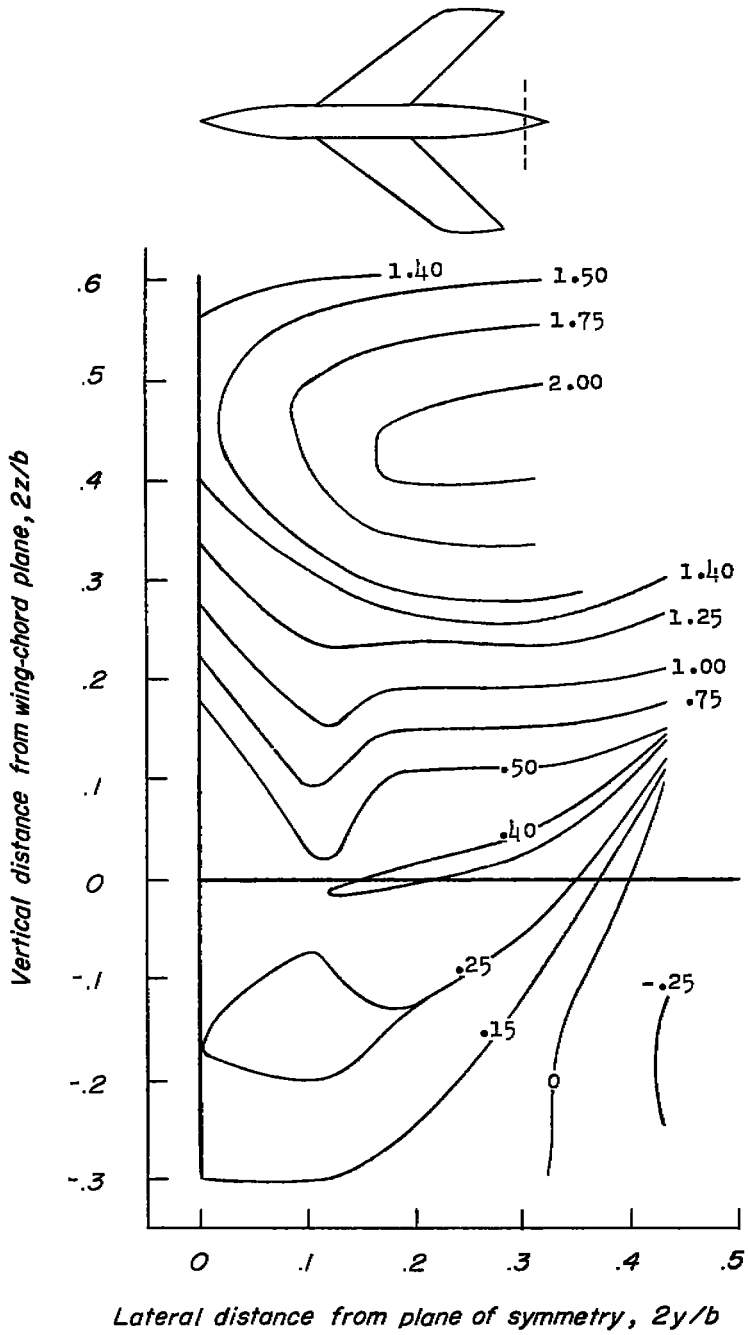

Figure 36.- Contours of $\partial\epsilon/\partial\alpha$ behind a stalled 50-2.9-.63 wing-body combination incorporating NACA 64_1-112 airfoil sections normal to 0.282 chord line. $\alpha = 21^\circ$; $2x_0/b = 1.17$; $R = 6.0 \times 10^6$; α for $C_{L_{max}} = 26.6^\circ$; reference 27.

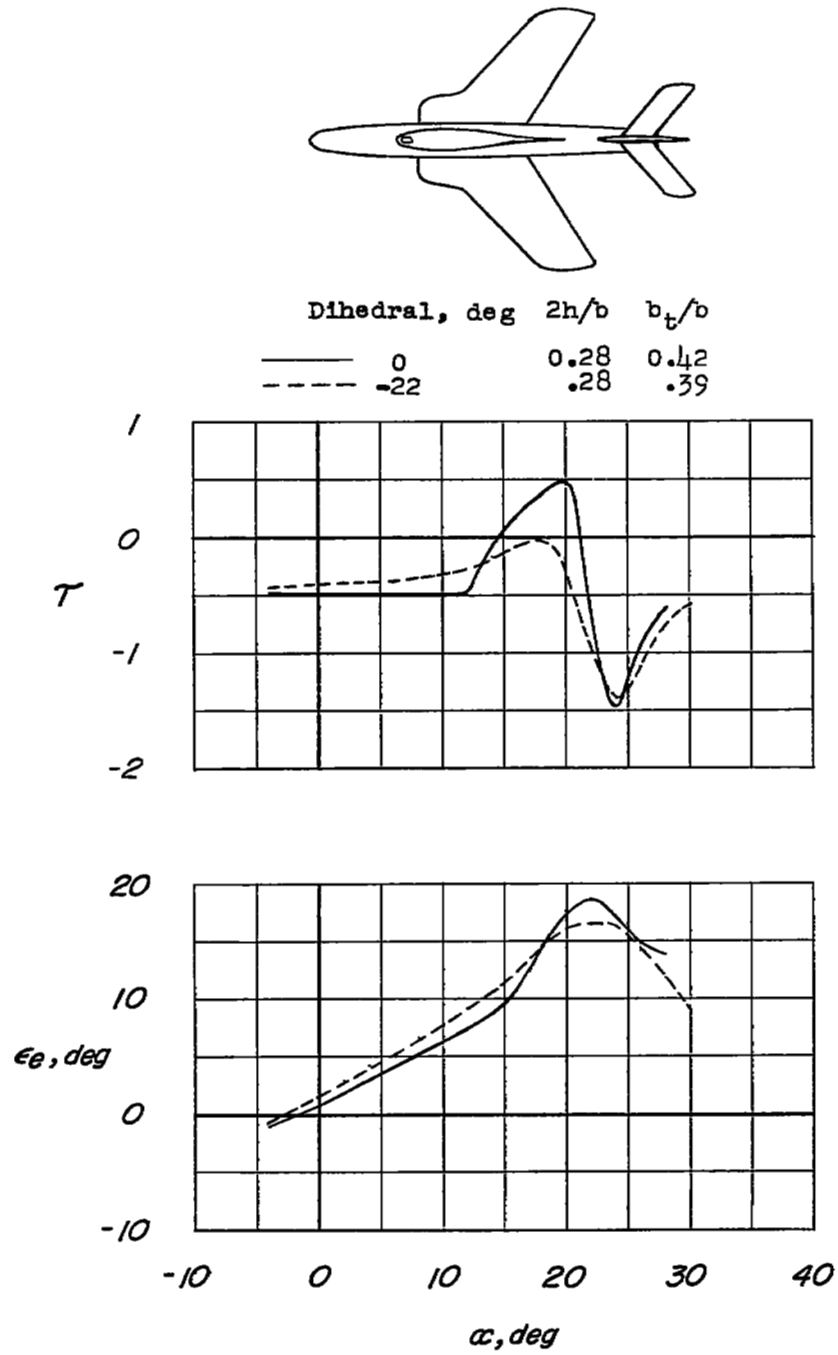

Figure 37.- Effect of tail dihedral on the stability parameter τ and the effective downwash of a 40-3.5-.58 wing-body combination. The wing had NACA 64A010 airfoil sections normal to the 0.25 chord line. $2l/b = 1.20$; α for $C_{L_{max}} = 20°$; $R = 9.0 \times 10^6$; unpublished data from Langley 19-foot pressure tunnel.

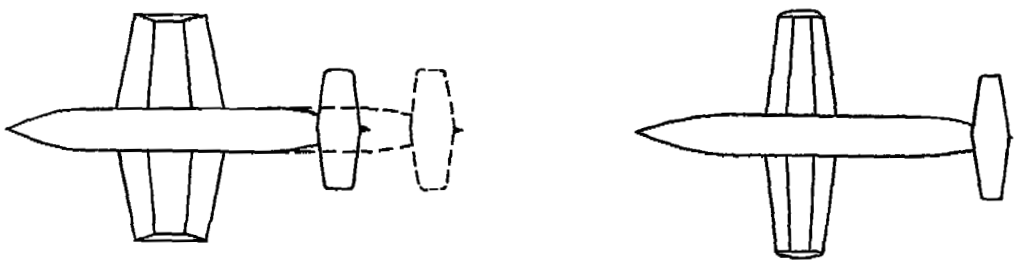

Wing	2ℓ/b	b_t/d	α for $C_{L_{max}}$	Ref.
—— 5.3-2.5-.63	1.63	2.51	14.6°	52
- - - - 5.3-2.5-.63	2.44	2.51	14.6°	52
—— 3.4-4.0-.63	1.66	3.17	14.6°	49

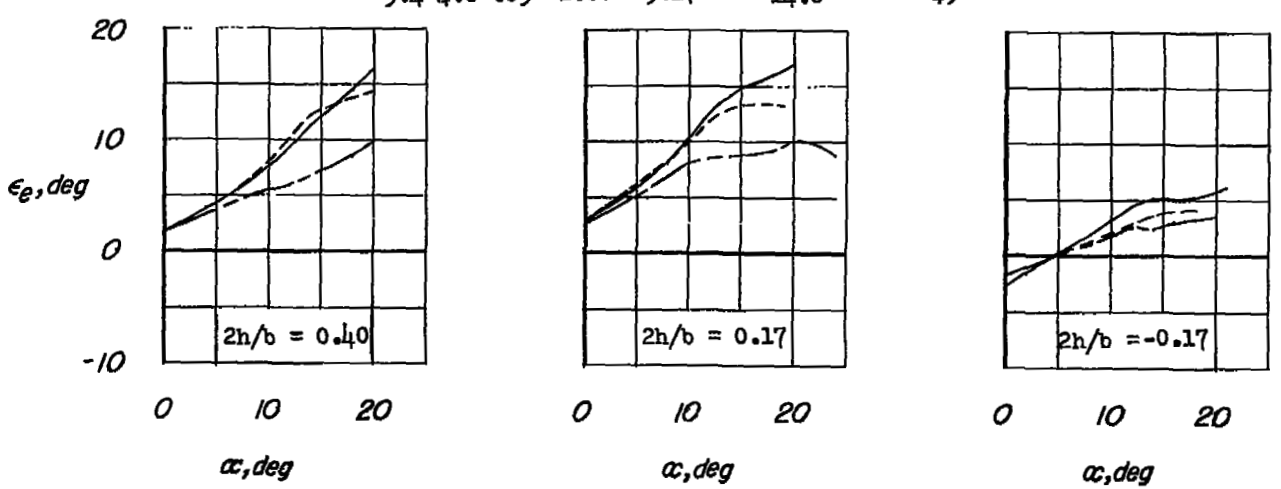

(a) ϵ_e against α.

Figure 38.- Effective downwash ϵ_e, $\eta\left(\frac{q_t}{q}\right)_e$, and stability parameter τ for several unswept wing-body combinations. Wings have 6-percent-thick hexagonal airfoil sections. $R \approx 6.2 \times 10^6$ to 7.6×10^6.

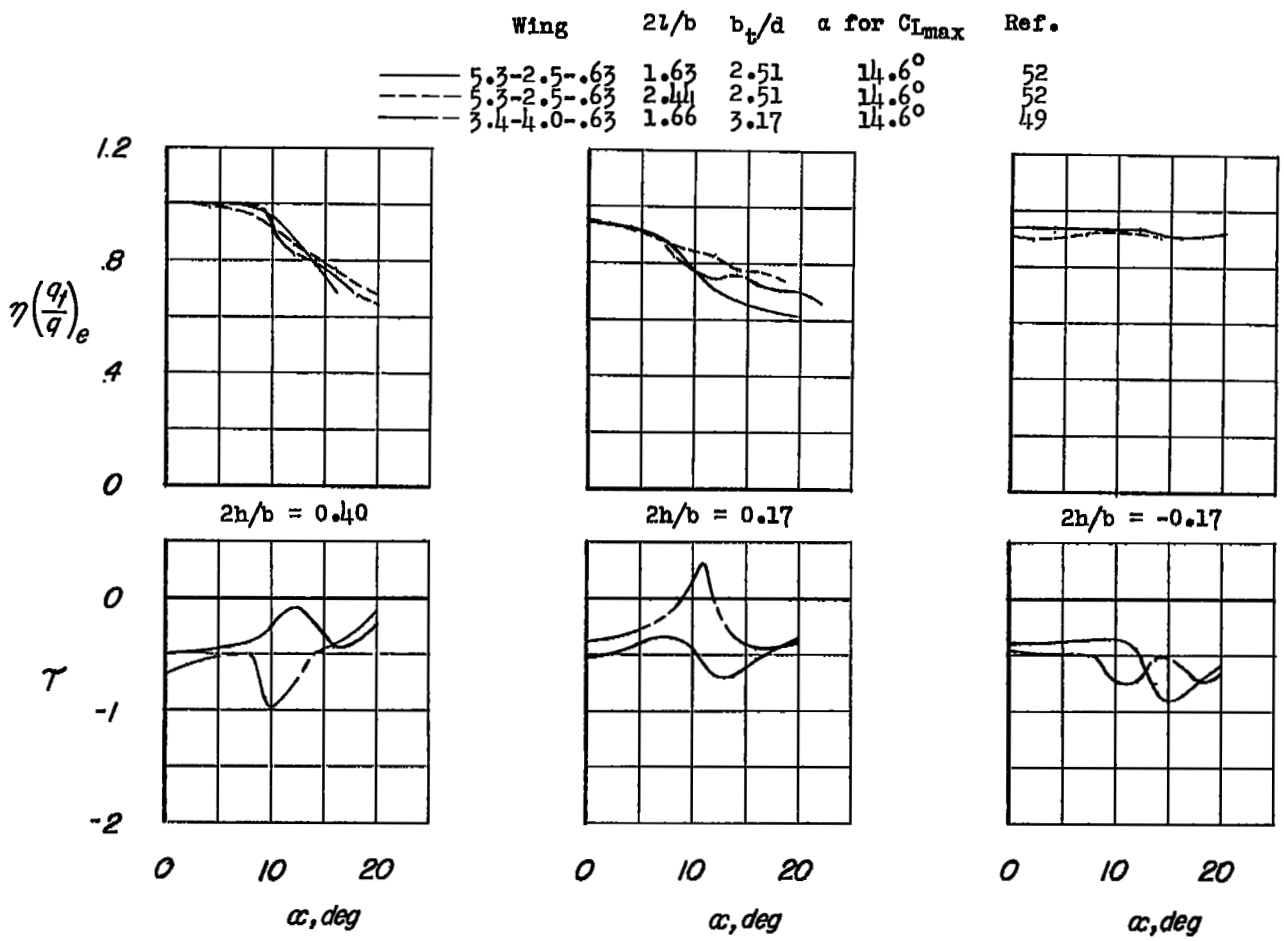

(b) $\eta\left(\frac{q_t}{q}\right)_e$ and τ against α.

Figure 38.- Concluded.

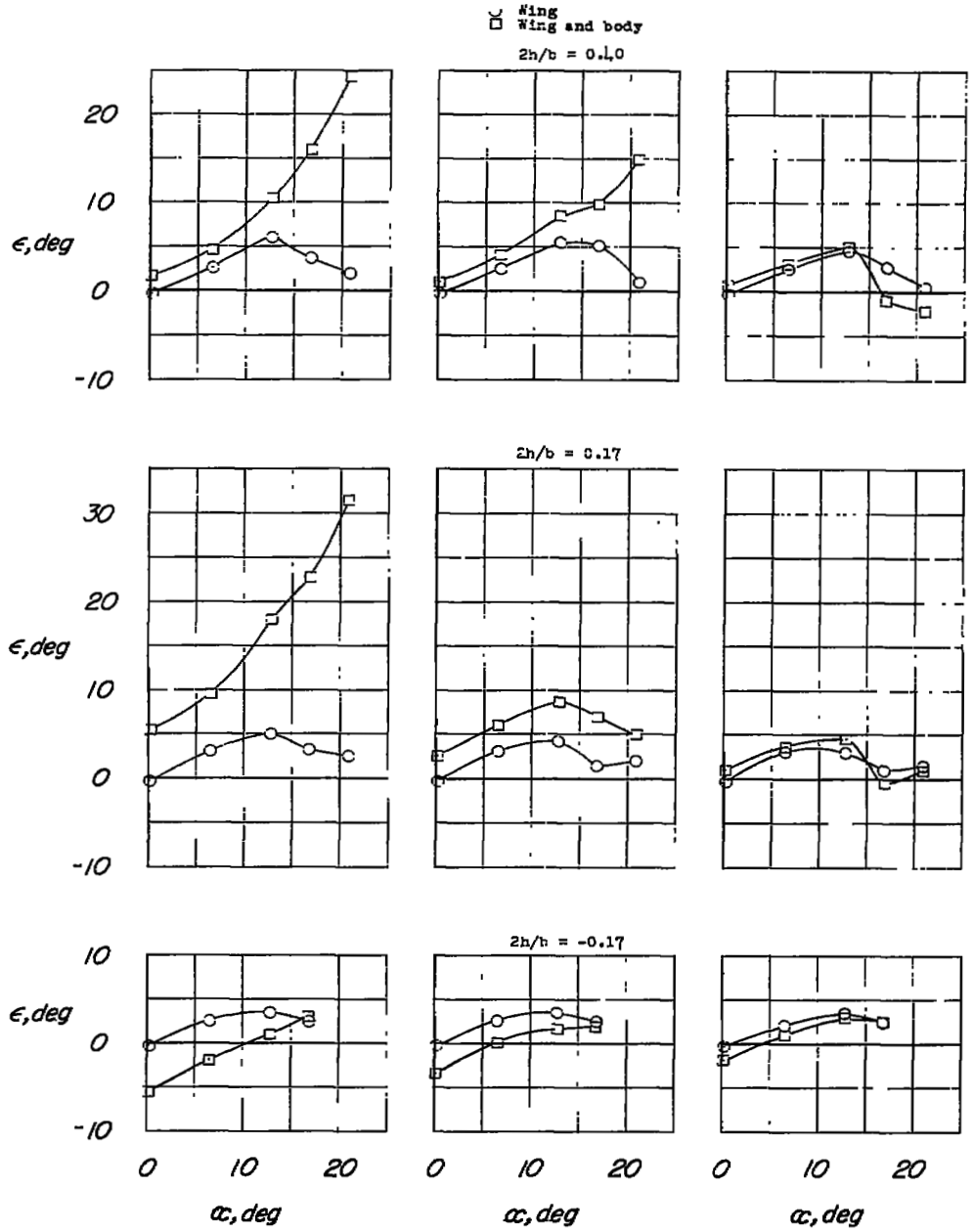

(a) 2y/b = 0. (b) 2y/b = 0.189. (c) 2y/b = 0.378.

Figure 39.- Variations with angle of attack of the downwash at several spanwise stations behind a 3.4-4.0-.63 wing with and without a body. The wing has 6-percent-thick hexagonal airfoil sections. $2x_0/b = 1.63$; α for $C_{L_{max}} = 14.6^\circ$; $R = 4.3 \times 10^6$; unpublished data from Langley 19-foot pressure tunnel.

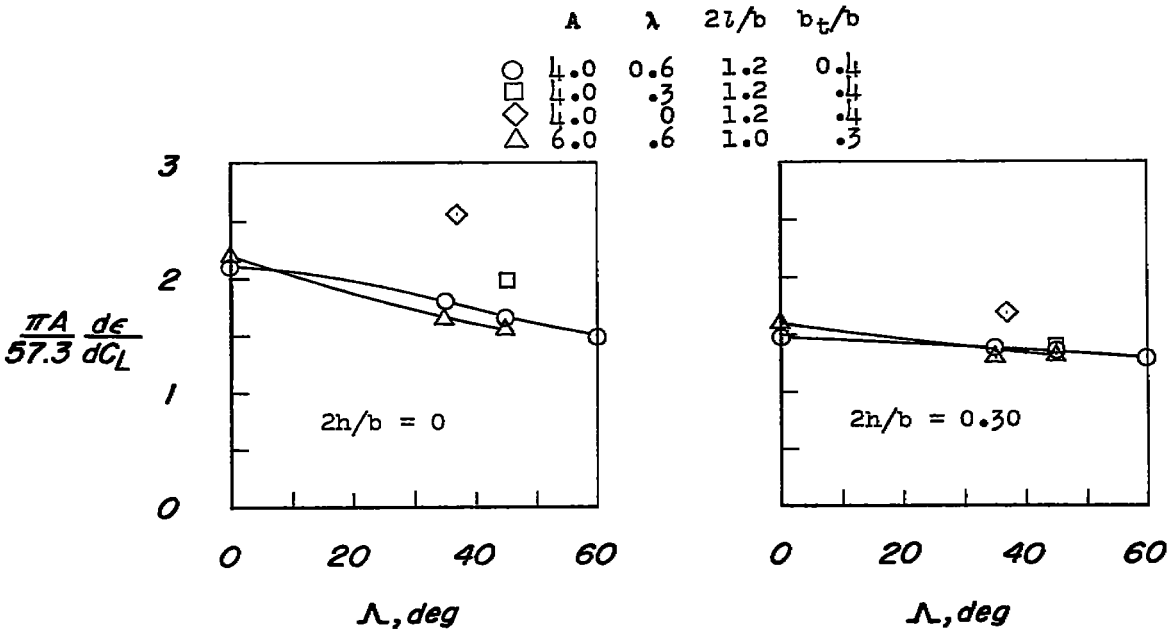

(a) Constant lift coefficient.

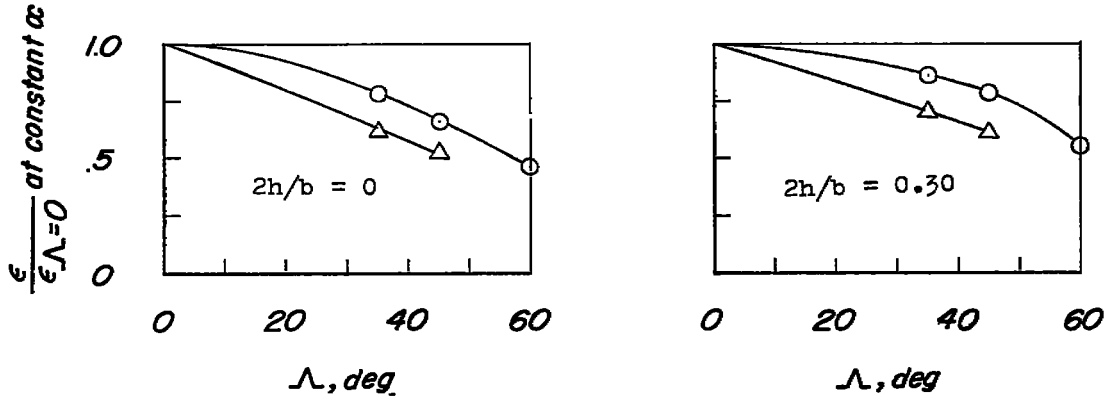

(b) Constant angle of attack.

Figure 40.- Effect of plan-form variables on the calculated wing downwash at low angles of attack. Reference 56.

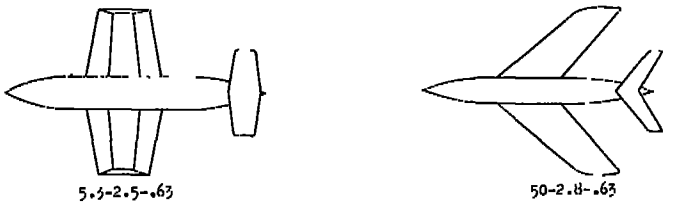

Wing	2l/b	b_t/b	Wing airfoil section	α for $C_{L_{max}}$	R	Reference
— — 5.3-2.5-.63	1.63	0.50	Hexagonal	14.6°	7.6×10^6	5
— — — 50-2.8-.63	1.21	.48	Circular arc (normal to line of maximum thickness)	27°	5.5×10^6	13

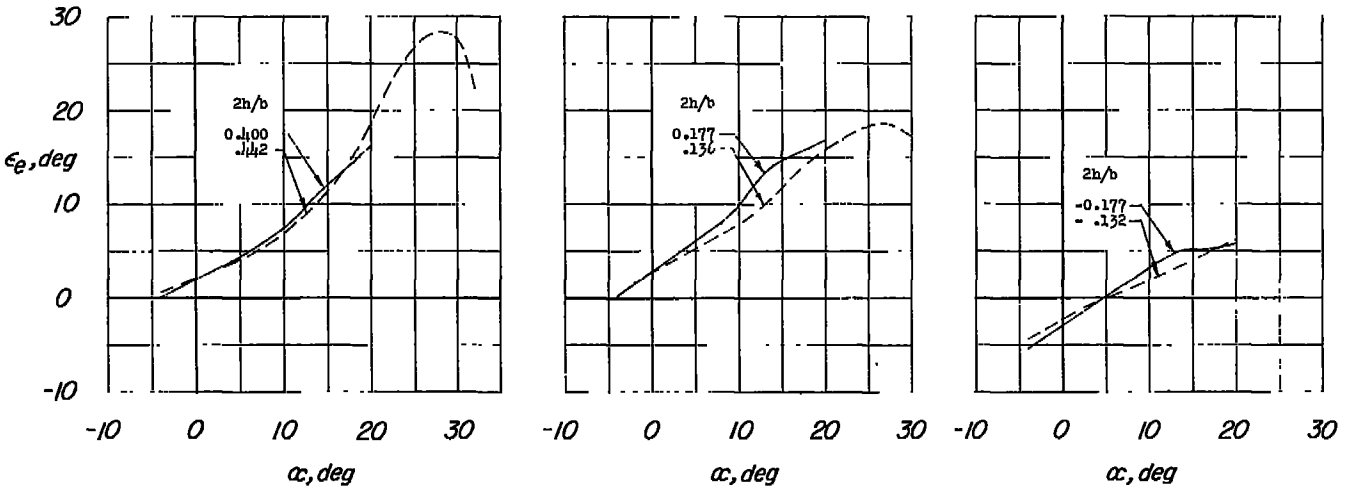

(a) ϵ_e against α.

Figure 41.- Effect of variation of wing sweep from 5° to 50° on ϵ_e, $\eta\left(\frac{q_t}{q}\right)_e$, and τ of wing-body combinations with the horizontal tails at several vertical positions.

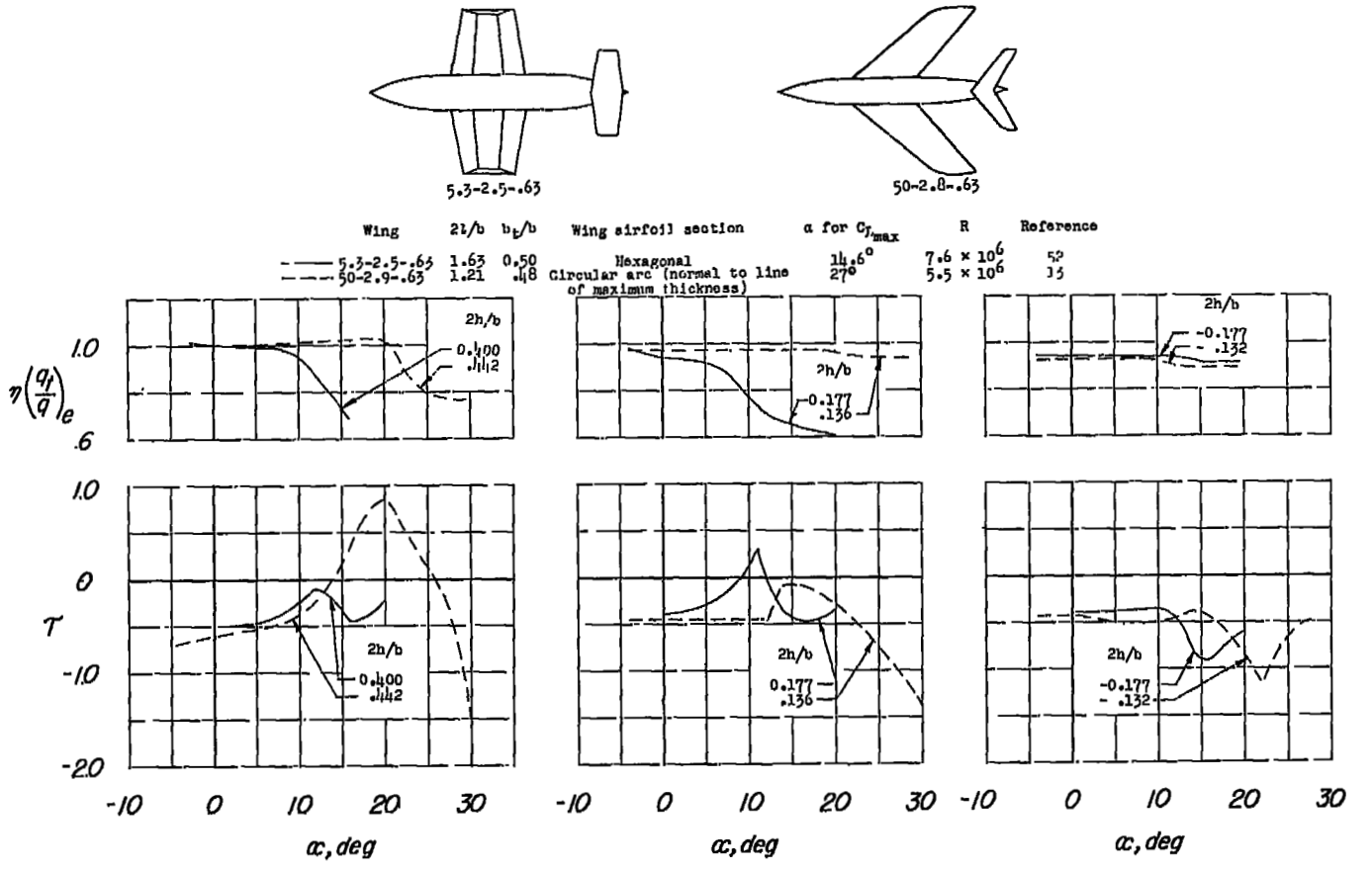

(b) $\eta\left(\frac{q_t}{q}\right)_e$ and τ against α.

Figure 41.- Concluded.

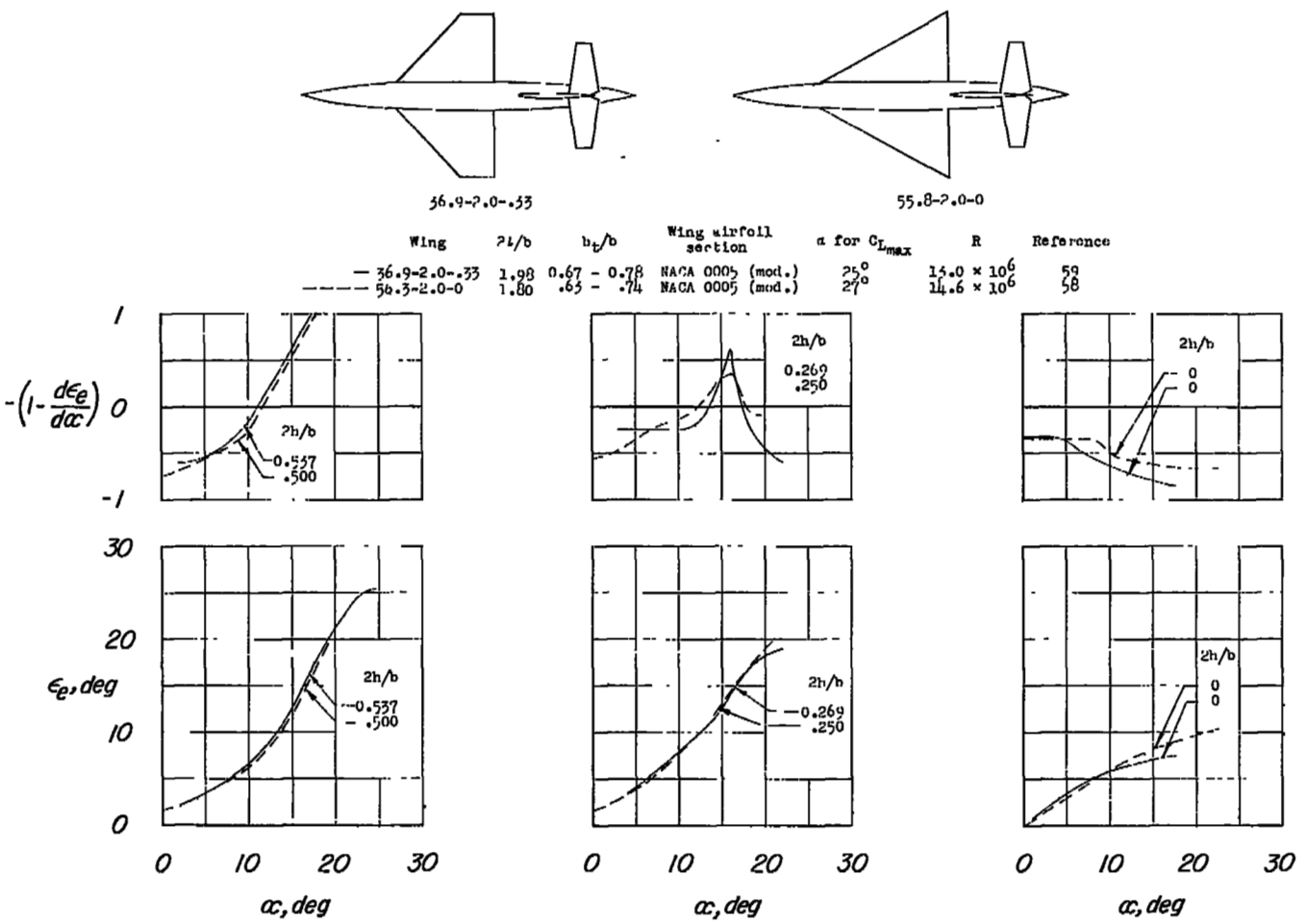

Figure 42.- Effect of the variation of wing sweep from 37° to 56° on ϵ_e and $-\left(1-\frac{d\epsilon_e}{d\alpha}\right)$ of wing-body combinations with the horizontal tails at several vertical positions.

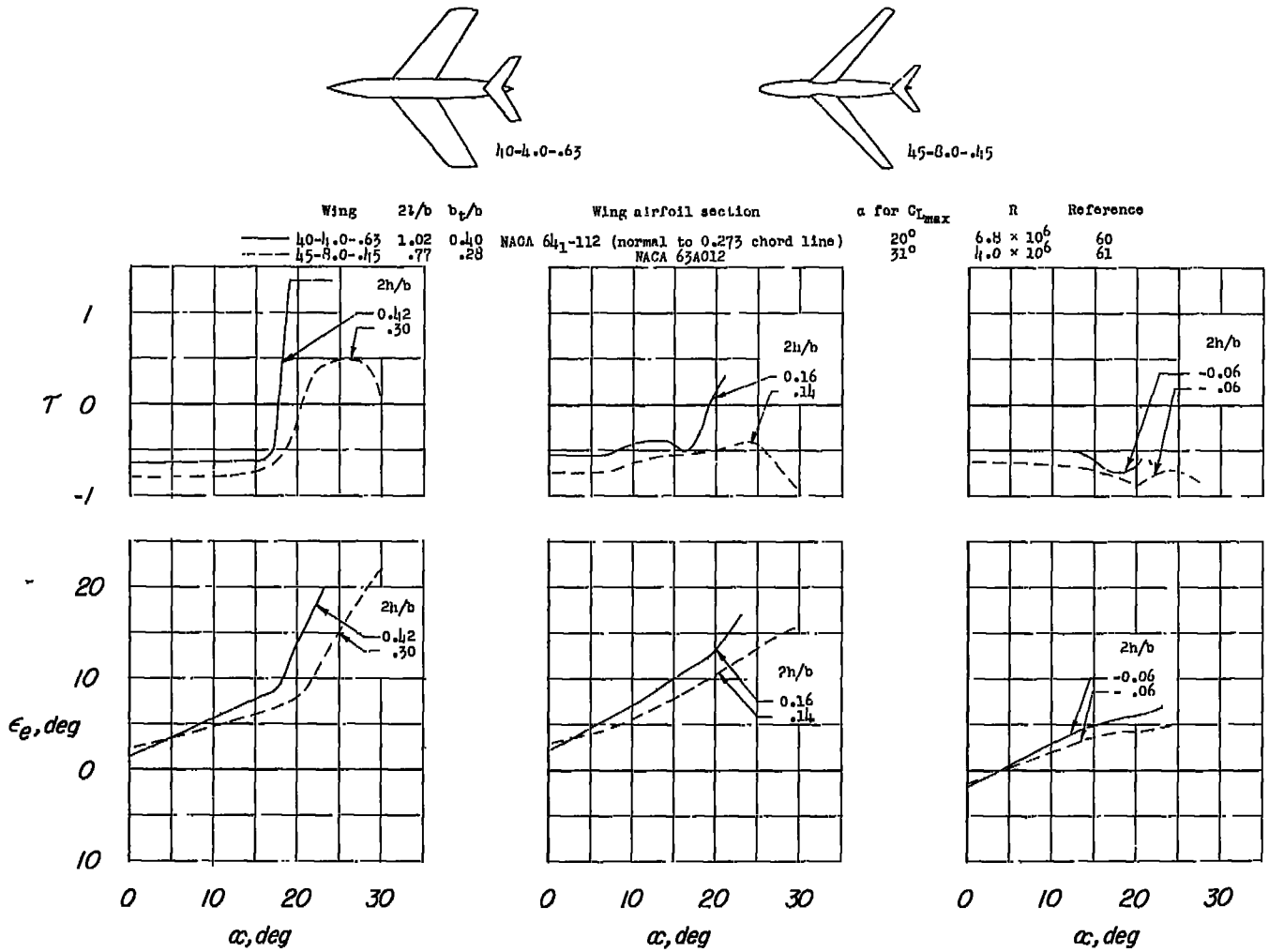

Figure 43.- Effect of wing aspect ratio on ϵ_e and τ of sweptback wing-body combinations with the horizontal tails at several vertical positions.

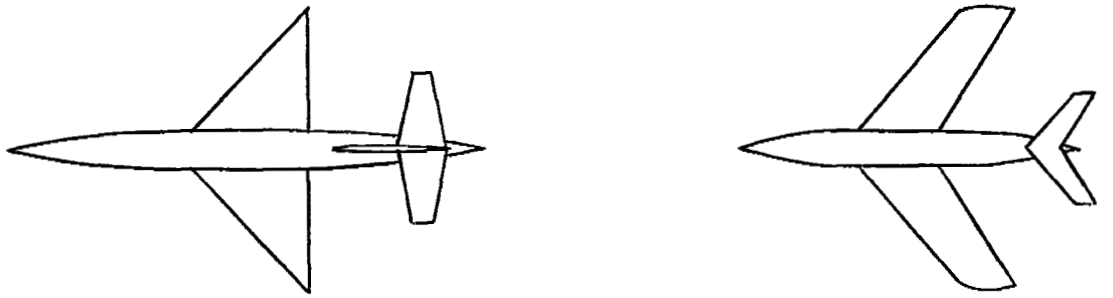

Wing	$2l/b$	b_t/b	Wing airfoil section	α for $C_{L_{max}}$	R	Ref.
——— 36.9-4.0-0	1.28	.45-.52	NACA 0005 (mod.)	22.7°	10.9×10^6	62
- - - - 40-3.9-.63	1.03	.40	Circular arc (normal to line of maximum thickness)	19°	6.9×10^6	63

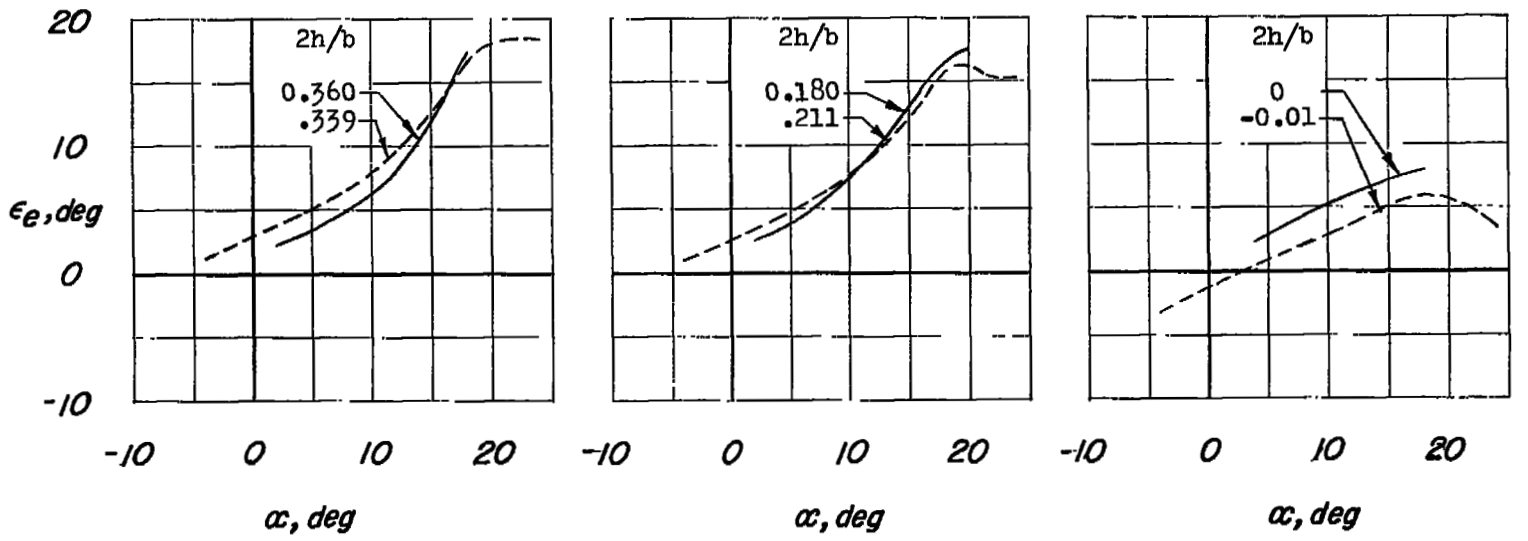

Figure 44.- Effect of wing taper ratio on ϵ_e of sweptback wing-body combinations with the horizontal tails at several vertical positions.

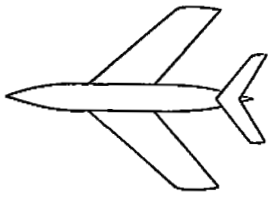

Wing	Wing airfoil section	2ℓ/b	b_t/b	R	Ref.
———	50-2.9-.65 NACA 641-112 (normal to 0.282 chord line)	1.23	0.48	6.0×10^6	27
– – – –	50-2.8-.65 Circular arc (normal to line of maximum thickness)	1.23	0.48	5.5×10^6	13

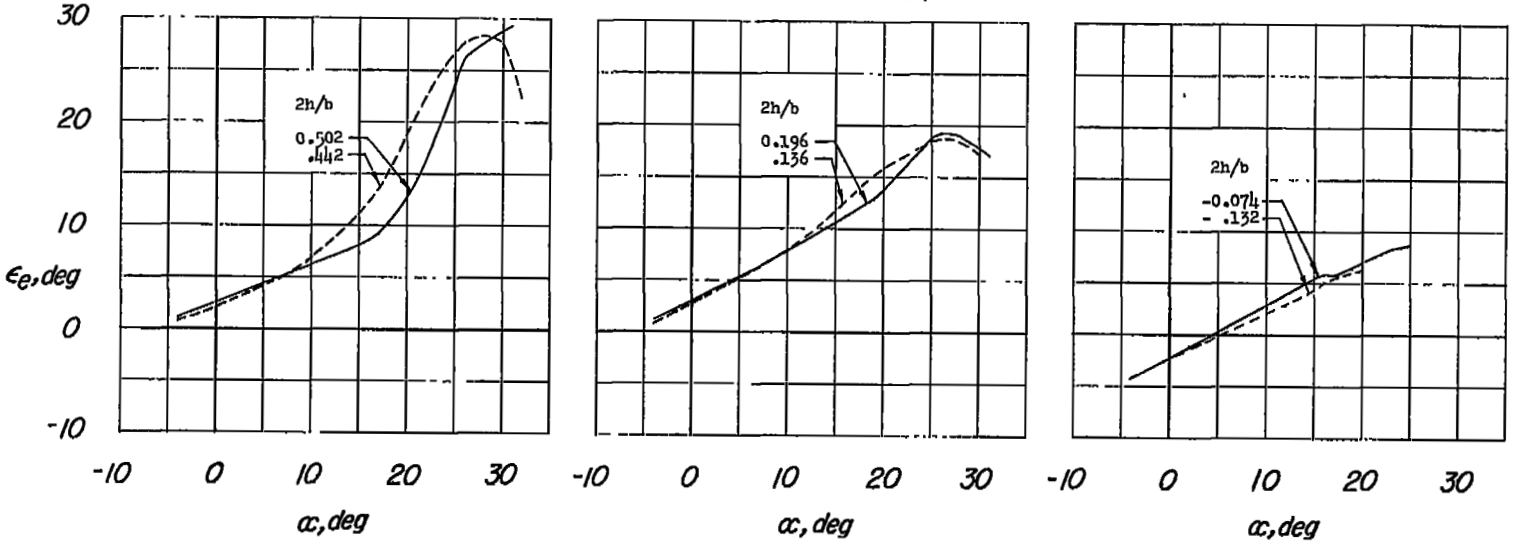

(a) ϵ_e against α.

Figure 45.- Comparison of the effect of wing airfoil section on ϵ_e and τ of sweptback-wing—body combinations with the horizontal tails at several vertical positions.

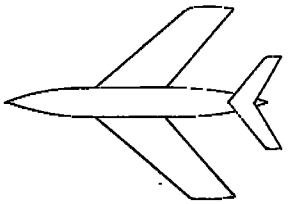

Wing	Wing airfoil section	2l/b	b_t/b	R	Ref.
——— 50-2.9-.63	NACA 64_1-112 (normal to 0.282 chord line)	1.23	0.48	6.0×10^6	27
– – – – 50-2.8-.63	Circular arc (normal to line of maximum thickness)	1.23	0.48	5.5×10^6	13

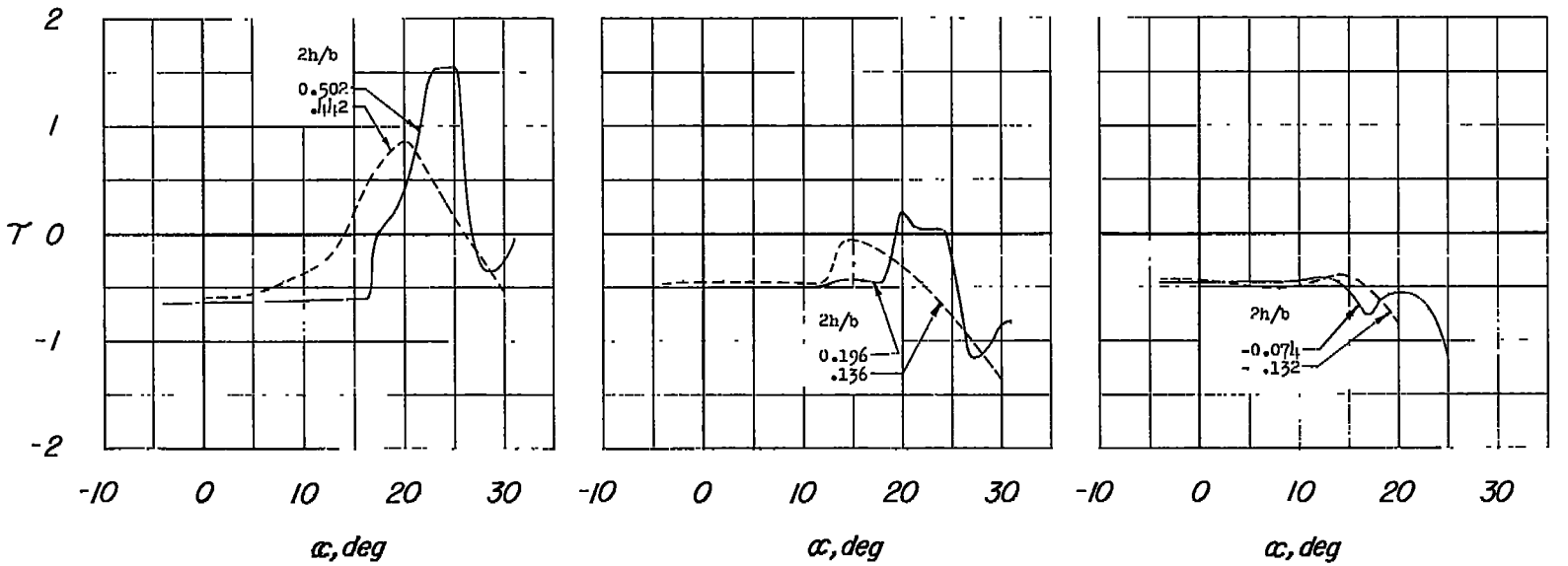

(b) τ against α.

Figure 45.- Concluded.

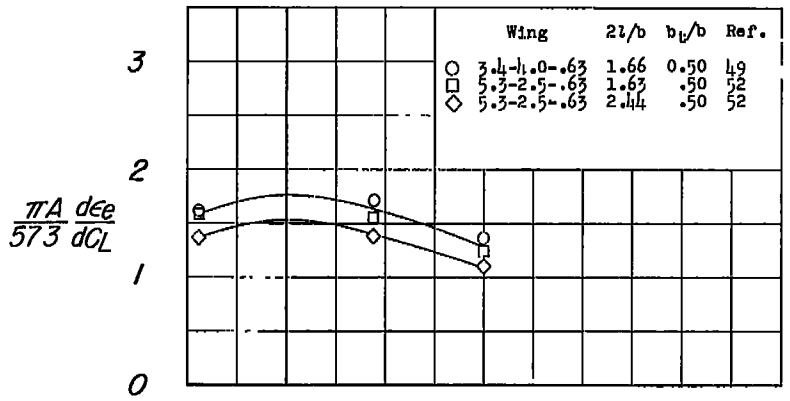

(a) $\lambda = 0.63$; $A = 2.5$ to 4; $\Lambda \approx 0^\circ$.

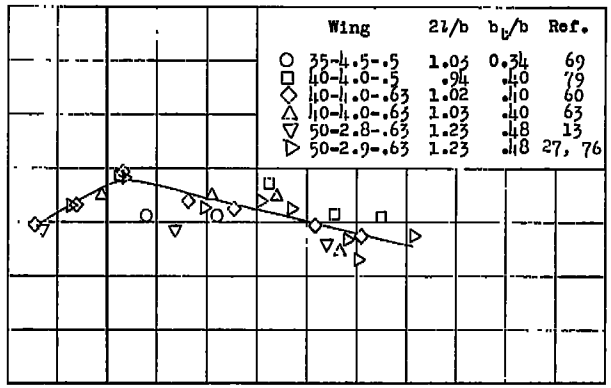

(b) $\lambda = 0.50$ to 0.63; $A = 2.9$ to 4.5; $\Lambda = 35^\circ$ to 50°.

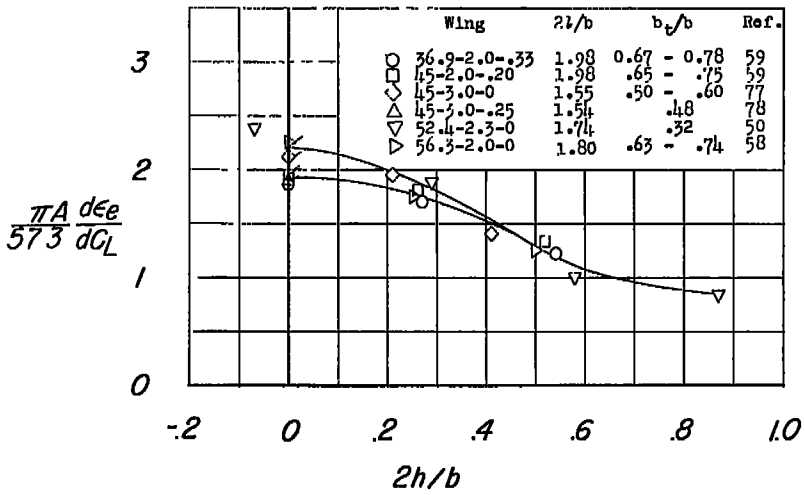

(c) $\lambda = 0$ to 0.33; $A = 2.0$ to 3.0; $\Lambda = 37^\circ$ to 56°.

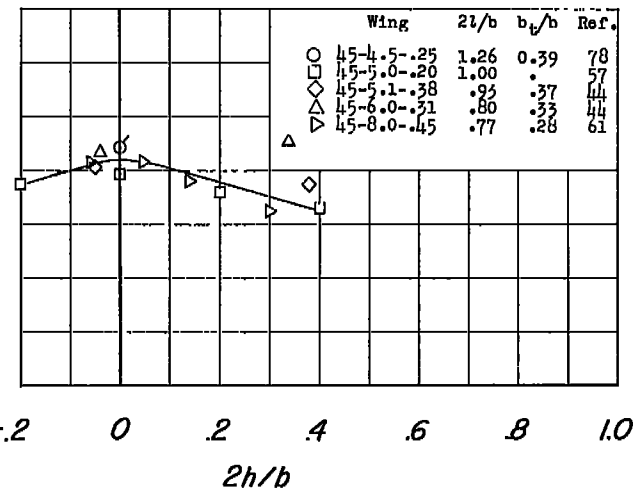

(d) $\lambda = 0.20$ to 0.45; $A = 4.5$ to 8.0; $\Lambda = 45^\circ$.

Figure 46.- Summary of downwash characteristics for wing-body combinations at low angles of attack. Flagged symbols indicate tail intersects body.

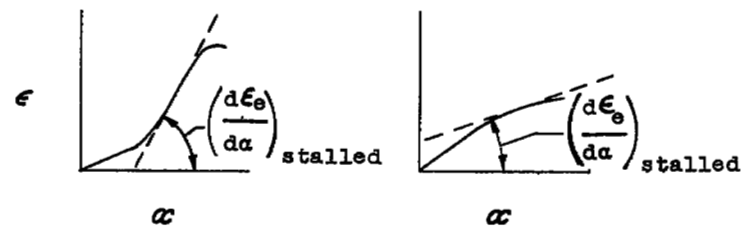

	Wing	2l/b	b_t/b	Ref.
○	36.9-2.0-.33	1.98	.67-.78	59
□	36.9-2.3-.25	1.37	.34	18
◇	45-2.0-.20	1.98	.65-.75	59
△	52.8-2.3-0	1.74	.32	50
▽	52.8-2.3-0	2.32	.32	50
▷	56.3-2.0-0	1.80	.63-.74	58

	Wing	2l/b	b_t/b	Ref.
○	45-3.0-0	1.56	.50-.60	77
□	45-3.0-0	1.07	.54	70
◇	45-3.0-0	1.34	.47	70
△	50-2.9-.63	1.23	.48	27, 76
▽	50-2.8-.63	1.23	.48	13

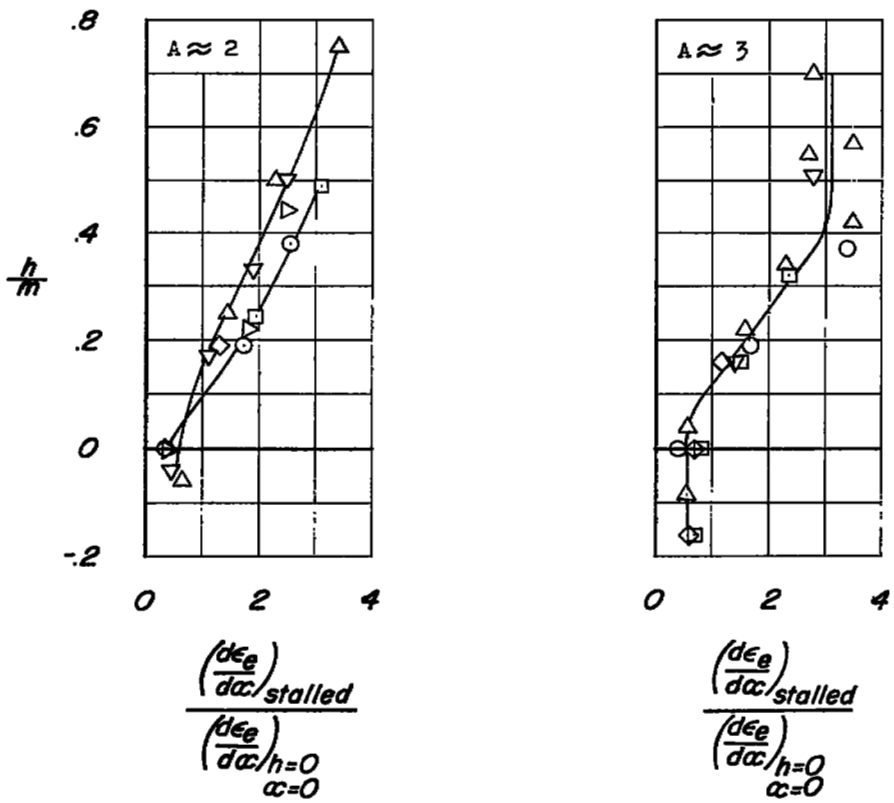

Figure 47.- Summary of $d\epsilon_e/d\alpha$ in the stalled range of lift coefficients for various sweptback wing-fuselage combinations.

Wing	$2l/b$	b_t/b	Ref.
○ 35-4.5-.5	1.03	0.34	69
□ 36.9-4.0-0	1.28	.32-.39	62
◇ 36.9-4.0-0	1.28	.45-.52	62
△ 40-3.9-.63	1.03	.40	63
▽ 40-4.0-.63	1.02	.40	60

Wing	$2l/b$	b_t/b	Ref.
○ 45-5.1-.38	0.93	0.37	44
□ 45-8.0-.45	.77	.28	61

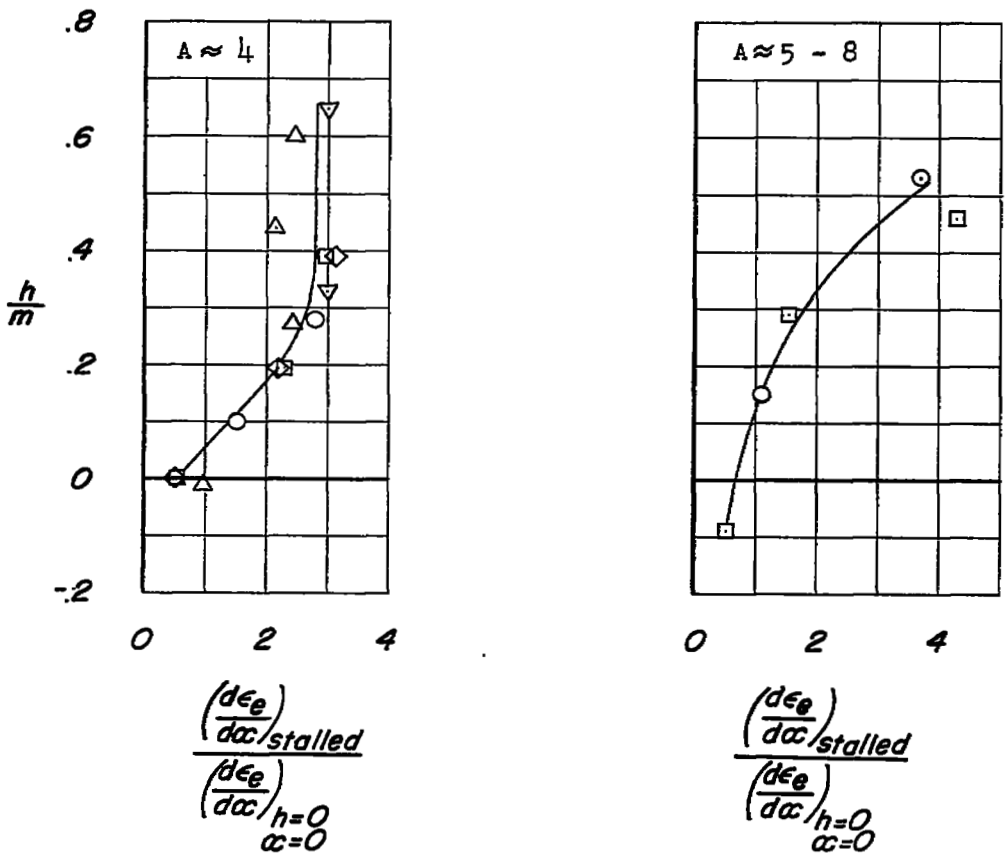

Figure 47.- Concluded.

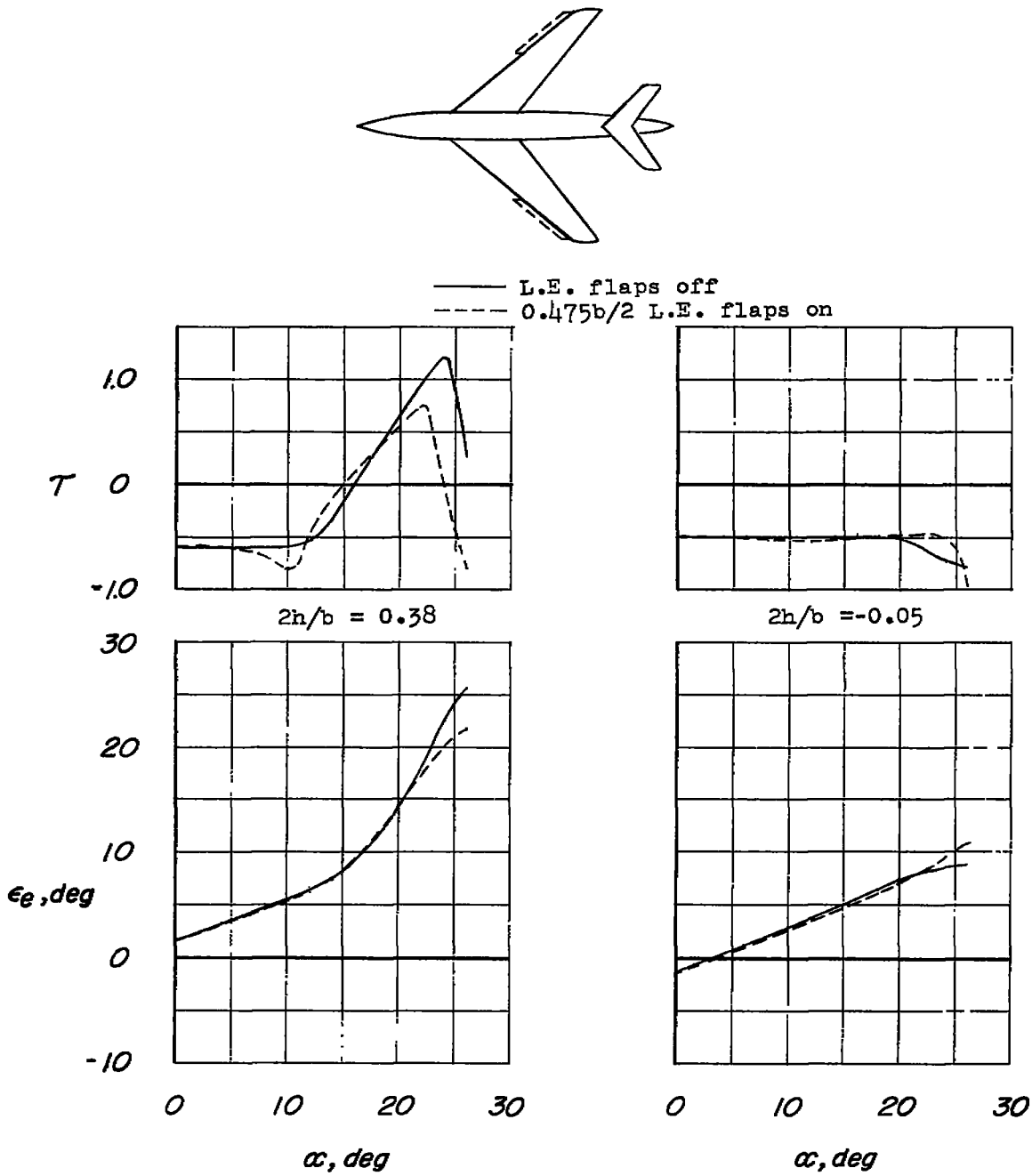

Figure 48.- Effect of wing leading-edge flaps on ϵ_e and τ of a 45-5.1-.38 wing-body combination with the horizontal tail at two vertical positions. The wing has NACA 64-210 airfoil sections normal to the 0.286 chord line; $2l/b = 0.93$; $b_t/b = 0.365$; $R = 6.0 \times 10^6$; reference 44.

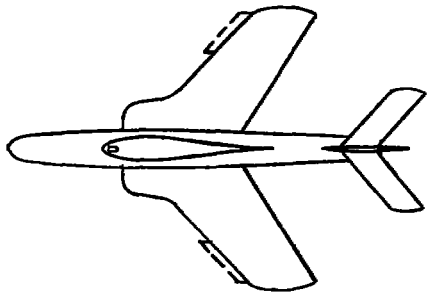

——— Chord-extensions off
– – – – 0.30b/2 Chord-extensions on

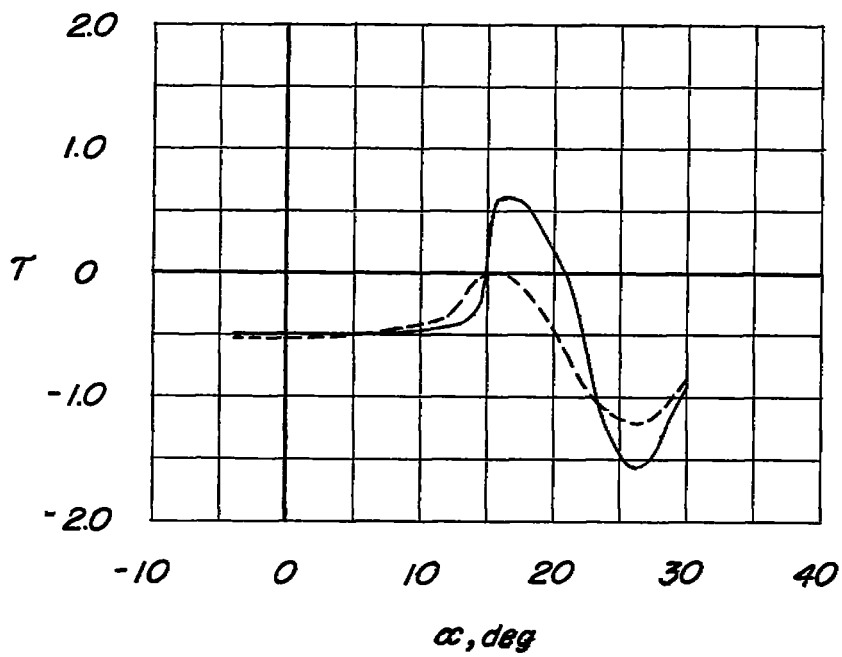

Figure 49.- Effect of wing leading-edge chord extensions on the stability parameter τ of a 40-3.5-.58 wing-body combination. The wing had NACA 64A010 airfoil sections normal to 0.25 chord line; $2h/b = 0.28$; $2l/b = 1.20$; $b_t/b = 0.424$; $R = 9.0 \times 10^6$; unpublished data from Langley 19-foot pressure tunnel.

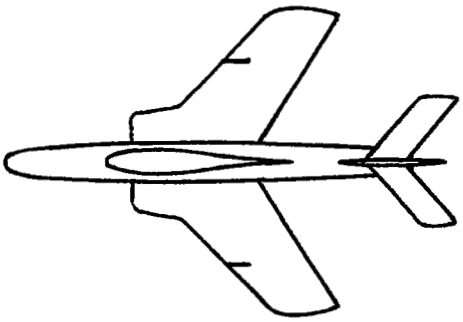

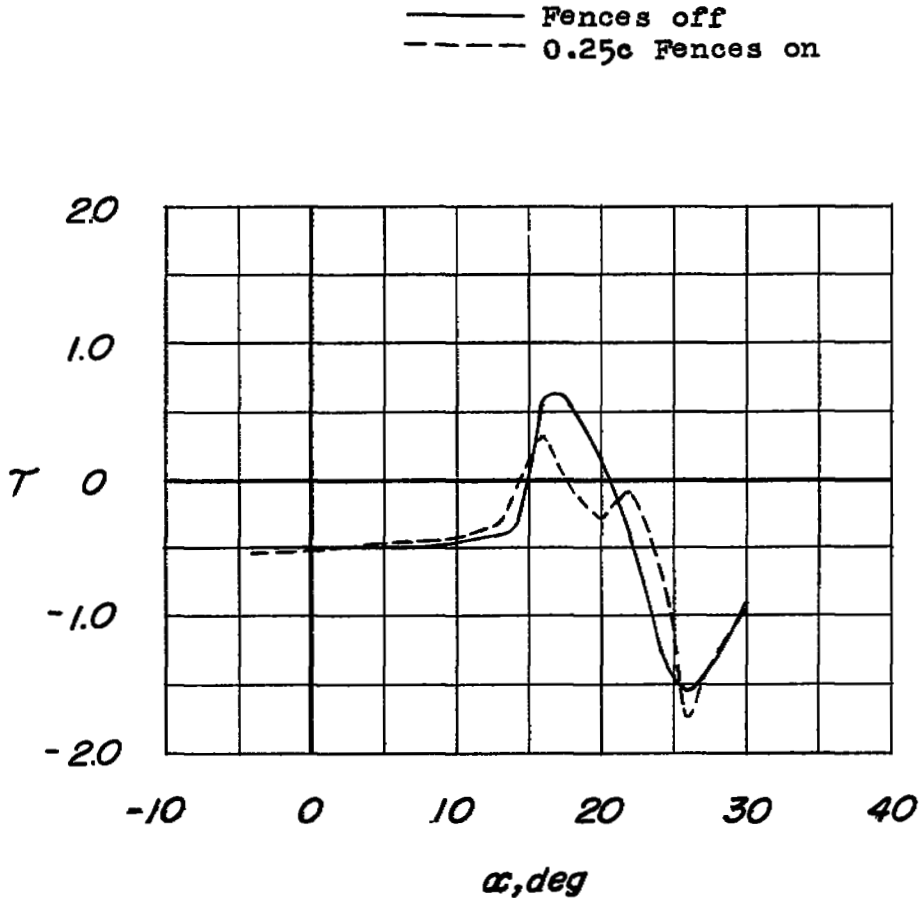

Figure 50.- Effect of wing fences on the stability parameter τ of a 40-3.5-.58 wing-body combination. The wing had NACA 64A010 airfoil sections normal to 0.25 chord line; $2h/b = 0.28$; $2l/b = 1.20$; $b_t/b = 0.424$; $R = 9.0 \times 10^6$; unpublished data from Langley 19-foot pressure tunnel.

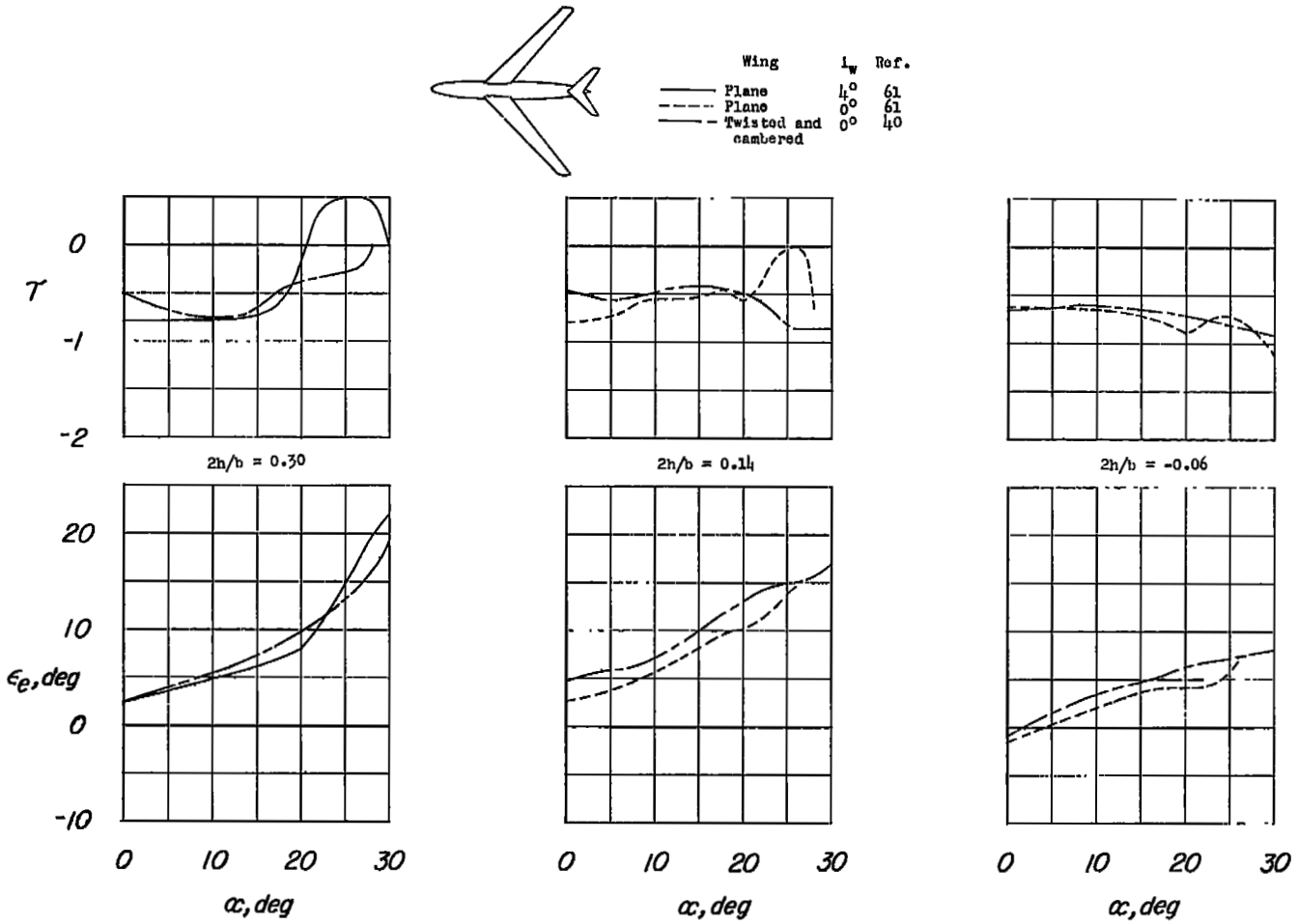

Figure 51.- Effects of wing twist and camber on ϵ_e and τ of a 45-8.0-.45 wing-body combination with the horizontal tail at several vertical positions. The wings had NACA 63AX12 airfoil sections. $2l/b = 0.77$; $b_t/b = 0.28$; $R = 4.0 \times 10^6$.

	Wing	Flap	b_f/b	b_t/b_f	$2l/b$	Reference
○	3.4-4.0-.63	Plain	0.55	0.91	1.66	49
□	5.3-2.5-.63	Plain	.55	.91	1.63	52
◇	5.3-2.5-.63	Plain	.95	.53	1.63	52
△	40-3.0-.25	Split	.50	.96	1.54	78
▽	40-4.5-.25	Split	.50	.78	1.26	78
◁	40-4.0-.63	Split	.50	.80	1.02	60
▷	45-5.1-.38	Split	.40	.91	.93	44
◸	45-8.0-.45	Split	.35	.80	.77	61
◺	50-2.8-.63	Split	.40	1.20	1.23	13
◿	50-2.9-.63	Split	.40	1.20	1.23	27
◹	36.9-4.0-0	Single slotted	.70	.78	1.28	75
◻	36.9-2.0-.33	Single slotted	1.00	.78	1.98	59
◼	45-2.0-.20	Single slotted	.96	.78	1.98	59
◪	45-3.2-.47	Single slotted	.84	.60	1.19	Unpublished
◫	45-5.1-.38	Double slotted	.40	.91	.93	44
◩	45-8.0-.45	Ext. split	.50	.56	.77	61
◧	50-2.8-.63	Ext. split	.50	.96	1.23	13
▣	50-2.9-.63	Ext. split	.40	1.20	1.23	27

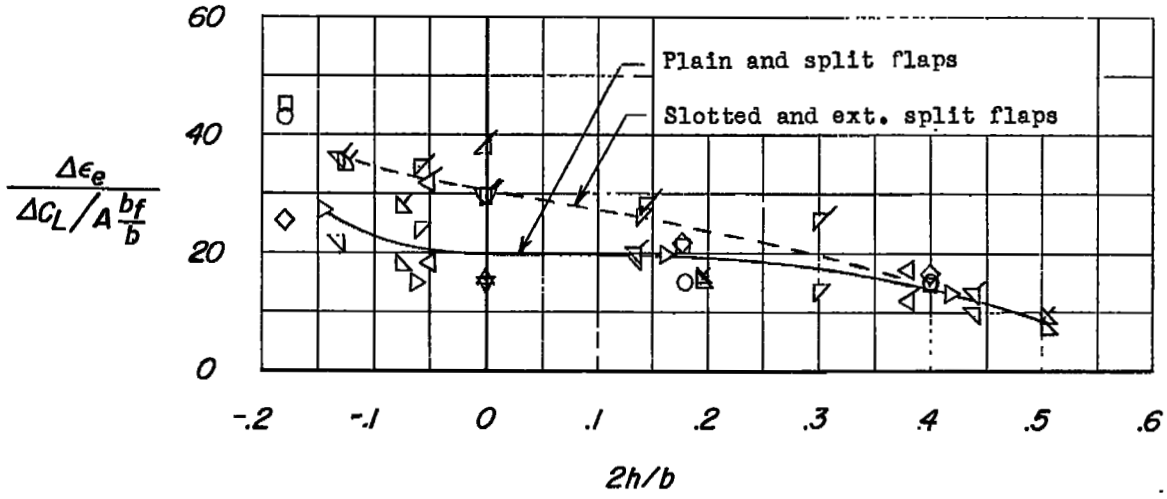

Figure 52.- Summary of data on downwash due to trailing-edge flaps on wing-body combinations. $\alpha = 0^\circ$.

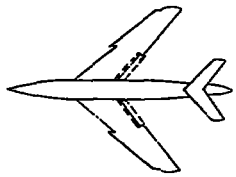

Airfoil: NACA 64-210
(normal to 0.286 chord line)

T.E. flaps	α for $C_{L_{max}}$
——— off	25°
- - - - 0.40b/2 split	23°
——— 0.40b/2 double slotted	19°

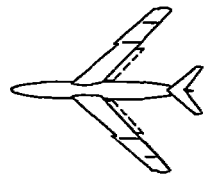

Airfoil: NACA 63_1A012

T.E. flaps	α for $C_{L_{max}}$
——— off	27°
- - - - 0.50b/2 ext. split	28°

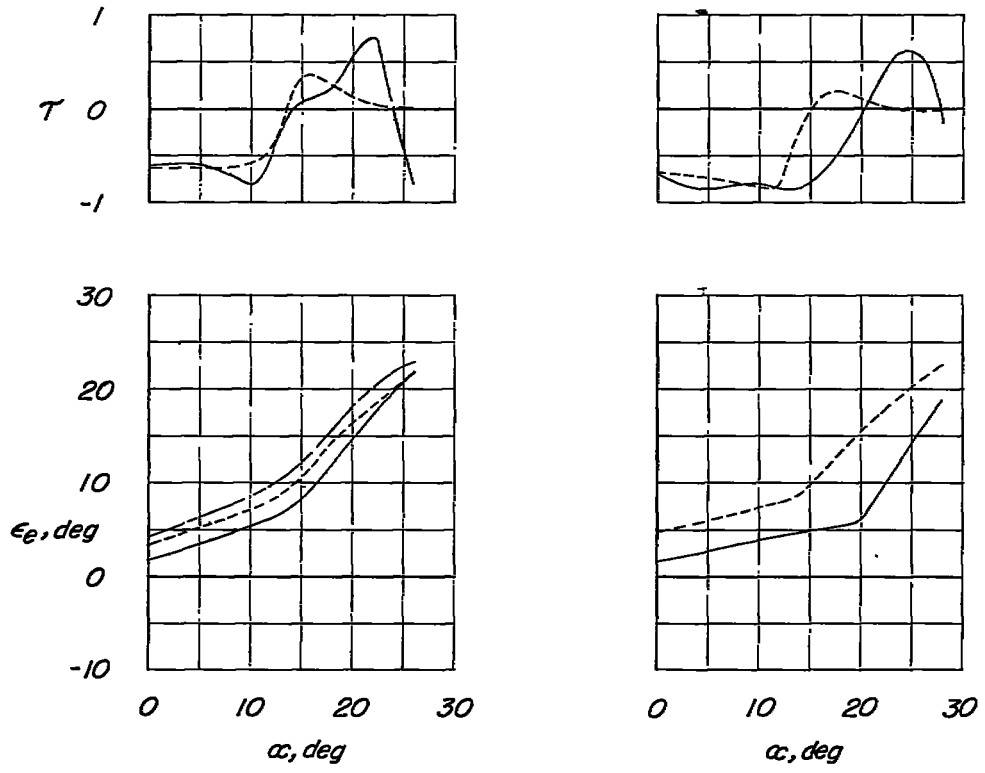

(a) 45-5.1-.38 wing with L.E. flaps; 2h/b = 0.38; 2l/b = 0.93; R = 6.0×10^6; reference 44.

(b) 45-8.0-.45 wing with L.E. flaps and fences; 2h/b = 0.30; 2l/b = 0.77; R = 4.0×10^6; reference 61.

Figure 53.- Effect of trailing-edge flaps on ϵ_e and τ for several 45° sweptback-wing—body combinations with the horizontal tail mounted in a high position.

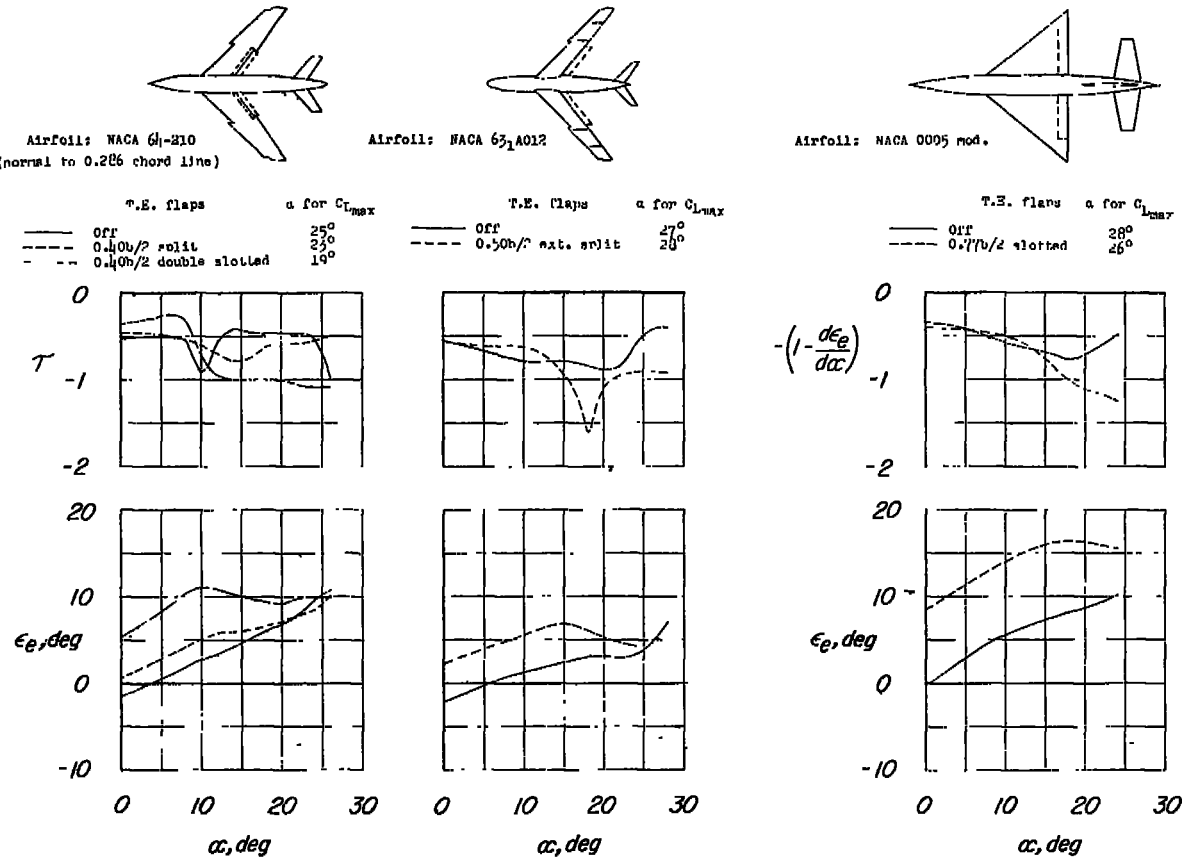

(a) 45-5.1-.38 wing with L.E. flaps; $2h/b = -0.05$; $2l/b = 0.93$; $R = 6.0 \times 10^6$; reference 44.

(b) 45-8.0-.45 wing with L.E. flaps and fences; $2h/b = -0.06$; $2l/b = 0.77$; $R = 4.0 \times 10^6$; reference 61.

(c) 45-3.0-0 wing; $2h/b = 0$; $2l/b = 1.56$; $R = 12.8 \times 10^6$; reference 77.

Figure 54.- Effect of trailing-edge flaps on ϵ_e and τ for several 45° sweptback-wing—body combinations with the horizontal tail mounted in a low position.

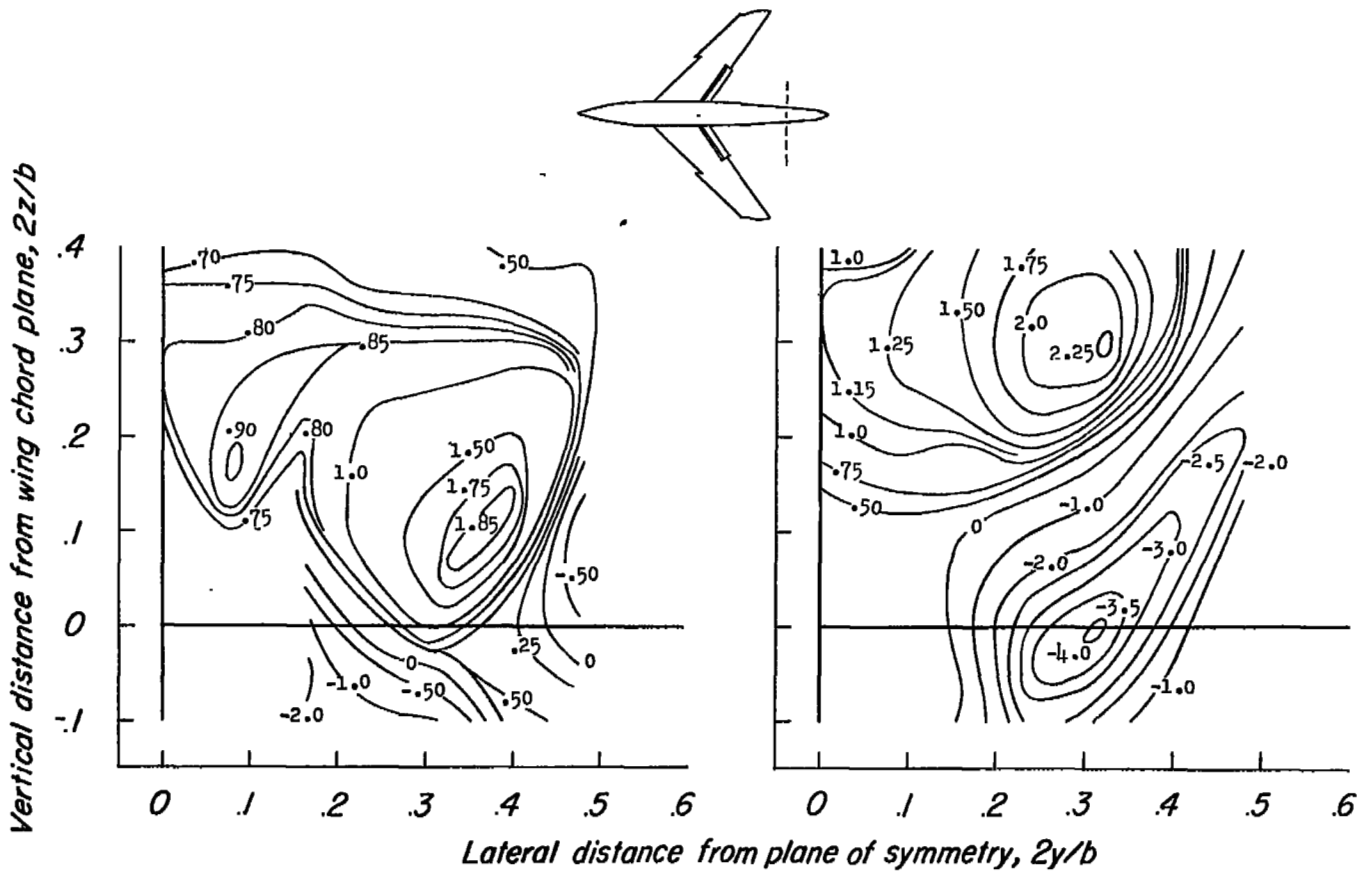

(a) $\alpha = 12^{\circ}$.

(b) $\alpha = 17^{\circ}$.

Figure 55.- Contours $d\epsilon/d\alpha$ behind a 45-5.1-.38 wing-body combination with 0.40b/2 double slotted flaps. The wing had NACA 64-210 airfoil sections normal to the 0.286 wing chord line. 0.475b/2 leading-edge flaps; $2x_0/b = 0.88$; $R = 6.0 \times 10^6$; separation on wing occurs initially at $\alpha = 11^{\circ}$; α for $C_{L_{max}} = 19^{\circ}$; reference 44.

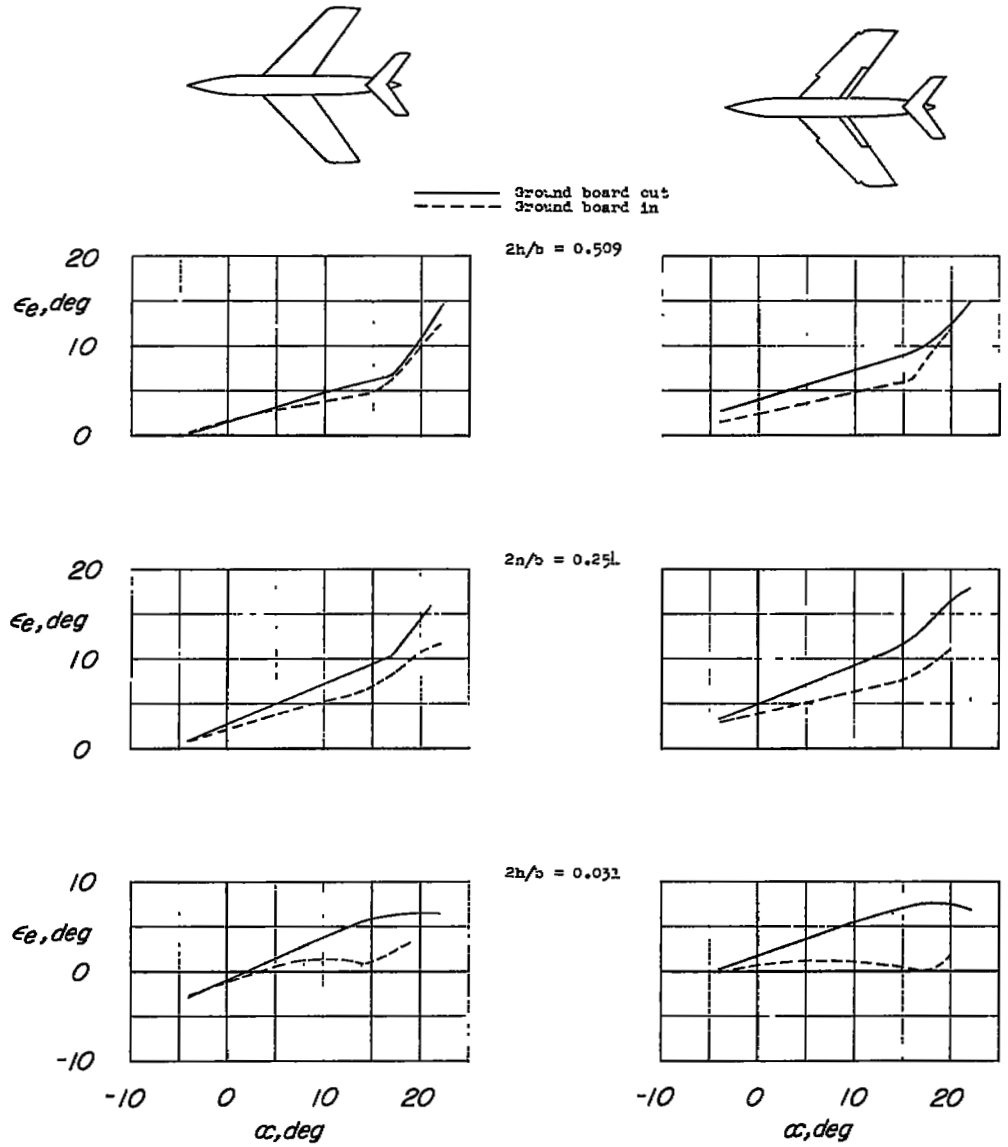

(a) Flaps off.

(b) 0.575b/2 leading-edge flaps on; 0.500b/2 split trailing-edge flaps on.

Figure 56.- Effect of ground on the downwash at several tail heights behind a 40-4.0-.63 wing-body combination with and without flaps. The wing was in a low position and had NACA 64_1-112 airfoil sections normal to the 0.273 chord line. The ground distance was 0.92c' measured from quarter-chord point of wing mean aerodynamic chord to ground board. $2l/b = 1.018$; $R = 6.8 \times 10^6$; reference 60.

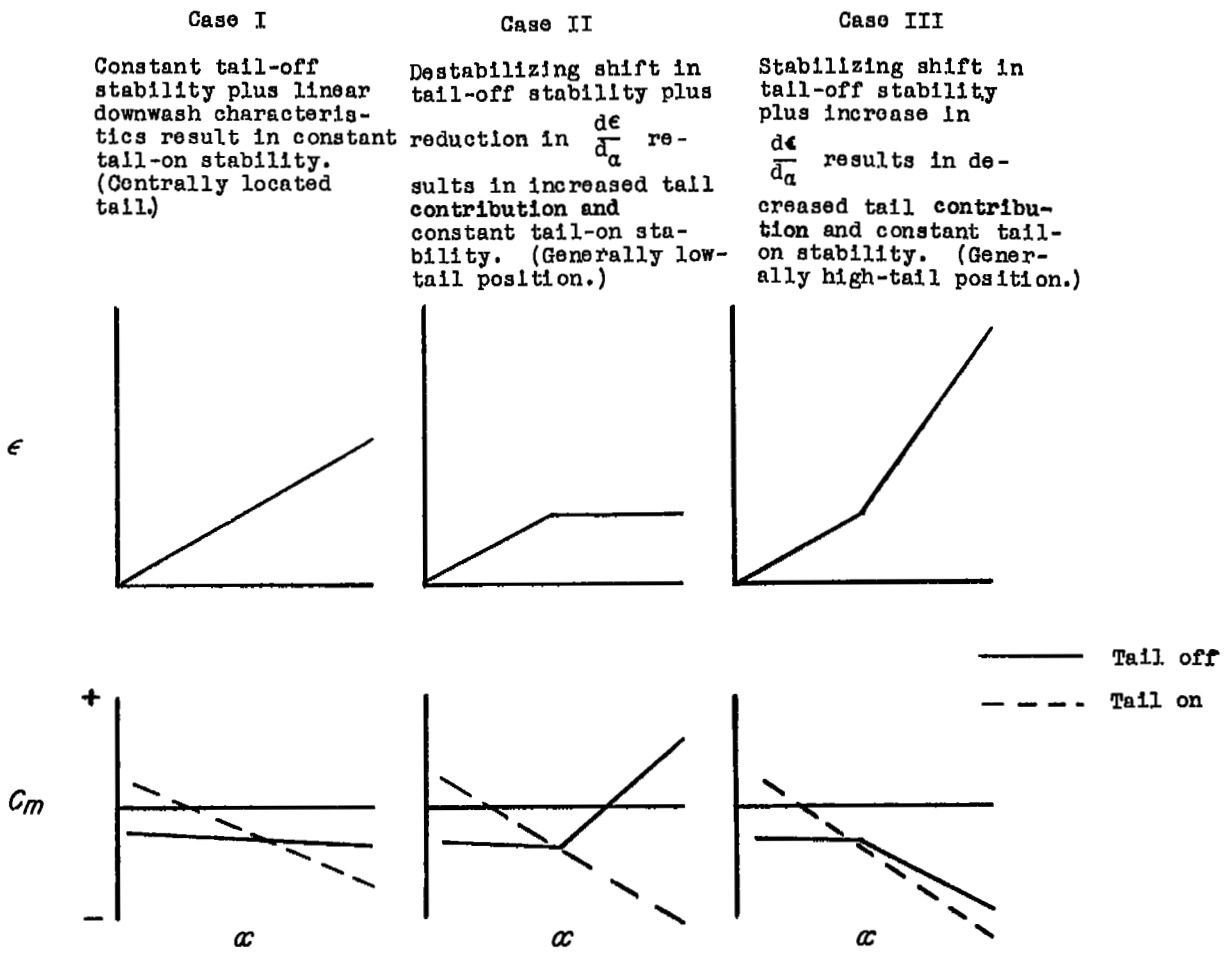

Figure 57.- An idealized illustration of the improvement made in the pitching-moment characteristics of typical wing-body combinations by the use of a horizontal tail operating in the downwash field behind a sweptback wing.

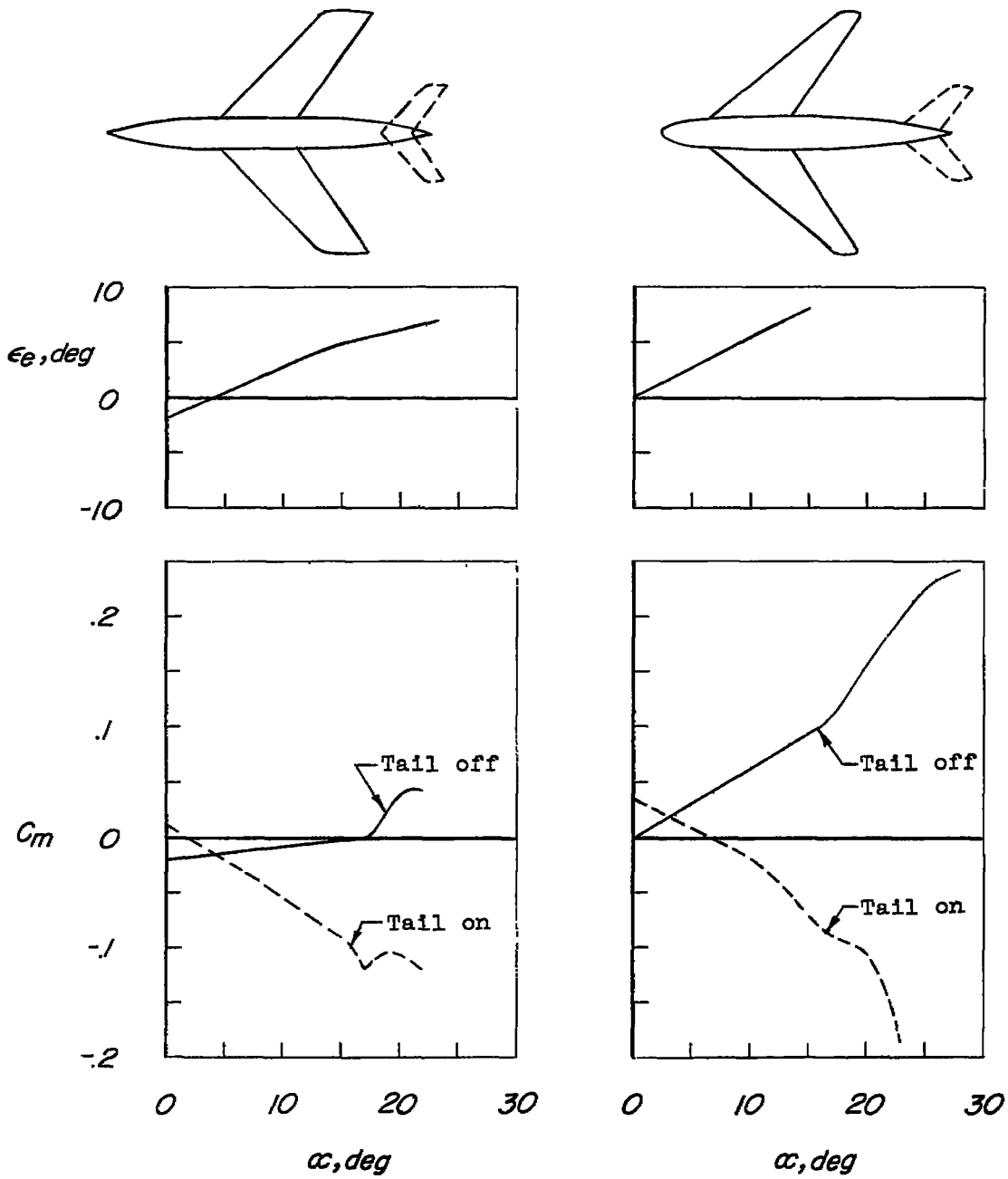

(a) 40-4-.63; V = 0.32; 2h/b = -0.06; 2l/b = 1.0; center of gravity at 0.25c'; reference 60.

(b) 45-4.5-.25; V = 0.584; 2h/b = 0; 2l/b = 1.17; center of gravity at 0.45$\bar{c}$; reference 78.

Figure 58.- Effect of a horizontal tail on the pitching-moment characteristics of configurations having unstable sweptback wings.

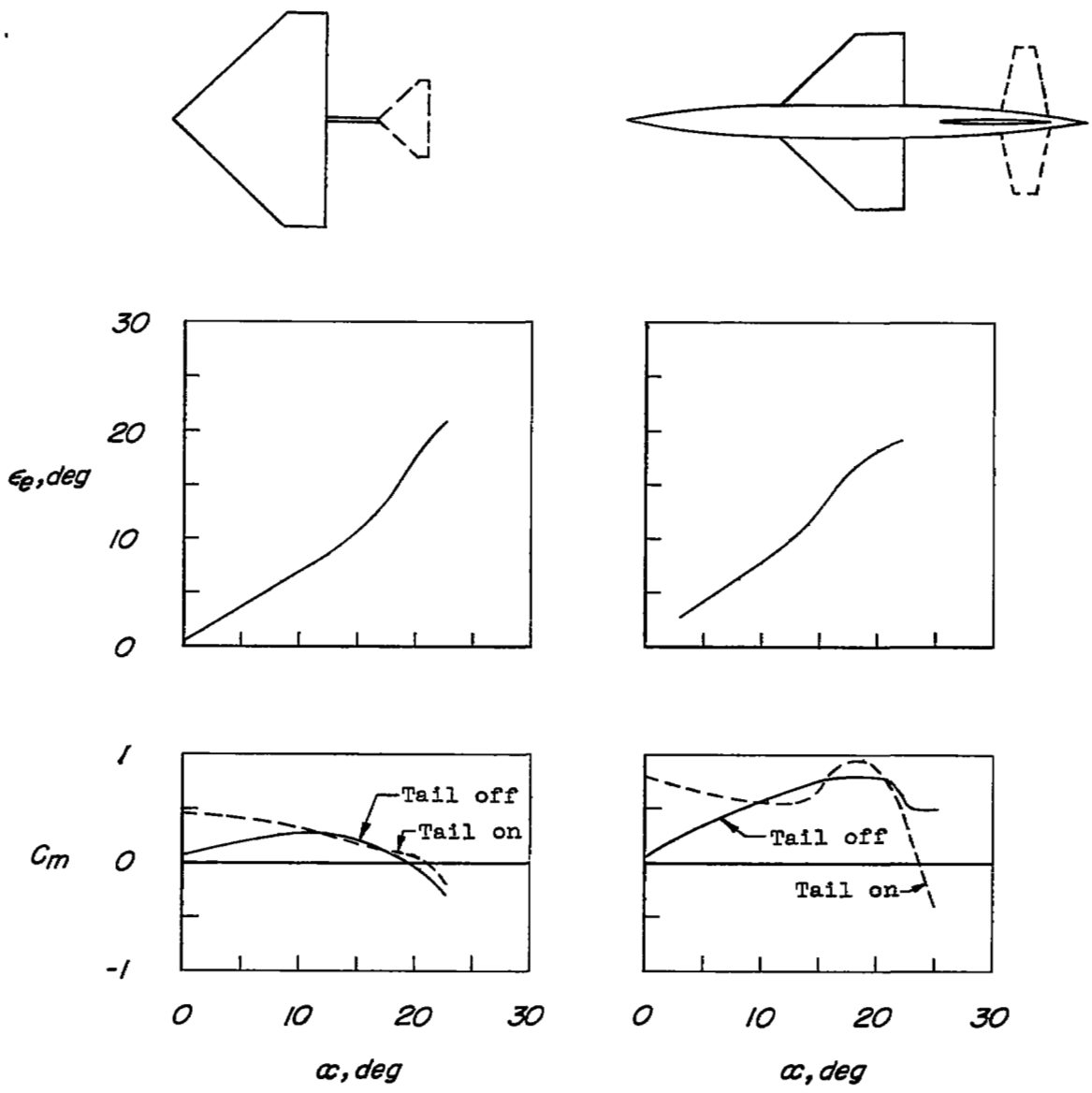

(a) 36.8-2.3-.25; V = 0.193; 2h/b = 0.23; 2l/b = 1.36; center of gravity at 0.525 wing-root chord; reference 18.

(b) 36.9-2.0-.33; V = 0.383; 2h/b = 0.27; 2l/b = 1.85; center of gravity at 0.37c'; reference 59.

Figure 59.- Effect of a horizontal tail on the pitching-moment characteristics of configurations having stable sweptback wings.

NACA - Langley Field, Va.